The Solar Corona Through Numerical Eyes

by
Ofer Cohen

A dissertation submitted in partial fulfillment
of the requirements for the degree of
Doctor of Philosophy
(Space and Planetary Physics)
in The University of Michigan
2008

Doctoral Committee:

Professor Tamas I. Gombosi, Chair
Professor Lennard A. Fisk
Professor Kenneth G. Powell
Research Scientist Igor V. Sokolov
Research Scientist Gabor Toth
Associate Research Scientist Ward B. Manchester IV
Assistant Astronomer Ilia I. Roussev, University of Hawaii

To my parents, for making me,
to Dganit, for making me who I am,
and to my son, for what he will make me.

ACKNOWLEDGEMENTS

First, and foremost, I would like to thank my wife, Dganit, for coming up with the idea to apply for graduate studies in the US and for making so much sacrifieses. I would like to thank my mentors: Peter Israelevich, for introducing me to the world of space and plasma physics, Tamas Gombosi, for giving me the opportunity to be part of one of the bset groups in the world for modeling of Space Physics, Igor Sokolov, for teaching me how to understand physics so much better, Ilia Roussev, for making sure I know what I am doing, Gabor Toth, for teaching me how to write codes, Len Fisk, for his scientific inspirations, and Chip Manchester for his constant ideas and suggestions. I would also like to thank Ken Powell for being part of my thesis committee.

I would like to thank all faculty, research, and administrative staff at AOSS for all their help through the time I spent at Michigan:

- **CSEM members:** Rich Frazin, Aaron Ridley, K.C. Hansen, Darren DeZeeuw, Janet Kozyra, Mike Liemohn, Andy Nagy, and Bart Vanderholst.
- **AOSS members:** Natalia Andronova, John Barker, Mike Combi, Paul Drake, Sue Lepri, Chris Parkinson, and Thomas Zurbuchen.
- **AOSS administrative staff:** Jan Beltran, Debbie Eddy, Sue Griffin, Kristi Hansen, Marti Moon, Mary Nehls-Frumkin, Kathy Norris, Sandra Petlinsky, Margaret Reid, Aimee Reische, Faye Ogasawara, and Bryan White.

I would like to thank all my fellow students and post-docs: Alex Glocer, Dan Welling, Noe Lugaz, David Applbaum, Rona Oran, Jared Bell, Amanda Brecht, Fang Fang, Yanshi Huang, Anna DeJong, Jason Gilbert, Raluca Ilie, Tamara McDunn, Pran Mukherjee, Dalal Najib, Dave Pawlowski, Arnaud Valeille, Judy Yu, Liang Zhao, Gregory Bee, Yiqun Yu, Lena Adams, Martin Rubin, and Valeriy Tenishev.

I would like to thank my guitar for not being mad at me even thought I left her to something more sexy (space physics...). I also like to thank the Michigan football team and the Hapoel Tel-Aviv soccer team for providing very happy and very sad moments in my life.

Finally, I would like to thank my parents for exposing me to the world of astronomy and for raising me to be who I am. I hope this work serves as a certificate for a good job.

TABLE OF CONTENTS

DEDICATION . . . . . **ii**

ACKNOWLEDGEMENTS . . . . . **iii**

LIST OF FIGURES . . . . . **vii**

LIST OF TABLES . . . . . **xii**

LIST OF APPENDICES . . . . . **xiii**

CHAPTER

I. Introduction 1

1.1 Why do we care about this anyway? 2
1.2 Ideal Magnetohydrodynamics 3
1.3 The Solar Interior 6
1.4 The Solar Cycle and Solar Dynamo 11
1.5 The Solar Corona 17
1.6 The Solar Wind 21
1.7 Heating of the Solar Corona 27
1.8 Coronal Mass Ejections 30
1.9 The Heliosphere 36
1.10 The purpose of this work 41

II. A Global MHD Model for the Solar Corona 43

2.1 The Ambient Solar Wind 43
2.2 The BATS-R-US Code 46
2.3 The Space Weather Modeling Framework 57
2.4 Numerical Model for the Solar Corona and Heliosphere 59
2.5 Validation of the MHD Model 68
2.6 Discussion on the Results of the MHD Model 80
2.7 Conclusions for the MHD Model 82
2.8 Model Solution with Fisk's Heating Function 83

III. Magnetic Reconnection Processes in the Solar Corona 85

3.1 Magnetic Reconnection Processes and the Solar Meridional Flow 85
3.2 Physical Model 89
3.3 Simulation Results 94
3.4 Discussion on the Flux-transport Model 102

IV. Simulation of a Sun-to-Earth Space Weather Event 104

4.1 Simulation of the May 12, 1997 event 106
4.2 Discussion of the Initial Results 114
4.3 Improved Simulation 118
4.4 Conclusions for the Simulation of a CME Event 125

V. Conclusions and Future Work 126

5.1 Summary of this Work 126
5.2 Future Work 127

APPENDICES **128**

BIBLIOGRAPHY **136**

LIST OF FIGURES

Figure

1.1 The H-R diagram, which describes the life cycle of stars in terms of its luminosity and temperature (taken from http://spaceknowledge.net/). 6

1.2 Different regions of the solar interior (from Carroll and Ostlie [17]). 9

1.3 Density (top), temperature (middle), and temperature gradient (bottom) structure of the solar interior based on Dalsgaard helioseismology model (taken from http://solarscience.msfc.nasa.gov). 10

1.4 The latitude of sunspots over time. Positive polarity is shown in yellow, while negative polarity is shown in blue. One can see that the polarity reverses every 11 years. This figure was taken from http://solarscience.msfc.nasa.gov/dynamo.shtml 12

1.5 The solar dynamo process as presented in Babcock [8]. 12

1.6 Interchange reconnection of CMEs with the open flux leads to a field reversal (Owens et. al [72]). 15

1.7 The evolution of the magnetic pole heliographic position (black line) and the two "average sunspots" position (red and blue lines) in the dipole frame. 16

1.8 Plasma can freely flows along open field lines, while it is trapped in close field lines. 18

1.9 Observational based models for electron density of the corona in different regions (from Aschwanden [7]). 19

1.10 Temperature structure in the solar corona as a function of height (taken from Trina Coleman's webpage). 20

1.11 The possible mathematical solutions from eq. 1.9. 23

1.12 Different solutions for the flow speed for different base temperatures from Parker, 1958 [73]. 24

1.13 Ulysses measurements of the solar wind speed as a function of heliolatitude for solar minimum (left) and for solar maximum (right). The bi-modal structure of the solar wind is clear during solar minimum, while it is more structured during solar maximum (from: McComas et al. [65]). 26

1.14 Different models for coronal heating at the chromosphere and at the corona (from Aschwanden 2004 [7]). 29

1.15 The four main observable features of CMEs. The white light brightening due to plasma accumulation at the CME front (a), $H\alpha$ emissions from prominence eruption (b), chromospheric $H\alpha$ ribbons (c) and X-ray loops (d) (taken from Forbes 2000 [34]). 31

1.16 Schematics of the CME features (taken from Forbes 2000 [34]). 31

1.17 An example of a shear-arcade model - the "breakout" model taken from Lynch et. al 2004 [59]. The arcade interacts with the overlaying field. 34

1.18 An example of a flux-rope model taken from Roussev et. al 2003 [82]. The initial flux rope goes unstable and erupts. 35

1.19 Eruption of a three-dimensional emerging magnetic flux rope as a model for CMEs by W. B. Manchester [62]. Panel (a) illustrates the Lorentz force, which drives the shear flows producing the eruption. Here, magnetic stream lines (confined to the $y-z$ plane at the central cross section of the rope) are drawn as white lines while black lines show the direction of the current density. The existence of the Lorentz force ($\mathbf{j}\times\mathbf{B}$) out of the plane is clearly seen where the field and current density are oblique. The magnetic field crosses $\mathbf{j}$ in opposite directions on opposite sides of the rope producing the shear stress. The horizontal cross-field current is the result of the large vertical gradient in the axial magnetic field component shown in color. The horizontal shear velocity, which clearly occurs where $\mathbf{j}$ and $\mathbf{B}$ are non-parallel is shown in Panel (b). Panel (c) shows Lorenz-force-driven shear flows driving an eruption in a magnetic arcade, which also explains CMEs. 35

1.20 The different regions in the heliosphere with the location of the Voyager 1 and 2 spacecrafts (taken from NASA's website). 36

1.21 The Parker spiral, streamlines, and magnetic field lines configuration for different heliolatitudes. (taken from NASA's website). 38

1.22 A schematics of the Fisk model (left). Ω marks the rotation axis of the Sun, M marks the magnetic axis and P marks the magnetic field line originated from the solar pole. The middle figure shows the unperturbed Parker spiral, and the right figure shows the modified spiral due to differential rotation. 41

2.1 The normal fluxes, $\mathbf{F}$ flowing through the faces of the cells. 48

2.2 Cell enumeration around the refinement interface [93]. 49

2.3 The block structure of BATS-R-US . Large cell blocks require the same amount of computation as small cell blocks. Each block is provided with the required set of ghost-cells (green). 53

2.4 Schematics of the parallel architecture of BATS-R-US . Each parent block has the information from all its children blocks. 54

2.5 An example of of the AMR throughout a simulation of the Earth's magnetosphere from the initial grid state (top-left) to the final grid state (bottom-right). 56

2.6 Module structure and coupling architecture of the SWMF. 58

2.7 Examples of the three-dimensional structure of the coronal magnetic field computed using the potential field approximation from Altschuler & Newkirk, 1969 [2]. 62

2.8 The spatial distribution of γ used in our model. γ is specified on the solar surface using the Bernoulli integral and been interpolated to spherically uniform value of 1.1 at $r = 2.5R_\odot$. γ is linearly varied to a value of 1.5 for $2.5R_\odot < r \leq 12.5R_\odot$. . . 65

2.9 A cut in the steady state solution for the SC during CR1922. Color contours represent the radial solar wind speed and streamlines represent the magnetic field lines. 69

2.10 A comparison of the simulation results with ACE and WIND data at 1AU for solar wind radial speed. 70

2.11 A comparison of the simulation results with ACE and WIND data at 1AU for magnetic field magnitude. 71

2.12 A comparison of the simulation results with ACE and WIND data at 1AU for plasma number density. 72

2.13 A comparison of the simulation results with ACE and WIND data at 1AU for plasma temperature. 73

2.14 A cut in the steady state solution for the SC during CR1973. Color contours represent the radial solar wind speed and streamlines represent the magnetic field lines. 75

2.15 A comparison of the simulation results with ACE data at 1AU for solar wind radial speed. 76

2.16 A comparison of the simulation results with ACE data at 1AU for magnetic field magnitude. The magnetic field from the simulation is multiplied by 2. 77

2.17 A comparison of the simulation results with ACE data at 1AU for plasma number density. 78

2.18 A comparison of the simulation results with ACE data at 1AU for plasma temperature. 79

2.19 Comparison between the results for the WSA model (left) and Fisk's model (right) for the final speed distribution (top) and the steady-state solution for the solar corona (bottom). Color contours represent the solar wind speed and streamlines represent magnetic field lines. 84

3.1 Initial distribution of the open magnetic flux (radial magnetic field) on the solar surface for solar minimum conditions (CR1908 - top) and for solar maximum conditions (CR1959 - bottom). The white dashed line marks the location of the current sheet. 93

3.2 Meridional (top) and Azimuthal (middle) components of $\mathbf{w}$ and κ (bottom) for initial distribution of solar maximum (left) and solar minimum (right). 95

3.3 Steady-state solution for solar minimum conditions with uniform diffusion (top) and with non-uniform diffusion (bottom). The white dashed line marks the location of the boundaries of the coronal holes for the case of uniform diffusion. 97

3.4 A latitudinal cut at $\phi = 180°$ for the solar minimum case at steady state. The black line represents the initial state, the blue line represents the steady state solution with uniform diffusion, and the red line represents the steady state solution with non-uniform diffusion. 99

3.5 Steady-state solution for solar maximum conditions with uniform diffusion (top) and with non-uniform diffusion (bottom). 101

4.1 Simulation results (solid curve) and WIND data (dotted curve) for the ambient solar wind conditions of CR1922. Plots are shown for solar wind speed (top-left) magnetic field (top-right) number density (bottom-left) and temperature (bottom-right) respectively. 107

4.2 Magnetogram of Carrington Rotation 1922. NOAA Active Region 8038 is shown by the black arrow. The background color indicates the radial component of the magnetic field; red color represents positive polarity, whereas blue color shows the negative magnetic polarity. The black line represents the polarity inversion line. . . 108

4.3 Zoom on the vicinity of the active region ($15°N < \theta < 30°N, 125° < \phi < 150°$). Color contours are the same as in Figure 4.2. White streamlines represent the magnetic field lines of the superimposed flux rope, black arrow represents the flux rope orientation, and red triangles represent the grid. 109

4.4 The CME propagation after 10 hours as it approaches the outer boundary of SC model, located at $24R_{\odot}$. Color contours represent flow speed and streamlines represent magnetic field lines. 110

4.5 Synthetic white-light images produced by the simulation (left) and observed LASCO C2 white-light images (right) at $t = 7:35$ (top) and $t = 8:35$ (bottom). 111

4.6 Synthetic white-light images produced by the simulation (left) and observed LASCO C3 white-light images (right) at $t = 12:51$ (top) and $t = 14:51$ (bottom). 112

4.7 Simulation results (solid curve) and WIND data (dotted curve) for the May 12, 1997 CME event. Plots are shown for solar wind speed (top-left) magnetic field (top-right) number density (bottom-left) and temperature (bottom-right), respectively. The gray lines mark the actual shock arrival time. 113

4.8 Simulation results (solid curve) and ACE data (dotted curve) for steady-state heliosphere driven by MDI magnetogram as of April 18, 2002. Plots are shown for solar wind speed (top-left) magnetic field (top-right) number density (bottom-left) and temperature (bottom-right) respectively. 116

4.9 Simulation results (solid curve) and ACE data (dotted curve) for the April 21, 2002 CME event. Plots are shown for solar wind speed (top-left) magnetic field (top-right) number density (bottom-left) and temperature (bottom-right), respectively. The gray lines mark the actual shock arrival time. 117

4.10 A comparison of the steady state simulation results (red line) with WIND data (blue line) for Solar wind radial speed (top left), magnetic field (top right), number density (bottom left), and temperature (bottom right) three days prior to the CME arrival. 118

4.11 Synthetic white-light images produced by the simulation (left) and observed LASCO C2 white-light images (right) at $t = 7:34$ (top) and $t = 8:33$ (bottom). White arrows mark the CME front. 120

4.12 Synthetic white-light images produced by the simulation (left) and observed LASCO C3 white-light images (right) at $t = 12:51$ (top) and $t = 14:51$ (bottom). The orientation of the CME seems to be twisted by 90 degrees due to interaction with the ambient magnetic field. 121

4.13 The CME in the corona after 10h of simulation time from the top, side and front. Color contours represent the solar wind speed, while iso-surface represent a density ratio of 4 between the current and initial density. 123

4.14 A comparison of the simulation results (black line) with WIND data (blue line) for Solar wind radial speed (top left), magnetic field (top right), number density (bottom left), and temperature (bottom right), respectively. The gray lines mark the actual shock arrival time. 124

B.1 The geometry of the RS7 fan and side discontinuities. 135

LIST OF TABLES

Table

1.1 Physical properties of the Sun 6

1.2 Energy Requirements for a Moderately Large CME 32

1.3 Estimates of Coronal Energy Sources 32

2.1 Statistics for solar minimum results. 74

2.2 Statistics for solar maximum results. 80

LIST OF APPENDICES

Appendix

A. Physical Constants and Notation 129

B. The Roe Solver 130

CHAPTER I

Introduction

"Here comes the Sun, to do do do, here comes the Sun..."

George Harrison

Since the dawn of time, people realized the Sun is essential for life to exist and worshiped it as one of their main gods. From the Greek, Roman, and Celtic cultures in Europe, the Egyptian and Mesopotamian cultures in the Middle East, the ancient Indian and Chinese cultures in Asia, and the ancient cultures in the Americas, the Sun always played a central role in the life of people.

Until the 16^{th} century, the Sun was thought to orbit the Earth just like the planets. Nicolaus Copernicus was the first to suggest that the Earth orbits the Sun, an idea that had theological consequence and raised strong opposition from the Christian church. Later on, partially due to the invention of the telescope, this idea became more and more acceptable. During the 1700s and 1800s, people began to continuously observe the behavior of sunspots, and in addition, people began to reveal the spectroscopic properties of the Sun after Sir Isaac Newton discovered that the light of the Sun is composed of different colors using a prism.

The Sun's source of energy was unknown for long time. Sources such as chemical burning and meteorite hits were proposed to explain the solar heat. However, these

sources could not last long enough, in particular following geological discoveries that revealed that the age of the Earth is about 4.5 billion years.

Our current understanding of the Sun is a result of the discovery of quantum and nuclear physics, as well as improved astrophysical understanding. In the first half of the 1900s, people realized that the Sun is a standard star, just like the stars we observe in the sky, and that the source of energy in the Sun is due to nuclear fusion reactions that take place in the solar core. This theory about nuclear burning could explain the age of the Sun and a complete theory about solar and stellar evolution had been developed between the 1940s to the 1960s. The historical evolution of each particular subject is described in separate section of the introduction.

1.1 Why do we care about this anyway?

In the modern era, we know that the Sun drives life on earth. In addition, we live in a time when understanding the space environment between the Sun and the Earth becomes more and more important. Most of the material in this region of space exists in the form of ionized gas, which we call "plasma". About 99% of the known universe (i.e. the ordinary baryonic matter) is in the form of plasma, so it is important to understand the behavior of this state that is sometime called "the fourth state of matter".

So why do we care about it? Because it is interesting!!! Plasma is an ionized gas that behaves differently than neutral gas and has some unique properties. One of the most important properties of plasma is that it is unstable and does not like to stay still. This fact makes it very hard to perform laboratory experiments with plasma. For this reason, the natural environment of space becomes the actual laboratory to study plasma physics. Plasma exists in space and in the Sun in extreme conditions

that are almost impossible to create in laboratory such as, very high temperatures, very low density, very fast speeds and very strong magnetic fields. This is what makes the space environment the "playground" of plasma physicists.

On the practical side, our growing dependency on space technology and the growing space exploration makes it very important for us to understand the space environment in order to learn how to predict its behavior. The field of space physics, which started as a niche of astrophysics or of geosciences, has become a major, independent field of physics with its own sub-disciplines such as: solar interior physics, solar corona and heliospheric physics, magnetospheric physics, ionospheric physics and even more. Some practical implementations of space physics are discussed and demonstrated in detail in this work.

1.2 Ideal Magnetohydrodynamics

The physical description of any hydrodynamic system is done using a set of conservation laws for the mass (or mass density, ρ), the momentum density ($\rho\mathbf{u}$), and the energy density of the fluid. This set of conservation laws is commonly known as the *Euler equations* for invicsid fluids, or the *Navier-Stokes equations* for viscous fluids. In the case of conducting fluid, the Euler equations are coupled with Maxwell's equations, which describe the evolution of the electromagnetic field. This coupling enables us to treat the plasma as a single conducting fluid with the lowest level approximation of the ideal MagnetoHydroDynamics (MHD). Other higher level approximations are resistive MHD, in which we keep the diffusion term in the induction equation, hybrid treatment, which separates electrons from ions, and a fully kinetic treatment [39].

The main assumptions under the ideal MHD approximation are:

1. **Quasi-neutrality** - we assume that the plasma is composed of electrons and ions, but their numbers are equal on the scale larger than the shielding scale of a test charge called Debay length: $\lambda_D^2 = \frac{\varepsilon_0 kT}{e^2 n_0}$, where ε_0 is the permittivity in vacuum, T is the temperature, k is the Boltzmann constant, e is the elementary charge, and n_0 is the plasma number density. This way the plasma shields any local charge within it.

2. **Infinite conductivity** - we assume that the plasma responds very quickly to slow variations in the large scale fields or to fluid advection. This assumption leads to the *frozen-in* concept, in which the magnetic field and the particles are glued to each other and move together. Therefore, the conductivity, $\sigma_0 \to \infty$ so we can drop the diffusion term in the induction equation, $\eta_m = \frac{1}{\sigma_0 \mu_0}$, and we can also obtain the relation $\mathbf{E} = -\mathbf{u} \times \mathbf{B}$ (also called Ohm's law).

3. **Non-relativistic motion** - We assume that all motions in the system are non-relativistic so we can ignore high-frequency variations in $\mathbf{E}$. Therefore, we can neglect the displacement current in Ampere's law and obtain: $\frac{\nabla \times \mathbf{B}}{\mu_0} = \mathbf{j}$.

4. **Local thermodynamic equilibrium** - we assume that variations in temperature are slow and that the particle distribution is Maxwellian for a given temperature.

5. **Five-moment approximation** - we assume that the pressure can be described in a scalar matter and that stress and heat flow are negligible.

Under all the assumptions above, together with neglecting gravitational effects, we can obtain the set of ideal MHD equations in conservative form [40]:

$$
\begin{aligned}
&\frac{\partial \rho}{\partial t} + \nabla \cdot (\rho \mathbf{u}) = 0 \\
&\frac{\partial \rho \mathbf{u}}{\partial t} + \nabla \cdot \left(\rho \mathbf{u}\mathbf{u} + p\mathbf{I} + \frac{B^2}{2\mu_0}\mathbf{I} - \frac{\mathbf{B}\mathbf{B}}{\mu_0} \right) = 0 \\
&\frac{\partial \mathbf{B}}{\partial t} + \nabla \cdot (\mathbf{u}\mathbf{B} - \mathbf{B}\mathbf{u}) = 0 \\
&\frac{\partial \mathcal{E}}{\partial t} + \nabla \cdot \left[\left(\mathcal{E} + p + \frac{\mathbf{B}\cdot\mathbf{B}}{2\mu_0} \right) \mathbf{u} - \frac{1}{\mu_0}(\mathbf{B}\cdot\mathbf{u})\mathbf{B} \right] = 0 \quad ,
\end{aligned}
\tag{1.1}
$$

where $\mathcal{E} = \frac{p}{\gamma - 1} + \rho \frac{\mathbf{u}\cdot\mathbf{u}}{2} + \frac{\mathbf{B}\cdot\mathbf{B}}{2\mu_0}$.

The ideal MHD approximation is very useful in describing the large-scale behavior of plasma as a fluid. However, this approximation fails to describe local and kinetic effect that are very important in plasma physics. The main phenomena that cannot be described by the ideal MHD approximation are magnetic reconnection, viscous effects, and physical effects that requires resolution higher than the Larmor radius (the gyration radius of charged particles around a magnetic field due to the Lorentz force). In order to treat these physical effects one must use higher-order approximation such as: kinetic treatment of the plasma, resistive MHD, Hall MHD, or hybrid methods that treat electrons and ions in separate manner.

1.3 The Solar Interior

The Sun is a typical main sequence G type star (a star absorbs strong metallic lines in its spectrum), which is located in the middle of the H-R diagram (seen in Figure 1.1).

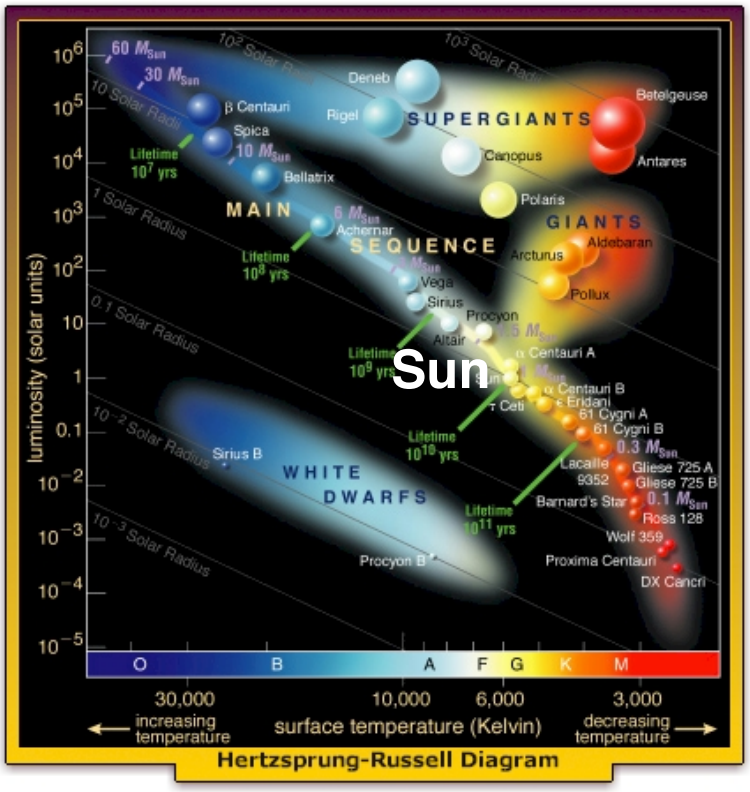

Figure 1.1: The H-R diagram, which describes the life cycle of stars in terms of its luminosity and temperature (taken from http://spaceknowledge.net/).

Table 1.1 sumarises some of the physical properties of the Sun.

Table 1.1: Physical properties of the Sun

Quantity	Symbol	Value
Mass	$M_\odot$	$1.99 \times 10^{30}\ kg$
Radius	$R_\odot$	$6.96 \times 10^{8}\ m$
Mean density	$\rho_\odot$	$1.41 \times 10^{3}\ kg\ m^{-3}$
Surface gravitational acceleration	$g_\odot = \frac{GM_\odot}{R_\odot^2}$	$275\ m\ s^{-2}$
Effective blackbody temperature	T_{eff}	$5,770\ K$
Luminosity	$L_\odot$	$3.83 \times 10^{26}\ W$
Equatorial rotation period	$T_\odot$	$25.8\ days$
Equatorial angular velocity	$\Omega_\odot$	$2.8 \times 10^{-6}\ rad\ s^{-1}$

1.3.1 Thermonuclear Reaction and the Solar Core

The Sun was born in an interstellar gas cloud, which contains mostly hydrogen but also heavier elements. Gravitational forces caused local instabilities in the cloud that generated contractive conservation of angular momentum around some center of mass. These local instabilities evolved to form an accretion disk. At the center of the disk, the increase in mass led to an increase in pressure and temperature. At some point, when the temperature exceeded about 2 million degrees, the pressure was so high that the Hydrogen nuclei merged to begin the following thermonuclear process:

$$
\begin{aligned}
{}^1H + {}^1H &\rightarrow {}^2D + e^+ + \nu + 1.442\ MeV \\
{}^2D + {}^1H &\rightarrow {}^3He + \gamma + 5.493\ MeV \\
{}^3He + {}^3He &\rightarrow {}^4He + {}^1H + {}^1H + 12.859\ MeV \\
4{}^1H &\rightarrow {}^4He + 2e^+ + 2\nu + 26.73\ MeV,
\end{aligned}
\tag{1.2}
$$

where H is an hydrogen atom, D is a deuterium atom, He is an Helium atom, e^+ is a positron, ν is a neutrino, and γ is a gamma ray. In this set of reactions, for each transformation of four ${}^1H$ atoms to a ${}^4He$ atom, we are left with an energy of $26.73\ MeV$. This excess energy balances the inward gravitational force so the Sun reaches steady-state where the fusion process is taking place inside 0.2 of the solar radius. The steady-state will remain as long as the hydrogen is burnt in the solar core. This supply of hydrogen should cease in about 5 billion years and then the Sun will become a red giant and it will loose most of its material. The remaining material of the Sun will form a white dwarf, which is very dense body that cools down with time. This will be the end state of our Sun.

1.3.2 Thermal Structure of the Radiation and Convection Zones

The energy produced in the solar core is transported to the surface via radiation or convection. Radiation transport is the case, in which photons carry the energy by being absorbed and re-emitted from the solar matter in random direction. Convection is the case when hot cells of material rise to the surface, cool down and sink back to the hot bottom (similar to the motion of boiled water). Heat conduction, in which the the energy is transferred through particle collisions is not important in the solar interior but can occur in principle in collisionless plasma.

The radiation zone extends between $0.2 - 0.75 R_{\odot}$. The radial pressure gradient can be written in terms of the temperature gradient:

$$\frac{dP_{rad}}{dr} = \frac{4}{3} a T^3 \frac{dT}{dr}, \tag{1.3}$$

with the radiation constant $a = 4\sigma/c = 7.565 \times 10^{-16}\ J\ m^{-3}\ K^{-4}$. The radiative temperature gradient is:

$$\left|\frac{dT}{dr}\right|_{rad} = -\frac{3}{4ac} \frac{\bar{\kappa}\rho}{T^3} \frac{L(r)}{4\pi r^4}, \tag{1.4}$$

where $\bar{\kappa}$ is an opacity coefficient. In the radiation zone, the temperature structure is governed by radiation. However, at $r \approx 0.75 R_{\odot}$, the temperature gradient becomes so steep and the transfer of energy by radiation is not sufficient and convection takes over. Convection dominates when the temperature gradient is larger than the adiabatic temperature gradient defined as:

$$\left|\frac{dT}{dr}\right|_{ad} = -\frac{g_{\odot}}{C_p}. \tag{1.5}$$

Here C_p is the specific heat at constant pressure. The boundary between the radiation and convection zones is called the "tachocline" and above it heat is transferred to the surface in convective cells. New helioseismology measurements observed strong

radial shear and a transition from solid rotation to differential rotation in this region. Figure 1.2 shows the different layers of the solar interior.

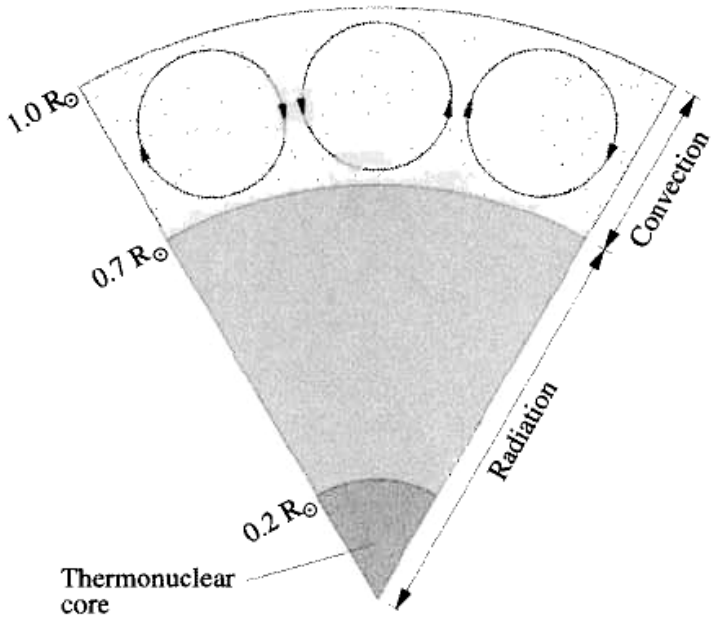

Figure 1.2: Different regions of the solar interior (from Carroll and Ostlie [17]).

Figure 1.3 shows the density, temperature, and temperature gradient structure of the solar interior.

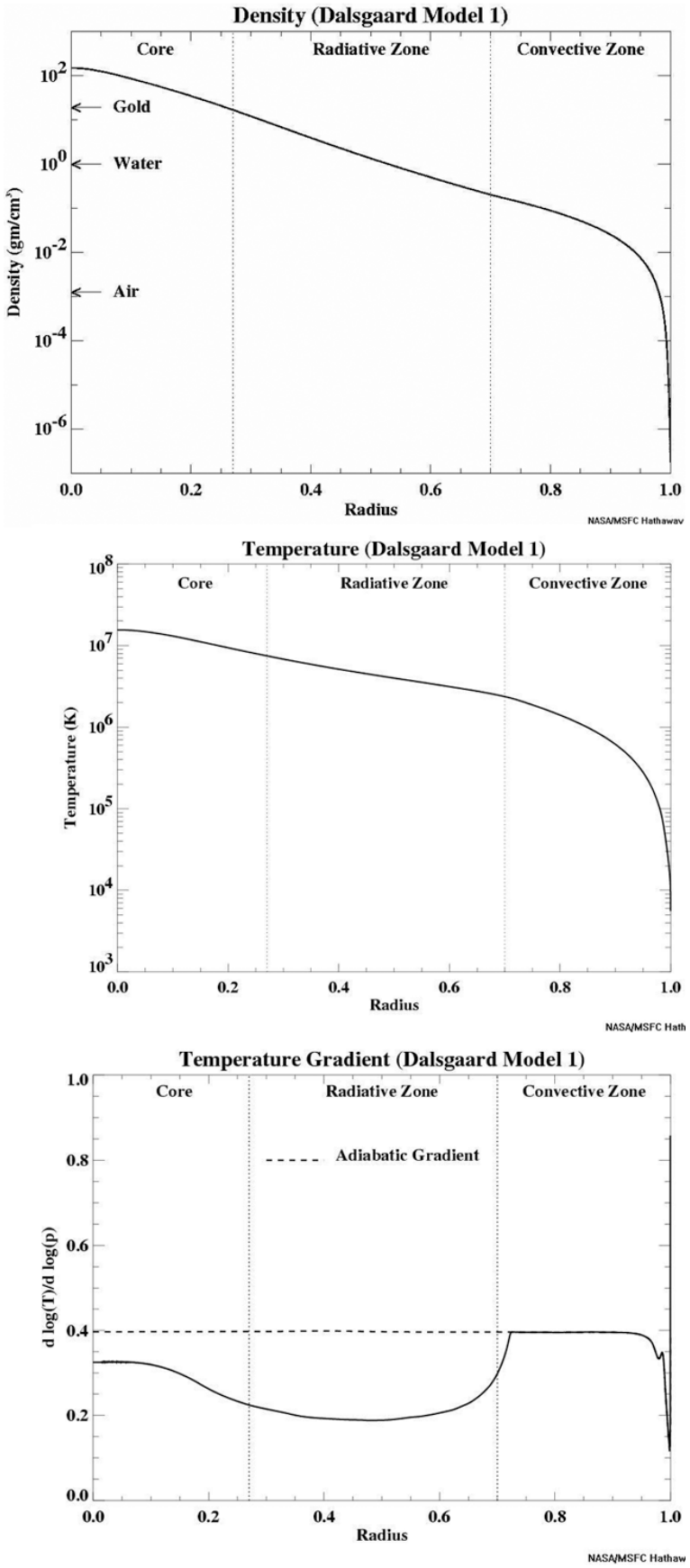

Figure 1.3: Density (top), temperature (middle), and temperature gradient (bottom) structure of the solar interior based on Dalsgaard helioseismology model (taken from http://solarscience.msfc.nasa.gov).

1.4 The Solar Cycle and Solar Dynamo

One of the most ancient measured natural signals is the number of sunspots on the surface of the Sun. Sunspots are regions on the Sun that appear to be darker than the surrounding area due to lower temperature. In modern days, we know that the reason for the appearance of these sunspots is the existence of strong magnetic flux tubes in the spots. The strong magnetic pressure prevents the hot plasma from bellow to rise and as a result, the spots are colder than the surrounding area.

New observations in the 20^{th} century led to the general understanding that the magnetic field of the Sun has a dipolar configuration when the number of sunspots is smaller (solar minimum) and it is more structured during the time when the number of sunspots reaches its peak (solar maximum). During solar minimum conditions, the Sun is more quiet and less active. During solar maximum however, the Sun is more active and this is the time when the magnetic field reverses. Another observation of sunspots is that they appear in higher latitudes (about 30 degrees from the equator) at the beginning of the cycle and they seem to migrate to lower latitude as the cycle progresses. By plotting the latitudes of the sunspots over time, we can obtain the famous "Butterfly Diagram" shown in Figure 1.4.

In 1961, Babcock [8] presented a complete conceptual description for the solar dynamo process (the process in which the solar magnetic field does not diffuses away). The initial state is of a pure poloidal (meridional) field . Differential rotation converts the poloidal component to a torodial (azimutal) component through the process called the "Omega Effect". In the next step, the toroidal flux tubes are twisted as they emerge to the surface through the process called the "Alpha Efect". Due to the orientation of the Coriolis force, the twisted flux tubes appear on the

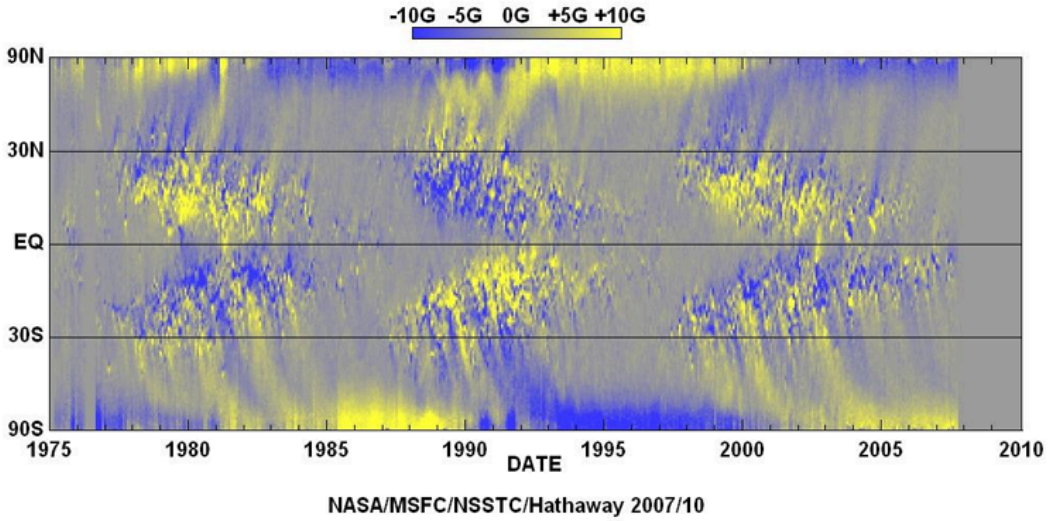

Figure 1.4: The latitude of sunspots over time. Positive polarity is shown in yellow, while negative polarity is shown in blue. One can see that the polarity reverses every 11 years. This figure was taken from http://solarscience.msfc.nasa.gov/dynamo.shtml

solar surface with a polarity opposite to the polarity of the ambient field. As more and more flux tubes emerge to the surface, the dipolar component of the large scale field breaks down and higher harmonics of the magnetic field appear. This process requires the existence of meridional flow that transport the two footpoints of the small loops to higher and lower latitudes, respectively. At the end of the process, the field configuration returns to a pure poloidal one but with opposite polarity.

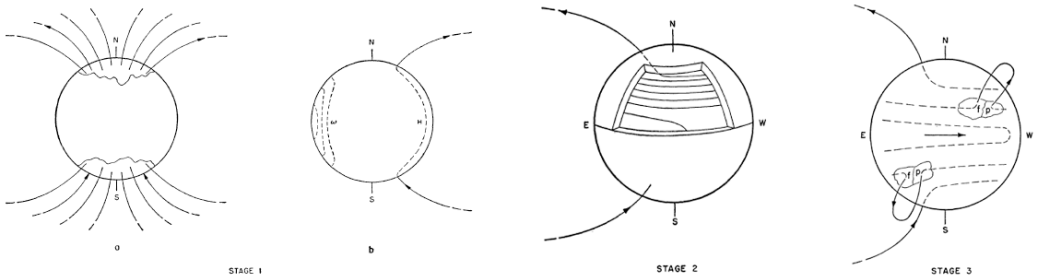

Figure 1.5: The solar dynamo process as presented in Babcock [8].

In the past two decades or so, a number of numerical models have been developed to investigate the evolution of the solar magnetic field. The models can be divided

into two types. Models of the convection-zone (the dominant models have been developed at HAO by Gilman and Dikpati, and others), and surface flux-transport models (dominated by the work of Wang and Sheeley at NRL, and Schrijver et al.). In general, the convection-zone type of models calculates the general circulation of the magnetic field with observed velocity field. In practice, these models solve the non-linear, two or three dimensional induction equation. Flux-transport models calculate the two dimensional surface transport of the magnetic field. They usually include differential rotation, meridional flow and uniform diffusion (following Leighton, 1964 [53]). Both types of models have been significant to our understanding of the solar magnetic field and they were able to reproduce the butterfly diagram, the Maunder minimum, and the general behavior of the evolution of the solar magnetic field.

There are two major problems with the current models for the solar dynamo. First, they deal only with the evolution of the "mean" magnetic field and do not solve the complete set of MHD equations for the system. Second, they cannot treat the pressure stratification of the interior or account for diffusion. Third, and more important, none of the above models do not take into account the role of the three dimensional coronal and heliospheric magnetic field in the long-term evolution of the magnetic field of the Sun. Even the theoretical dynamo models do not take into account the so-called open magnetic field which is dragged by the solar wind to the heliosphere, since this component is neither poloidal nor toroidal. In order to investigate the role of the heliospheric flux in the evolution of the solar magnetic field we must couple the convection zone, the corona and heliosphere together. We are far from being able to perform coupled numerical simulation of the complete system. However, the new numerical frameworks and advances in computation resources may provide the required capabilities in the near future.

Recent theories suggest how the open flux can affect the evolution of the large-scale magnetic field [32, 72]. The principle idea is that magnetic reconnection with open and closed field lines causes an effective transport of the open flux until the large-scale field is reversed. The idea that reconnection with closed loops leads to a general circulation of the open flux proposed by (Fisk et al. [32, 30, 31]) in a series of papers and we discuss this model in detail in Chapter III.

Owens et. al [72] suggested that interchange reconnection of CMEs with the heliospheric open flux can transport the open flux as well and the field reversal. This theoretical concept is shown in Figure 1.6. In the Babcock model, new magnetic flux emerges to the surface with polatiry opposite to the polarity of the ambient flux and as a result, the ambient flux is destroyed. However, the Babcock model does not describe the detailed mechanism in which the destruction of the flux is done. In the Fisk model, the interaction of the new flux with the surrounding flux is done through continuous reconnection at all heights and scales. In the model proposed by Owens et al., the new flux appears in active regions and it is transported by CMEs and the interaction with the ambient open flux takes place in the upper corona and heliosphere.

Figure 1.7 shows an initial result of sunspot data analysis. I averaged the latitude of sunspots data, taken from Mt. Wilson and USAF/NOAA web sites, over each Carrington Rotation for each hemisphere. This way I can track an "average sunspots" for each hemisphere. I then calculated the magnetic pole location in the heliographical frame using the g_1^0, g_1^1, and h_1^1 harmonics of the magnetic field expansion taken from WSO website [35]. Once the pole coordinates are known, we can transform the heliographic latitudes of the sunspots to the heliomagnetic frame; this transformation gives us the location of the average sunspots in the dipole frame. Figure 1.7

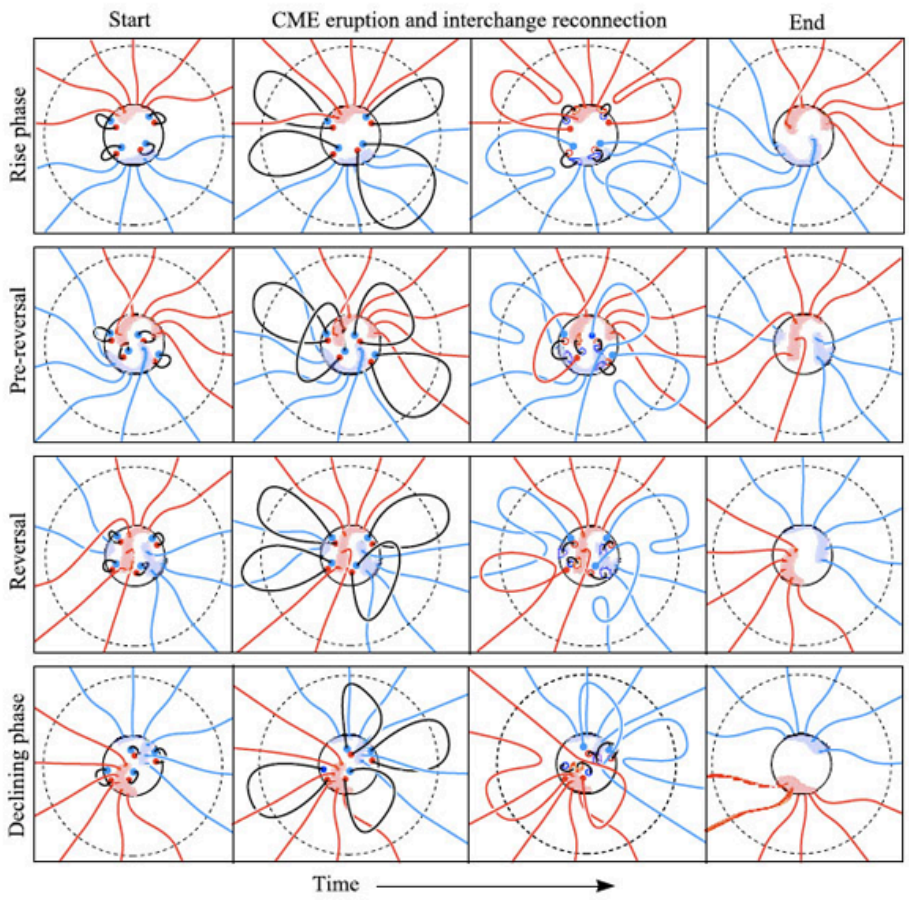

Figure 1.6: Interchange reconnection of CMEs with the open flux leads to a field reversal (Owens et. al [72]).

shows the heliographic location of the magnetic pole (black line) and the latitude of the average sunspots in the dipole frame (red and blue lines). In general, the migration of the sunspot latitude is consistent with the butterfly diagram. However, the most relevant feature in the plot is the fact that the two average sunspots jump to higher latitude. This jump occurs several months before the pole starts to migrate to the other hemisphere. I do not attempt to explain the reason for the latitudinal jump of the sunspots. However, this observation supports the idea that the open flux plays a major role in the evolution of the Sun's magnetic field. As long as the sunspots (or CMEs originated from active regions) are located at low latitudes, they interact mostly with the overlaying streamers. Once the sunspots move to higher

latitudes, they begin to interact with coronal holes and destroy them. As a result, the magnetic pole starts its migration and eventually, the field reverses.

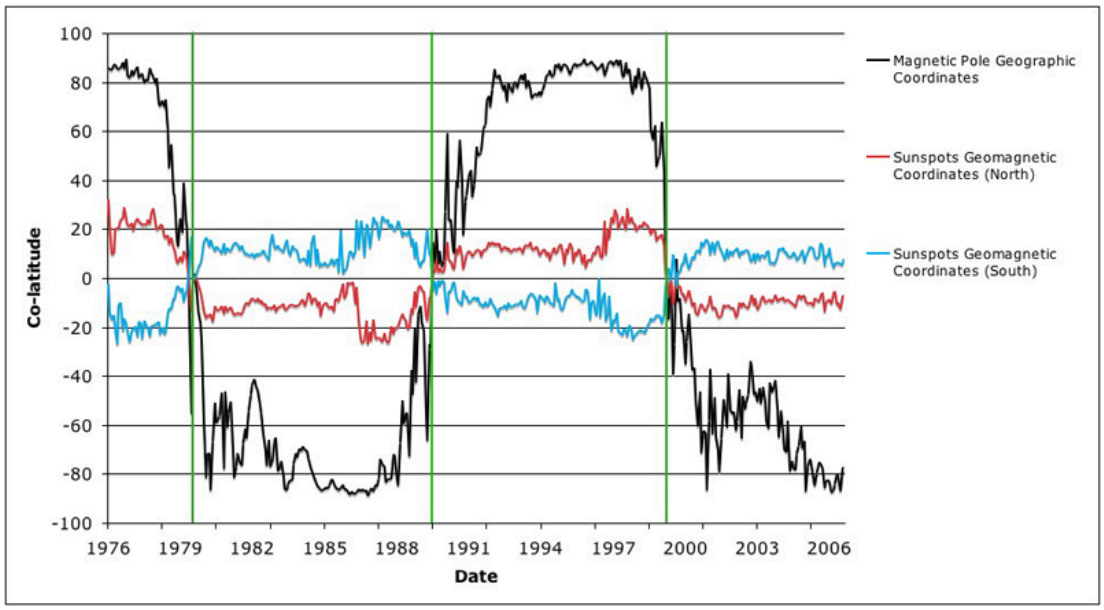

Figure 1.7: The evolution of the magnetic pole heliographic position (black line) and the two "average sunspots" position (red and blue lines) in the dipole frame.

The two models provide not only an explanation about the role of the open flux of the Sun in the reversal process, but also demonstrate how does the Sun transfer from one potential stage to another. The large-scale magnetic field of the Sun is considered to be potential field. However, the new emerging flux introduces a non-potential component, which the Sun gets rid of by reconnection processes. We are still far from fully understanding the long-term and large-scale evolution of the solar magnetic field. This work is part of the global effort to develop tools that will provide better understanding of the physical system. I believe that the key to a real understanding of the solar dynamo is to study the coupling between the convection zone and the solar corona, as well as observing stellar dynamos of other stars. The behavior of a stellar magnetic field depends on the star's basic properties. Therefore, we might learn something new just from observing and analyzing stellar cycles.

1.5 The Solar Corona

The solar atmosphere is called the "solar corona" due to its appearance during solar eclipses. When the moon covers the bright solar disk, the solar atmosphere can be seen as a halo or corona around the occulting disk of the Moon. The solar corona extends to about 10 solar radii and we call the part of the solar atmosphere that fills up the interplanetary space simply the "heliosphere".

The solar corona is dominated by the highly stratified density structure, on one hand, and by the structure of the magnetic field, on the other hand. At the photosphere, the electron density is of the order of $10^9\ cm^{-3}$ and it drops exponentially with height. The layer that extends from the photosphere to about 1.1 solar radii is called the "chromosphere". This layer is the place in which the plasma becomes fully ionized, so the gas follows magnetic field lines. This is why the density structure is not spherically uniform but is oriented with the structure of the magnetic field. In open field regions, the plasma can easily flow along the field lines so the density and temperature is relatively low. In closed field line regions, such as the helmet streamers (the closed field region), the plasma is trapped in the magnetic loops so the density and temperature are higher. This concept is shown in Figure 1.8.

Figure 1.9 shows observation based models for the electron density in different regions of the solar corona.

The temperature structure of the corona is still not fully understood. The photospheric temperature is about $5000^\circ\ K$, which matches the observed blackbody radiation. In the chromosphere, the temperature rises to about $10^4\ K$ and then it jumps to about 1 million degrees across a narrow transition zone. The astrophysics community has been puzzled with this observation for many years, since it seem

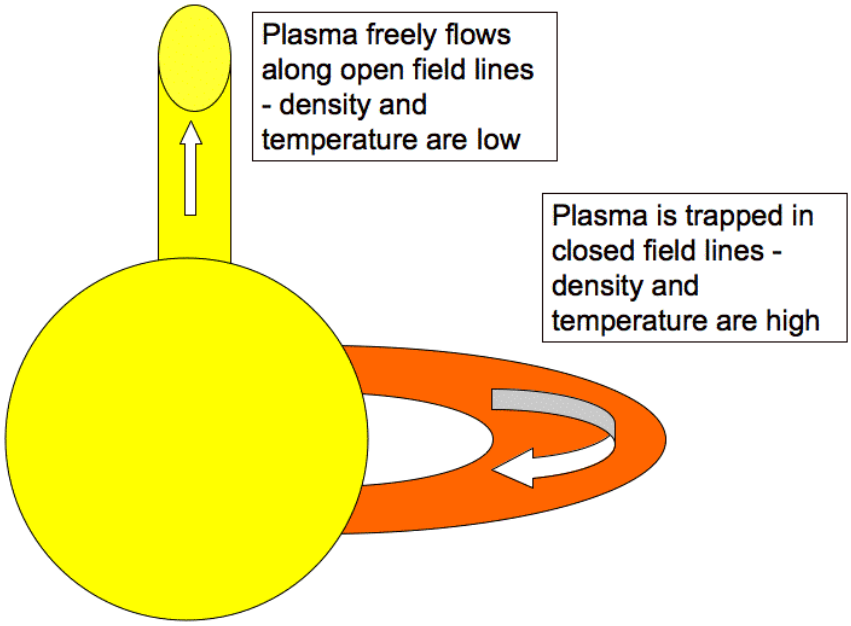

Figure 1.8: Plasma can freely flows along open field lines, while it is trapped in close field lines.

to violate the second law of thermodynamics. It is just counter-intuitive that the temperature of the solar atmosphere, which expands into space, raises to such high temperature. We know now that the heating of the solar corona is due to the combination of stratified atmosphere and the coronal magnetic field. This combination leads to a dumping of magnetic and acoustic waves that heats the corona. The exact mechanism however, is still under debate and I discuss this subject in detail in Section 1.7. Figure 1.10 shows the temperature structure of the corona.

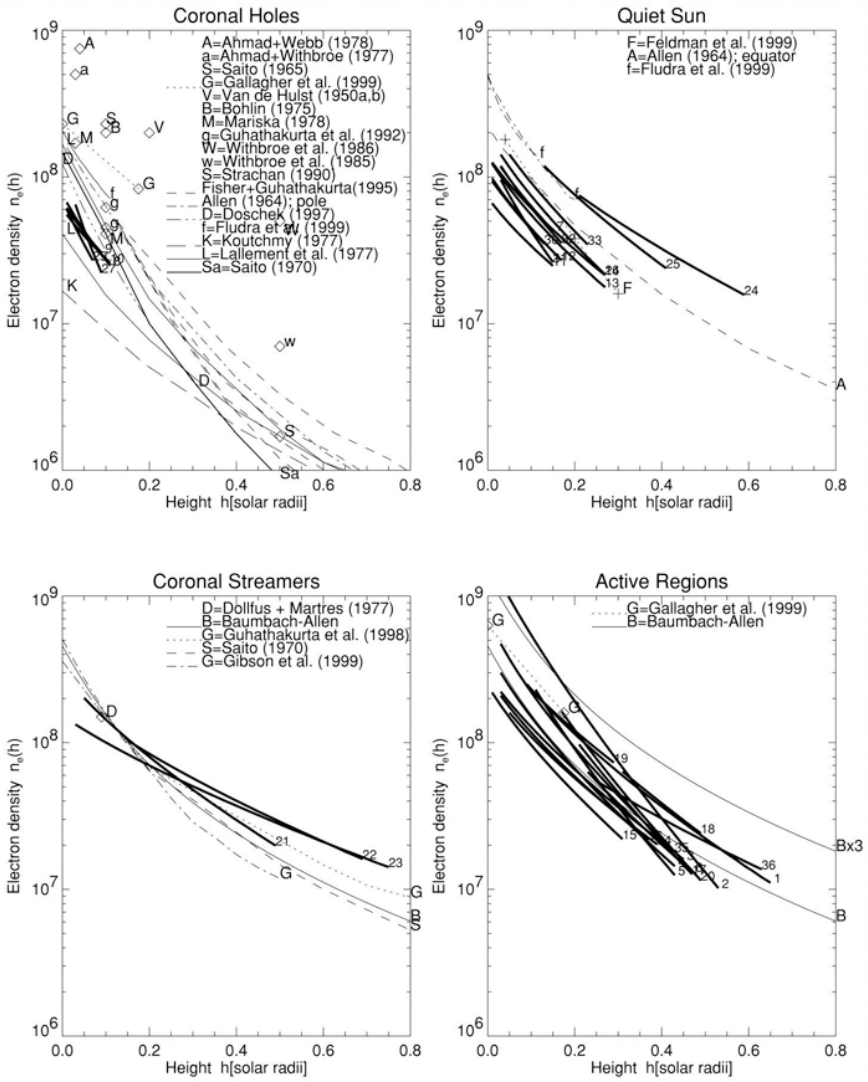

Figure 1.9: Observational based models for electron density of the corona in different regions (from Aschwanden [7]).

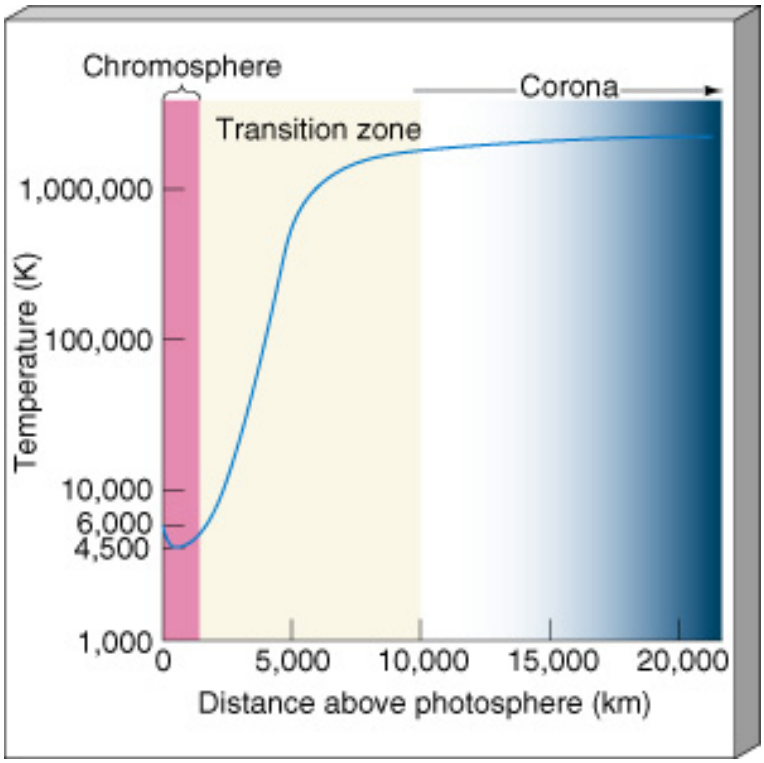

Figure 1.10: Temperature structure in the solar corona as a function of height (taken from Trina Coleman's webpage).

1.6 The Solar Wind

Until the middle of the 20^{th} century, the Sun was considered to be in a hydrostatic equilibrium. Due to its huge mass, astronomers did not believe that gas can escape the Sun's gravity. During solar eclipses, people did observe the solar corona extends up to several solar radii and in addition, people were aware of solar eruptions in which gas is released into space. These gas particles were often called "solar radiation" or "solar rays" and they were considered to be local jets that the Sun spits into a nearly empty space. In the early 1900s, Birkeland was the first to relate events on the Sun to disturbances of the Earth's magnetic field by realizing that the solar radiation must be composed of charged particles. The first spectroscopic measurements of the solar corona, revealed that its temperature is of the order of million degrees K. Sydney Chapman showed that the heat conductivity of the corona should be so high, that the corona should extend up to Earth's orbit and beyond. In 1951, Biermann suggested that comet tails always pointed away from the Sun due to a constant radiation. However, the density in his calculations was unreasonably high. Biermann's work was followed by a similar paper by Alfvèn in 1957.

1.6.1 The Hydrostatic Sun

Let us assume steady-state, spherical symmetry and let us neglect magnetic field effects and heat conduction [40]. The continuity, momentum, and energy equations become:

$$\begin{aligned} \tfrac{1}{r^2}\tfrac{d}{dr}\left(r^2\rho u\right) &= 0 \\ \rho u\tfrac{du}{dr} + \tfrac{dp}{dr} + \rho G\tfrac{M_\odot}{r^2} &= 0 \\ \tfrac{3}{2}u\tfrac{dp}{dr} + \tfrac{5}{2}p\tfrac{1}{r^2}\tfrac{d}{dr}\left(r^2 u\right) &= 0, \end{aligned} \tag{1.6}$$

If we assume that an hydrostatic solution ($u = 0$) the pressure at infinity is finite:

$$p(r \to \infty) = p_\odot \exp\left[-\frac{m_p G M_\odot}{2kTR_\odot}\right]. \tag{1.7}$$

Even with this basic problem, the idea that the Sun continuously expands was unacceptable among the astrophysics community. And than came Parker...

1.6.2 The Expanding Solar Atmosphere

In 1958 Parker solved the system of eq. 1.6 without setting u to zero. In this case, the three equations can be combined to obtain a differential equation for the speed:

$$\frac{u^2 - a_s^2}{u}\frac{du}{dr} = \frac{2a_s^2}{r} - \frac{GM_\odot}{r^2}, \tag{1.8}$$

with constant polytropic index, γ and the sound speed, $a_s^2 = \gamma\frac{p}{\rho}$. The general solution for eq. 1.8 is:

$$\frac{1}{2}u^2 - a_s^2 \ln u = 2a_s^2 \ln r + \frac{GM_\odot}{r} + C, \tag{1.9}$$

where C is a constant of integration. Eq. 1.8 can be re-written as follow

$$\frac{du}{dr} = \frac{u}{u^2 - a_s^2}\frac{2a_s^2}{r}\left(1 - \frac{U(r)}{2kT}\right), \tag{1.10}$$

where $U(r)$ is the gravitational potential. This equation introduces a singularity in the denominator when $u = a_s$ but dominator becomes zero at the same time, so by using L'Hospital's rule, it can be shown that there is a valid solution. The point in which both the dominator and the denominator become zero is called the "critical point". This is also the point where the flow becomes supersonic. Parker realized that this type of equation is exactly the same as the equation for "De Laval Nozzle" in hydrodynamics. This equation describes a subsonic flow in a nozzle that becomes supersonic at the inflection point between diverging and converging cross-sections (as in a jet engine). Figure 1.11 shows the possible solutions for the solar wind. Cases I

and II have double value solutions so they are not valid. Case III is not valid since it is supersonic at the base of the corona, and Case V provides finite pressure at infinity. The only physically valid solution is Case IV in which the flow is subsonic bellow the critical point and is supersonic above it.

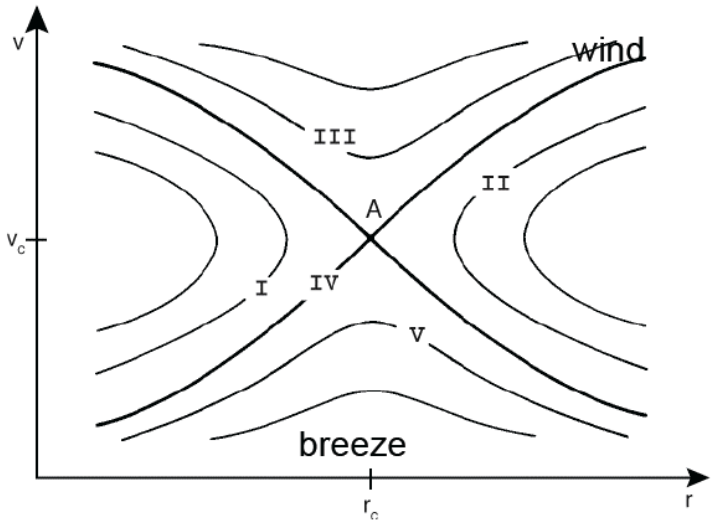

Figure 1.11: The possible mathematical solutions from eq. 1.9.

The physical reason for the solar wind is actually straightforward. The Sun is located in space where the external pressure is essentially zero, so the pressure gradient between the hot solar corona and interstellar medium is enormous. Even though the Sun's gravity is very large it cannot oppose this pressure gradient. Particles try to escape from the Sun due to the pressure gradient but gravity holds them back until they reach the critical point. At this point, the pressure gradient overcomes the gravitational force and the gas is accelerated to an asymptotic speed of $500 - 800\ km/s$. Figure 1.12 shows the different solutions for a flow speed with different base temperatures.

The hydrodynamic description of the solar wind can be written in the form of energy conservation along a streamline [74]. Parker realized that the gas in the

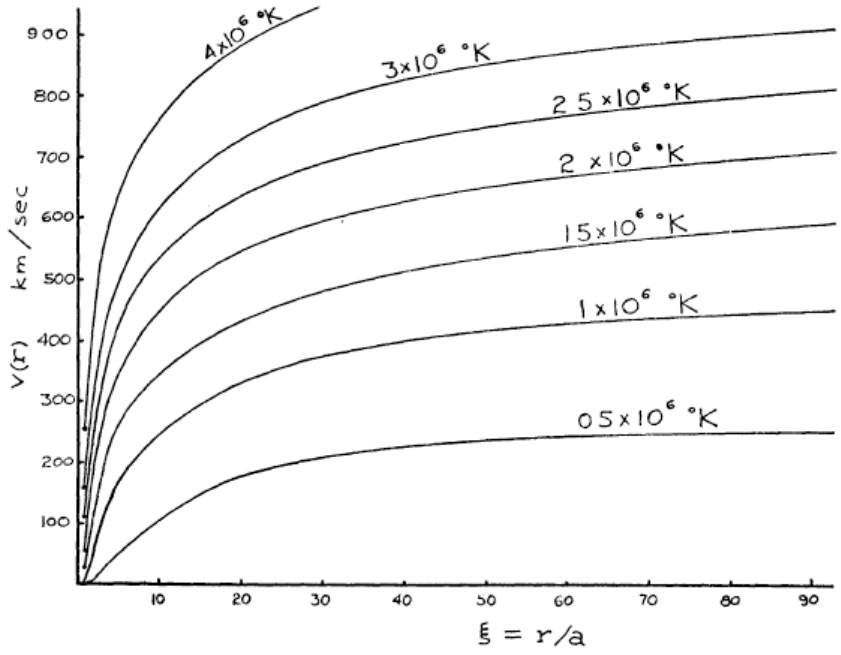

Figure 1.12: Different solutions for the flow speed for different base temperatures from Parker, 1958 [73].

corona must be highly conducting, therefore the field lines must be stretched with the flow. In this case, the energy equation can be written as follow:

$$u\frac{\partial u}{\partial l} + \frac{1}{l}\frac{\partial p}{\partial l} + \frac{\partial \Phi(l)}{\partial l} = 0, \tag{1.11}$$

where $\Phi(l)$ is the gravitational potential and l is the coordinate along the streamline path. Assuming that $p(l) = p_0 \left(\frac{\rho(l)}{\rho_0}\right)^\gamma$ and $1 < \gamma < 5/3$, we can integrate eq. 1.11 to obtain Bernoulli's integral:

$$\frac{1}{2}u^2(r) + \frac{\gamma}{\gamma-1}\frac{p_0}{\rho_0}\left[\frac{\rho(r)}{\rho_0}\right]^{\gamma-1} + \Phi(r) = \frac{1}{2}u_0^2 + \frac{\gamma}{\gamma-1}\frac{p_0}{\rho_0} + \Phi_0. \tag{1.12}$$

Here we changed the path coordinate, l, to the radial coordinate, r, and we used the notation 0 for the coronal base values. The concept of Bernoulli integral is useful in practice and it is implemented in our numerical model as a key feature. The complete description appears in Chapter II.

The idea of a continuous flow from the Sun was so revolutionary at the time,

that Parker's paper was rejected by two reviewers. Fortunately for Parker (and for us...), Subrahmanyan Chandrasekhar was the Astrophysical Journal editor and the paper was published after all. This is a unique case where good networking actually advanced science (Parker and Chandrasekhar worked together at the University of Chicago). The debate had been going on for several years until the Soviet Lunik 1 spacecraft measured the solar wind for the first time in 1961. A couple of years later, the American Mariner 2 spacecraft continuously measured the solar wind properties for three months and provided a clear proof that the solar wind exists as Parker predicted it.

Even though Parker's solar wind solution predicts the existence of a supersonic flow from the Sun, there are some issues that it cannot fully explain. The main issue is that in reality, the critical point is located much closer to the Sun than the one predicted by the hydrodynamic model. This means that there is an additional physical mechanism that accelerates the solar wind even more. The main candidate to provide the required extra energy is the coronal magnetic field. In addition, the solar wind has been observed to be bi-modal (see Figure 1.13), with fast solar wind ($u \approx 700 - 800\ km\ s^{-1}$) originating from high magnetic latitude and coronal holes, and slow solar wind ($u \approx 400\ km\ s^{-1}$) originating from the coronal holes boundaries. The two types of plasma seems to differ from each other not only in speed, but also in density, temperature, and composition. Parker's mechanism seems to work pretty well for the fast wind but it fails to explain how the slow wind is accelerated. In the next section, I will discuss the issue of the solar coronal heating and solar wind acceleration. In Section 1.9, I will discuss the consequences of the solar wind on the general structure of the Heliosphere.

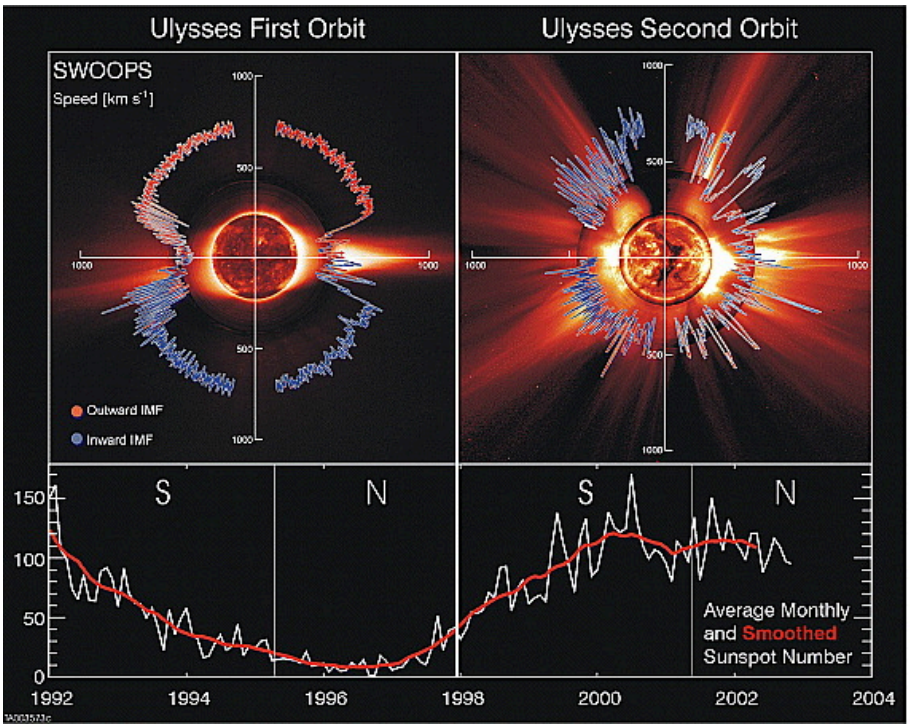

Figure 1.13: Ulysses measurements of the solar wind speed as a function of heliolatitude for solar minimum (left) and for solar maximum (right). The bi-modal structure of the solar wind is clear during solar minimum, while it is more structured during solar maximum (from: McComas et al. [65]).

1.7 Heating of the Solar Corona

The origin, acceleration, and heating of the solar wind have been debated by the solar-heliospheric community for decades. Although there is significant progress in this area, the available theoretical models for turbulent processes in the solar wind (i.e., turbulent heating) can not provide yet a reliable and quantitatively accurate agreement with the observed solar wind parameters at 1 AU. We also lack a detailed description of the three-dimensional structure of the interplanetary magnetic field, which affects the transport of solar energetic particles through the heliosphere.

The theory of origin and evolution of the solar wind is challenged by the following two fundamental problems. In the first place stands the "coronal heating" problem; the temperature in the solar atmosphere raises by two orders of magnitude from the photosphere ($T < 10^4$ K) to the corona ($T_e \approx T_i \approx 10^6$ K) across a narrow transition region [7]. The coronal plasma expands into the interplanetary space, guided by the magnetic field close to the Sun, to form the solar wind. Second, there is a discrepancy between the observed values of coronal temperature and the observed solar wind speeds in the inner heliosphere (IH), in particular at 1 AU. The solar wind at a heliocentric distance of 1 AU has a speed of $u_{sw} \sim 800$ km s^{-1}when originating from regions of open magnetic field lines; this is the so-called fast solar wind. On the other hand, the solar wind associated with regions of closed field lines (or helmet streamers), is slow, with a speed of $u_{sw} \sim 400$ km s^{-1}; this is the so-called slow solar wind. In both cases, the kinetic energy of a pair of proton and electron is much greater than their thermal energy in the solar corona (SC): $m_p(400\text{ km s}^{-1})^2/(2k_B) \approx 10^7\text{K} \gg T_e + T_i = T$. The discrepancy for the fast solar wind is more than an order of magnitude. Note that even the gravitational potential energy at the solar surface is

greater than the the thermal energy: $GM_{\odot}m_p/(R_{\odot}k_B) = 2.3{\times}10^7$ K $\gg T$. Therefore, the theory needs to explain how the solar wind plasma originates from the Sun, how it is accelerated to escape the solar gravity, and how it is further powered to reach the observed speed and the bi-modal structure in the inner heliosphere.

The most commonly accepted theory regarding heating of the solar corona suggests that the source of energy to heat and accelerate the solar wind comes from wave-particle interaction and turbulent cascade. In this theory, MHD waves with frequencies close to the particles resonant frequencies, are damped in the corona and provide the particles with the observed energies [50, 22]. It is not clear however, what are the dominant resonant frequencies. Is it ion waves? electron waves? Alfvén waves? On one hand, if the coronal heating is dominated by the minor species and heavier ions, then the heating occurs due to low frequency ion-cyclotron waves. On the other hand, observations have shown that the final solar wind speed is inversely proportional to the electron temperature [37]. This implies that the heating is driven by high frequency waves. In addition, there is an evidence that the so-called fast solar wind that originates from large coronal holes, and the slow solar wind that originates from the coronal hole boundary, are different in composition, temperature, and density. This might suggest that the acceleration mechanism for the two populations is actually not the same.

An alternative approach considers the large-scale heating as a result of small-scale magnetic reconnection processes and nanoflares that occur in the low corona [75, 30, 103]. Fisk [30] showed how local reconnection events in the corona result in a large-scale electric field, which leads to a large-scale Poynting flux to provide excess of energy to accelerate the solar wind. Fisk related this energy flux to the electron temperature, T_e, in the corona and proposed the following formula for predicting the

solar wind speed:

$$\frac{u^2}{2} = \frac{A}{T_e} - \frac{GM_\odot}{R_\odot}. \tag{1.13}$$

Here A is a constant, which depends on the mass flux carried by the solar wind. The inverse relation between the final solar wind speed and the electron temperature was confirmed observationally by Gloekler et al. [37]. Eq. 1.13 has been used in a global simulation of the solar corona and the results are presented in Section 2.8.

Even though the solar wind heating is still an open issue, the recent STEREO and HINODE missions should reveal some of the unknown physics. Figure 1.14 shows the different models for coronal heating.

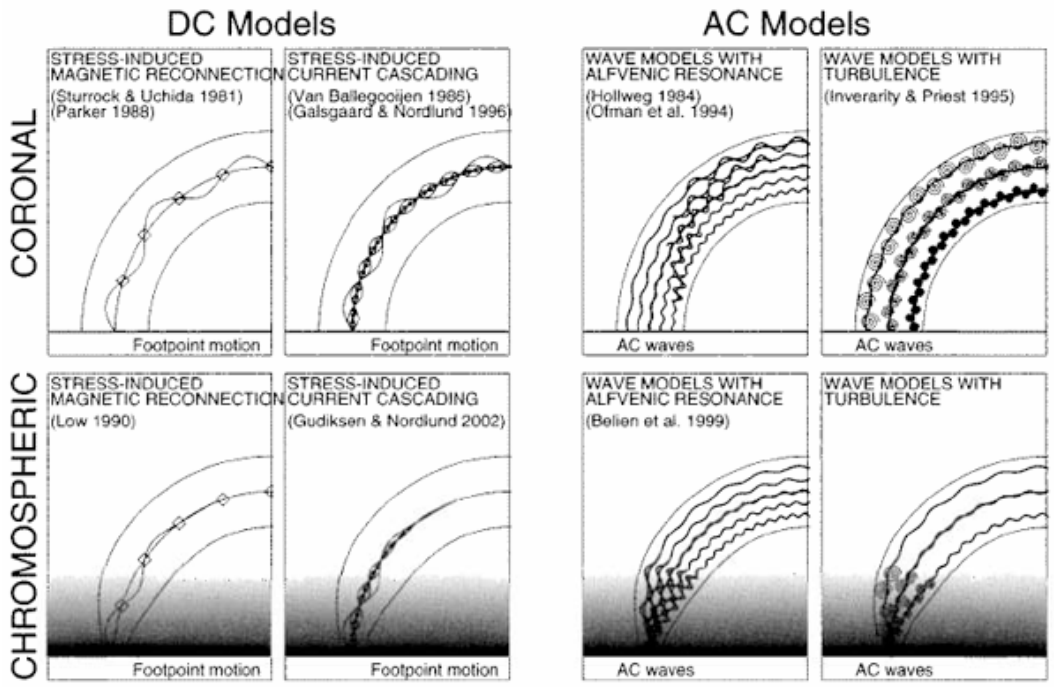

Figure 1.14: Different models for coronal heating at the chromosphere and at the corona (from Aschwanden 2004 [7]).

1.8 Coronal Mass Ejections

One of the most fascinating features among solar phenomena is Coronal Mass Ejection (CME). It had been observed in details by Skylab during the 70ŝ. In the past two decades, observations from the SOHO, TRACE, and YOHKOH satellites, and new ground-based observations have dramatically increased our knowledge about CME properties. Although the structure and evolution of CMEs is now well defined, the mechanism of CME initiation is still not fully understood. On average, CME ejects into the interplanetary space 10^{23} $Maxwells$ of magnetic flux and 10^{16} g of plasma. During the quiet phase of solar cycle there are approximately two CMEs per week and during the active period there is a CME every day. Figure 1.15 shows the four main observable features of CMEs. The white light brightening due to plasma accumulation at the CME front (a), $H\alpha$ emissions from prominence eruption (b), chromospheric $H\alpha$ ribbons (c) and X-ray loops (d).

The $H\alpha$ emissions are associated with solar flares and are cooler than the observed soft X-ray emissions since they are reflected from denser regions. Soft X-ray emissions are produced in loops with footpoints mapped into the location of the $H\alpha$ ribbons. These loops have temperature of $T > 10^7$ K and therefore the emissions are thermal in their origin. The hard X-rays are produced by non-thermal electrons and accompanied by radio signal, protons with energy up to 100 MeV are also observed. Figure 1.16 shows schematics of the CME features and their location.

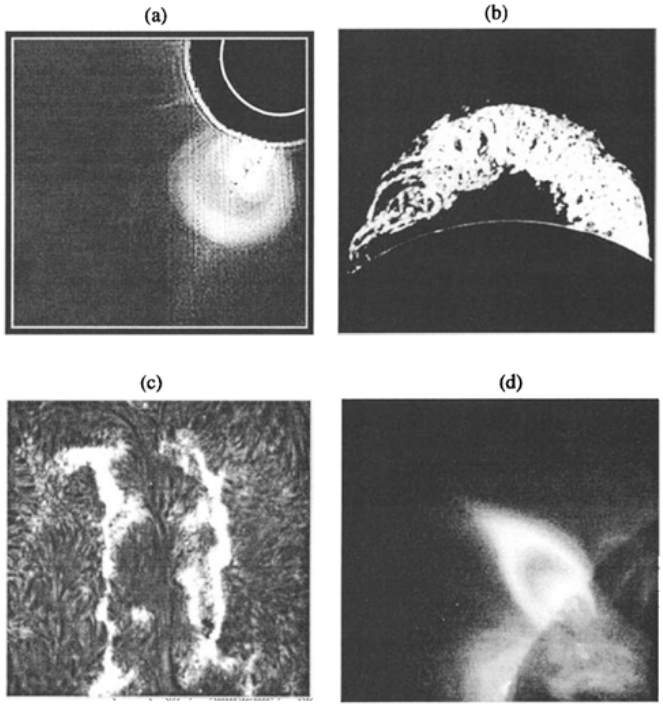

Figure 1.15: The four main observable features of CMEs. The white light brightening due to plasma accumulation at the CME front (a), $H\alpha$ emissions from prominence eruption (b), chromospheric $H\alpha$ ribbons (c) and X-ray loops (d) (taken from Forbes 2000 [34]).

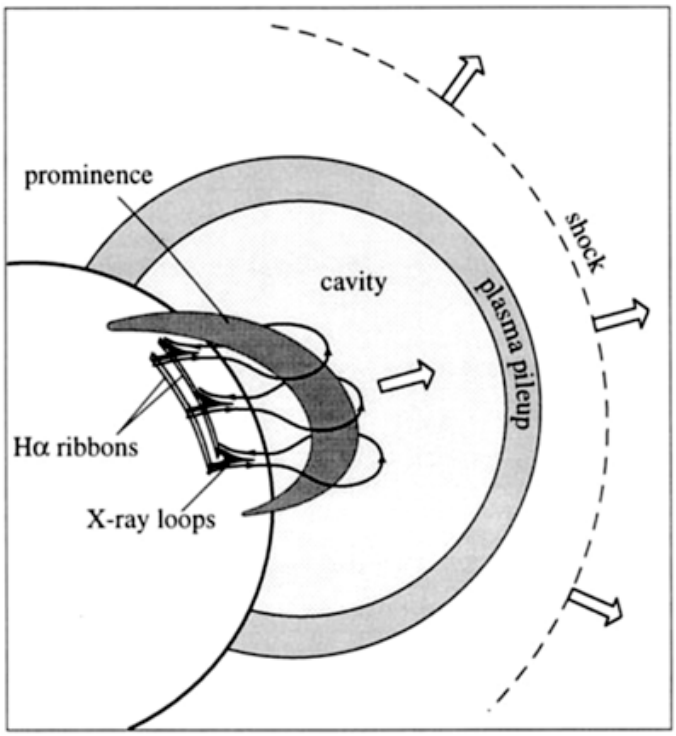

Figure 1.16: Schematics of the CME features (taken from Forbes 2000 [34]).

The generally accepted explanation of CMEs is related to loss of stability of the coronal magnetic field. The energy density released in a large CME is of the order of 100 $erg\ cm^{-3}$. Tables 1.2 and 1.3 show the energy and energy density for different sources in the solar corona. One can see that the magnetic energy is the only source, which can support an eruption.

Table 1.2: Energy Requirements for a Moderately Large CME

Parameter	Value
Kinetic energy (CME, prominence, and shock)	$10^{32}\ ergs$
Heating and radiation	$10^{32}\ ergs$
Work done against gravity	$10^{31}\ ergs$
Volume involved	$10^{30}\ cm^3$
Energy density	$100\ ergs\ cm^{-3}$

Table 1.3: Estimates of Coronal Energy Sources

Form of Energy	Observed Average Values	Energy Density $ergs\ cm^{-3}$
Kinetic $((m_p n V^2)/2)$	$n = 10^9\ cm^{-3}$, $V = 1\ km\ s^{-1}$	10^{-5}
Thermal (nkT)	$T = 10^6\ K$	0.1
Gravitational $((m_p n g h)/2)$	$h = 10^5\ km$	0.5
Magnetic $B^2/8\pi$	$B = 100\ G$	400

Since gravity and pressure gradient forces are negligible in the solar corona, the common way to describe its magnetic field is the force-free approximation (the Lorentz force is zero). In the force-free configuration electric currents can flow only along the field lines. This is the minimum energy state that a non-potential magnetic field can have. Because the photosphere is much denser than the corona, the field lines are considered to be "line-tied", which means that the footpoints of field lines are attached to the photosphere. This approximation assumes that the footpoints photospheric velocity is much smaller than the Alfven speed in the corona (the speed of the magnetic perturbation), hence the magnetic field will reconfigure itself to any change of the footpoint and will remain quasi-static. Most of CME models assume that these photospheric motions, in addition to the emerging of new magnetic flux

from the sub-surface, can shear and twist the coronal magnetic field until it looses its equilibrium and erupts.

The energy scheme of a CME is as follow. Initially, the system is in steady state and free energy begins to build up due to the shear of the field lines. At some critical point, the system looses its stability when the field lines cannot hold the forces that act on them; some of the field lines are opened and material is ejected to space. After the eruption, the system arranges itself to a lower energy state. Therefore, the pre-eruption state, where all the field lines were closed, need to have an higher energy than the post-eruption state where some of the field lines are open (the footpoints location of both states remain unchanged). In 1984, Aly [3] showed that for ideal MHD magnetic configuration with the same inner boundary conditions (the footpoints location), the fully open field line configuration always has higher magnetic energy than the force-free configuration; the ratio of the fully open configuration to the potential field (sun centered dipole) is about 1.66. The paradox is simple. In order to open the field lines we need to put energy into the system, but in order to get the eruption, we need the system to release energy.

The current models for CME initiation are proposed under Aly's limitation, while others try to work out the paradox assuming non-ideal MHD processes such as, magnetic reconnection and the existence of current sheets, or assuming a change in the inner boundary conditions (flux emergence). There are three main types of models for CME initiation [84]: 1) the so-called "flux-rope" models in which the CME is initiated by introducing a flux rope that goes through slow shearing and twisting motions of its footpoint so that the magnetic energy stored in the rope increases until the rope becomes unstable and erupts; 2) the so-called "shear-arcade" models in which the eruption the footpoints in a set of closed magnetic field lines

are sheared and the eruption is obtained by magnetic reconnection of the raising field with an overlaying background field; 3) flux-emergence models in which the eruption is a result of new magnetic flux emerging to the surface and interacting with the surrounding magnetic field and plasma. Figures 1.17 - 1.19 show examples of sheared-arcade, flux-rope, and flux-emergence CME initiation models.

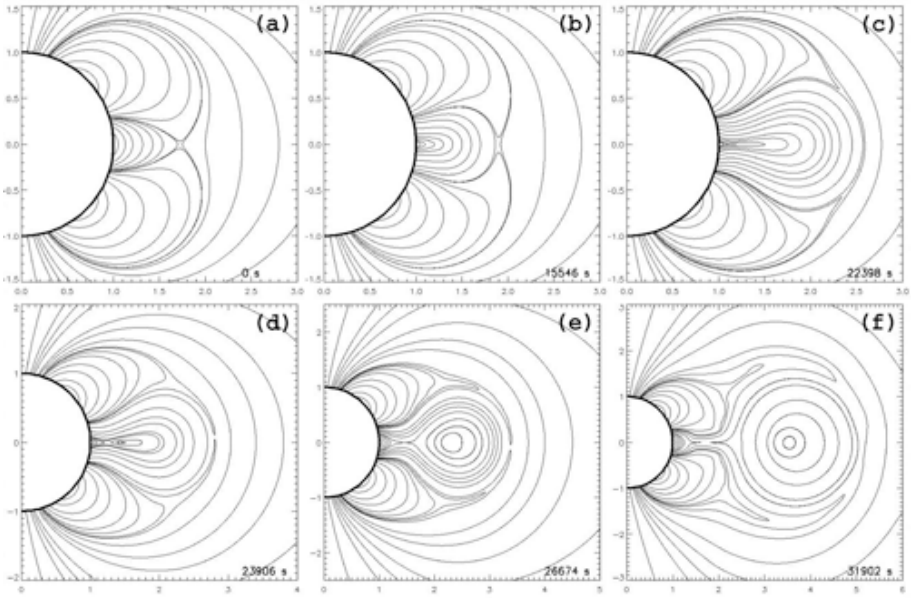

Figure 1.17: An example of a shear-arcade model - the "breakout" model taken from Lynch et. al 2004 [59]. The arcade interacts with the overlaying field.

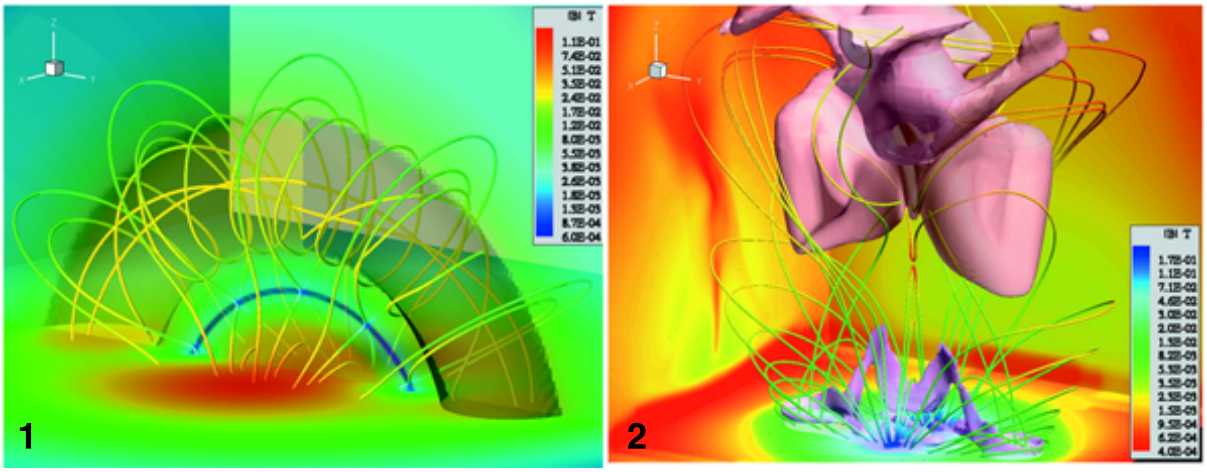

Figure 1.18: An example of a flux-rope model taken from Roussev et. al 2003 [82]. The initial flux rope goes unstable and erupts.

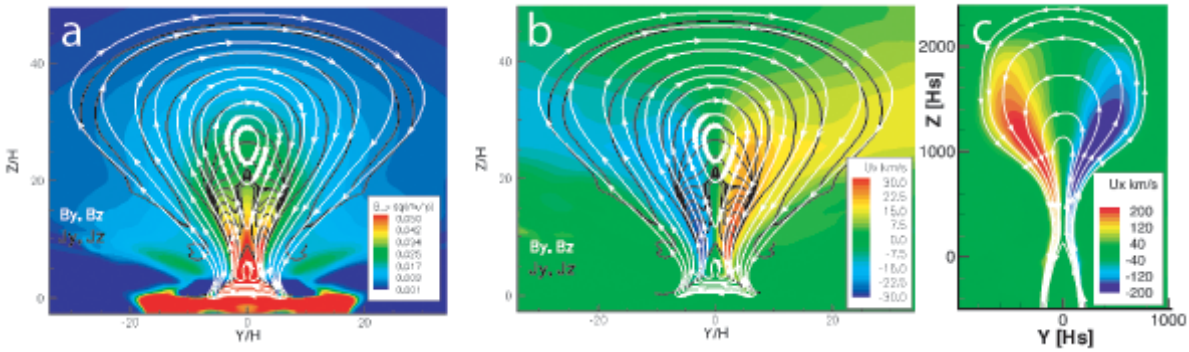

Figure 1.19: Eruption of a three-dimensional emerging magnetic flux rope as a model for CMEs by W. B. Manchester [62]. Panel (a) illustrates the Lorentz force, which drives the shear flows producing the eruption. Here, magnetic stream lines (confined to the $y-z$ plane at the central cross section of the rope) are drawn as white lines while black lines show the direction of the current density. The existence of the Lorentz force ($\mathbf{j} \times \mathbf{B}$) out of the plane is clearly seen where the field and current density are oblique. The magnetic field crosses $\mathbf{j}$ in opposite directions on opposite sides of the rope producing the shear stress. The horizontal cross-field current is the result of the large vertical gradient in the axial magnetic field component shown in color. The horizontal shear velocity, which clearly occurs where $\mathbf{j}$ and $\mathbf{B}$ are non-parallel is shown in Panel (b). Panel (c) shows Lorenz-force-driven shear flows driving an eruption in a magnetic arcade, which also explains CMEs.

1.9 The Heliosphere

The Heliosphere is basically the interplanetary space extending from the Sun to the boundary of the solar system. This boundary is called the Heliopause and it separates the subsonic solar wind from the interstellar medium. There is a termination shock before the heliopause where the solar wind slows down to subsonic speed and there is probably another bow shock on the other side where the interstellar gas becomes subsonic. Figure 1.20 shows the different regions in the heliosphere with the location of the Voyager 1 and 2 spacecrafts.

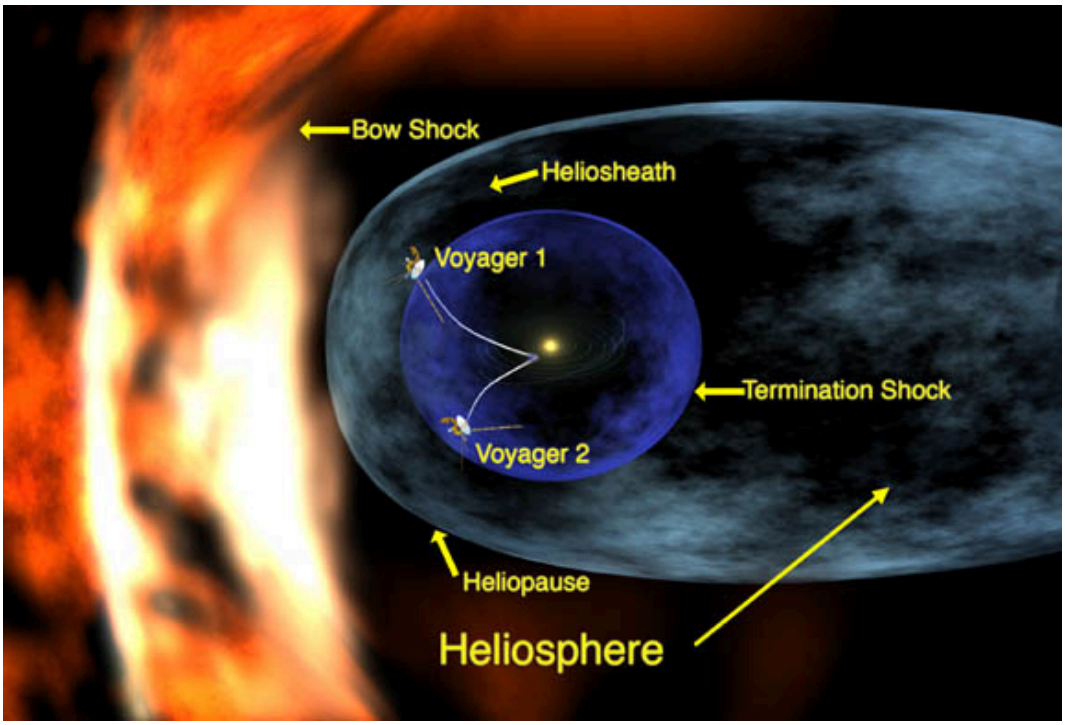

Figure 1.20: The different regions in the heliosphere with the location of the Voyager 1 and 2 spacecrafts (taken from NASA's website).

Since the solar wind is very highly conducting gas, the magnetic field of the Sun is dragged out by the solar wind and opened up into the heliosphere. In the frame rotating with the Sun, charged particles move along magnetic field lines. Therefore, the shape of the helispheric magnetic field determines the dynamics and transport of

solar wind particles, Solar Energetic Particles (SEPs), and cosmic rays (even though the bulk kinetic energy of the solar wind is much greater than its magnetic energy).

1.9.1 The Parker Spiral

Suppose the solar wind plasma flows radially from the Sun. Each plasma parcel drags the magnetic field with it, so the magnetic field should be parallel to the solar wind direction. These paths are also equipotential since $\mathbf{E}' = \mathbf{u}' \times \mathbf{B} = 0$. Let us consider the effect of the solar rotation. In the frame of reference rotating with the Sun, the solar wind velocity is:

$$\begin{aligned} u_r &= \tfrac{dr}{dt} = u_{sw} \\ u_\phi &= r \sin\Theta \tfrac{d\phi}{dt} = -\Omega_\odot r \sin\Theta, \end{aligned} \tag{1.14}$$

where $\Omega_\odot = 2.810^{-6}\ rad\ s^{-1}$ is the solar rotation, and Θ is the heliographic latitude. Solving for r and ϕ we obtain the equation for $\phi(r)$:

$$\phi(r) = \phi_0 - \frac{\Omega_\odot}{u_{sw}}(r - R_s). \tag{1.15}$$

This equation describes an archemidian spiral and is called the *Parker Spiral*. R_s is the radius in which the solar magnetic field lines are assumed to be purely radial. This radius is commonly refers to as the "source surface", and is discussed in detail in Section 2.4.1.

The heliospheric magnetic field configuration is:

$$\mathbf{B} = B_s \left(\frac{R_s}{r}\right)^2 \mathbf{e}_r - B_s \left(\frac{R_s^2}{r}\right) \frac{\Omega_\odot \sin\Theta}{u_{sw}} \mathbf{e}_\phi, \tag{1.16}$$

where B_s is the field strength at the source surface. Since the radial component drops like $1/r^2$, while the azimuthal component drops like $1/r$, the spiral has an angle of about 45° at the Earth orbit and close to 90° at Saturn's and Jupiter's orbits. Figure 1.21 shows the Parker spiral and the magnetic field lines configuration for different heliolatitudes.

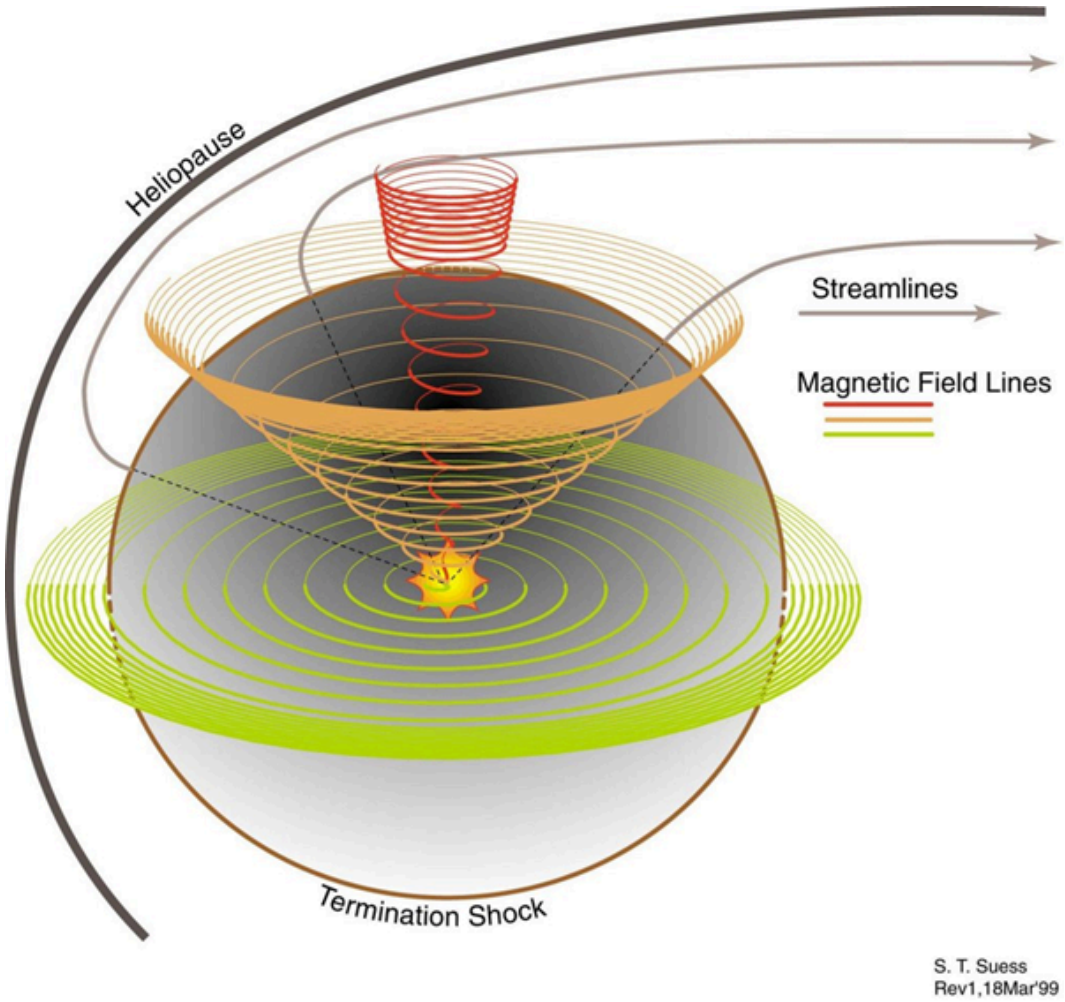

Figure 1.21: The Parker spiral, streamlines, and magnetic field lines configuration for different heliolatitudes. (taken from NASA's website).

1.9.2 Deviations from the Parker Spiral

The general dynamics in the heliosphere is controlled by the Parker spiral. However, in-situ measurements observed deviations from the predicted behavior of plasma. In order to explain these deviations, new theories were born where some of them, for example particle diffusion, became a completely new fields in space physics. In this section we will mention the main ideas about deviations from the Parker spiral without getting into details on each subject.

- **Superthermal Particle diffusion**

  Charged particles gyrate around magnetic field lines with guiding center that moves along the field lines. Therefore, the transport of charged particles is generally prefferred along magnetic field lines. In order to explain the observed particle distributions however, a transverse particle motion must be taken into account. The main mechanism in which particles move across field lines in the heliosphere is through a diffusion processes. The physical mechanism of particle diffusion in heliosphere is as follow. Even though the large-scale magnetic field follows the Parker spiral its small-scale is quite turbulent with local irregularities. These small deviations in the magnetic field introduce small-scale pitch angles that cause particles to move across the large-scale field line.

- **Pickup ions**

  So far, we discussed the motion of superthermal charged particles in the heliosphere. However, the interstellar medium contains neutral gas and dust, in particular near planets, moons comets and asteroids. These nuetrals are often heavier than hydrogen. If some neutral particle becomes ionized due to solar radiation or charge-exchange process, it starts to gyrate around the magnetic

field line. The field line moves with the solar wind plasma with speed of u_{sw}, so eventually, the guiding center of the new ion (or pick-up ion) is accelerated to speed of the order of u_{sw}. In addition, the random velocity of the pickup ions is also close to u_{sw}. This mass loading process slows down the solar wind in the heliosphere.

- **Solar differential rotation**

  When the Ulysses spacecraft measured energetic particles at high heliolatitudes for the first time, it observed particles that were thought to exist only at low latitudes. The temporal evolution of these particles has a clear periodicity of about 27 days, which is about the same as the solar rotation period. In 1996, Fisk [29] proposed an explanation for this observation as follow. Since the Sun rotates differentially, while the top of the corona seems to rotate rigidly, there will be excursion of the field lines due to the motion of the magnetic field footpoints on the photosphere and due to the mis-alignment of the rotation axis with the magnetic axis. This will lead to migration of field lines from one latitude to another and can explain how particles originating on a low latitude filed line can appear in higher latitudes. The left part of Figure 1.22 shows a schematics of the Fisk model. Ω marks the rotation axis of the Sun, M marks the magnetic axis and P marks the magnetic field line originated from the solar pole. One can see that at the top of the corona (the external surface), this field line appears in different latitude. The difference in the heliospheric spiral is shown in the middle and the right parts.

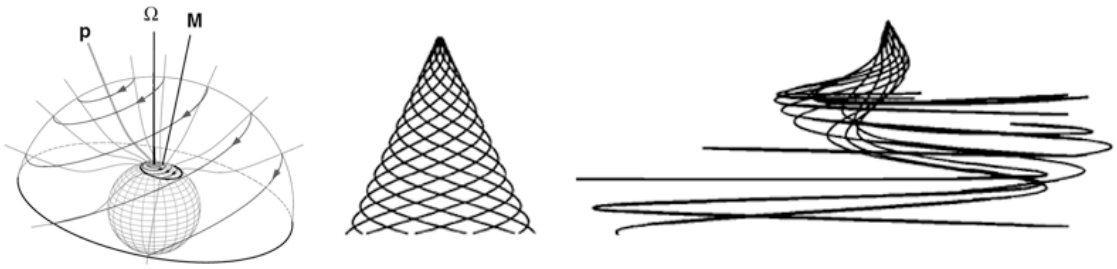

Figure 1.22: A schematics of the Fisk model (left). Ω marks the rotation axis of the Sun, M marks the magnetic axis and P marks the magnetic field line originated from the solar pole. The middle figure shows the unperturbed Parker spiral, and the right figure shows the modified spiral due to differential rotation.

1.10 The purpose of this work

Numerical tools provide an alternative to analytical solutions of physical problems, which are described in mathematical form. Most of the physical systems we deal with and we try to understand are so complicated and non-linear, that it is impossible to derive an analytical solution, unless large number of assumptions and simplifications are made. Numerical simulations, particularly with the current and future computational power, provide us with the opportunity to solve the physical problem with much less simplifications and sometime even allow us to solve the complete problem. Of course, numerical models have their own issues, which will be discussed in Chapter II. In this work, I use numerical simulations to study the physics of the solar corona, the heliosphere, and CMEs. The physical system of the solar corona and the heliosphere is not only non-linear, but it introduces a huge range of both temporal and spatial scales. This range of scales made it impossible to resolve some of the physics even with very sophisticated numerical models. I present some of the first numerical simulations performed using the concept of numerical framework, a concept in which different models for different physical domains are coupled together. This cutting-edge technology represents the next generation of

numerical modeling.

This work is divided to three major parts:

In Chapter II, I present a global, three-dimensional model for the solar corona and the inner heliosphere (up to 1 AU) in order to study the evolution of the large-scale quite Sun. This part is important in order to learn about the long-term evolution of the solar magnetic field, the magnetic connectivity between the Sun and the Earth, the ambient solar wind conditions at the vicinity of the Earth, and the global structure of the heliospheric magnetic field. This model can be later used to study long-term dynamics in the corona and heliosphere such as the effect of differential rotation on the structure of the heliospheric magnetic field, or the three dimensional evolution of the heliospheric magnetic field through the solar cycle.

In Chapter III, I investigate the effect of magnetic reconnection on the transport of the open magnetic flux of the Sun. Since the open flux of the Sun is the magnetic field component, which connects the Sun with the Earth, it is important to predict its evolution in time. I present a numerical model for the transport of the open flux, which includes components of new theoretical models. I show that the solution is different if this effect is taken into account.

In Chapter IV, I perform a Sun-to-Earth simulation of a CME event. I study the CME propagation in the interplanetary space and the importance of the ambient solution on the propagation. In addition, this simulation is important to demonstrate the opperationality of the numerical model for the purpose of space weather prediction. This kind of simulations are the essence of any numerical, dynamic, and physics based space weather forecasting tools.

In Chapter V, I describe the planned future work and some open issues.

CHAPTER II

A Global MHD Model for the Solar Corona

"We consider the dynamical consequences of Biermann's suggestion that gas is often streaming outward in all directions from the Sun with velocities of the order of $500-1500$ *km/sec. These velocities of* 500 *km/sec and more and the interplanetary densities of* 500 *ions/cm*$^{-3}$ *(*10^{14} *gm/sec mass loss from the Sun) follow from the hydrodynamic equations for* 3×10^6 *K solar corona. It is suggested that the outward-streaming gas draws out the lines of force of the solar magnetic fields so that near the Sun the field is very nearly in a radial direction. Plasma instabilities are expected to result in the thick shell of disordered field (*10^{-5} *gauss) inclosing the inner solar system, whose presence has already been inferred from cosmic-ray observations."*

E. N. Parker, Astrophysical Journal, 1958.

2.1 The Ambient Solar Wind

The ability to predict the physical conditions in the interplanetary space, as well as at the vicinity of the Earth on a daily basis has become significantly important in the past few decades. The growing dependency on satellite communication, the planned space missions, and the hazards to systems on the ground brought the concept of Space Weather. Unlike atmospheric forecasting tools, which have been

in use for decades, the tools for space weather forecasting are yet very limited. The prediction of space weather depends mostly on satellites, which observe the activity on the Sun (such as SOHO and STEREO) or satellites, which can measure the solar wind conditions at the vicinity of the Earth (such as ACE and WIND). Since the forecasting time of these near Earth satellites is about 60 minutes [36], we need to develop dynamical numerical models for the space environment in order to improve the forecasting time.

The Space Weather Modeling Framework (SWMF) is a computational tool for simulating the space environment from the solar photosphere all the way to the Earth's upper atmosphere. The complete description of the SWMF can be found in [99]. The SWMF includes the numerical models for the Solar Corona (SC) and the Inner Heliosphere (IH), which describe the interplanetary space between the Sun and the Earth. The SC and IH components are being used to describe the physical conditions of the ambient solar wind and the dynamical conditions during a space weather event [21].

In this chapter, I focus on modeling the ambient conditions for the SC and IH using the technolgy of the SWMF for the first time. Since the most important parameter in space weather forecasting is the arrival time of the Interplanetary Shock (IS) of a Coronal Mass Ejection (CME), it is important to obtain the correct background conditions in which this shock propagates through.

2.1.1 Previous numerical simulations of the solar corona and heliosphere

Previous work has been done to model the SC and IH using global MHD models, which can be divided according to their solar wind heating mechanisms. The most straightforward method is to predefine the volumetric heating in an empirical manner. As an example for this category of heating mechanism I mention the MAS code

for the solar corona developed at SAIC by (Mikic, Linker, Riley, Lionello, and Titov [67, 55, 56, 81]), the ENLIL code for the helisphere developed by Odstrcil and Pizzo ([69, 70]), Suess et al. ([95]), and the early BATS-R-US solar corona modeling by Groth ([42]).

A more physics-based method to obtain a solar wind solution is to use the WKB approximation of the Alfvén wave turbulence to obtain the extra energy required to heat and accelerate the solar wind. The main model uses this approach has been developed by Usmanov et al. ([102, 101]).

An alternative method is to assume that the extra energy gained by the solar wind can be represented as a change in the polytropic index, γ. The acceleration of the solar wind, as well as the difference in the final speed of the fast and slow solar wind is obtained by using a non-uniform distribution of γ in the energy equation. The first model to use this approach has been developed by Wu et al. ([114]). Roussev et al. ([83]) presented a new model for the solar corona based on the BATS-R-US global MHD code, in which the the non-uniform distribution of γ was related to the distribution of the magnetic field in the corona.

2.1.2 Scientific contribution of this work

In this work, I present a new numerical model for the solar corona and heliosphere (Cohen et al. [19]) based on the model by Roussev et al. which adpots the non-uniform γ as well. However, in order to obtain a more realistic solution, I specify the distribution of γ using an empirical model for the solar wind. This way the model is constrained by the observed solar wind at 1 AU and it should provide better results at 1 AU. Since the solar wind heating and acceleration in the model are constrained by an empirical input, it should also provide the correct solution for the solar corona.

In order to validate a global model, one needs to compare its output thoroughly

with observations. For the particular purpose of space weather forecasting, the model should match the observations of the spacecrafts, which measure the solar wind conditions at the vicinity of the Earth. Here I present a long-term validation of our steady-state SC and IH model. I compare the model's result with ACE and WIND observations for the hydrodynamical parameters, as well as for the magnetic field. This validation is crucial in order to decide whether the model can be used as an operational space weather forecasting system.

2.2 The BATS-R-US Code

The BATS-R-US code has been developed as a general, global tool to simulate plasma phenomena in space. In particular, the model has been developed to deal with the wide variety of temporal and spatial scales in space physics and has Adaptive Mesh Refinement (AMR) capabilities. The code solves the set of ideal Magneto-HydroDynamic (MHD) equations using modern, high-order finite volume upwind schemes based on the Riemann Problem (RP). The RP defines discontinuous initial condition, for example, in two neighboring grid cells. The information between the two states propagates at certain characteristic speeds associated with characteristic waves (CWs), which depend on the physical properties of the system. Mathematically, the CWs are the possible solutions for the set of equations describing the system. In MHD, there are 8 equations with 7 CWs. This degeneracy is a result of the requirement that $\nabla \cdot \mathbf{B} = 0$ and this issue will be discussed in details in section 2.2.5. This section describes the BATS-R-US code in detail.

2.2.1 Physical basis for BATS-R-US

This hyperbolic, conservative set of eq. 1.1 can be written in a matrix form [80]:

$$\frac{\partial \mathbf{U}}{\partial t} = (\nabla \cdot \mathbf{F})^T = \mathbf{S}, \tag{2.1}$$

where in the case of eq. 1.1, $\mathbf{S} = 0$. The set of primitive variables is

$$\mathbf{W} = (\rho, u_x, u_y, u_z, B_x, B_y, B_z, p)^T, \tag{2.2}$$

and the conserved variables are

$$\mathbf{U} = (\rho, \rho u_x, \rho u_y, \rho u_z, B_x, B_y, B_z, E)^T, \tag{2.3}$$

with

$$\mathbf{F} = \begin{pmatrix} \rho\mathbf{u} \\ \rho\mathbf{u}\mathbf{u} + pI + \frac{B^2}{2\mu_0}I - \frac{\mathbf{B}\mathbf{B}}{\mu_0} \\ \mathbf{u}\mathbf{B} - \mathbf{B}\mathbf{u} \\ \left(E + p + \frac{\mathbf{B}\cdot\mathbf{B}}{2\mu_0}\right)\mathbf{u} - \frac{1}{\mu_0}(\mathbf{B}\cdot\mathbf{u})\mathbf{B} \end{pmatrix}^T . \tag{2.4}$$

The electric field can be obtained through the relation $\mathbf{E} = -\mathbf{u} \times \mathbf{B}$.

2.2.2 Numerical solution

The general explicit, upwind finite-volume numerical scheme can be written as:

$$\frac{d\mathbf{U}_i}{dt}V_i + \sum_{faces} \mathbf{F}\cdot\hat{\mathbf{n}}\, dS = \mathbf{S}_i V_i, \tag{2.5}$$

where $\mathbf{U}_i$ and $\mathbf{S}_i$ are the cell-averaged conserved variables and source terms, respectively, V_i is the cell volume, and $\mathbf{F}$ is the flux passing through the cell face in the normal direction, $\hat{\mathbf{n}}$ (see Figure 2.1).

The numerical flux can be obtained using the eigenvalues of the MHD system, λ_k, and the left and right corresponding eigenvectors, l_k, and r_k, respectively. These parameters correspond to the CWs of the system, which are the entropy wave, three magnetic-flux waves, a pair of Alfvén waves, fast magnetosonic wave, and slow magnetosonic wave. The numerical flux is:

$$\mathbf{F}\cdot\hat{\mathbf{n}}(U_L, U_R) = \frac{1}{2}\left(\mathbf{F}\cdot\hat{\mathbf{n}}(U_L) + \mathbf{F}\cdot\hat{\mathbf{n}}(U_R)\right) - \sum_{k=1}^{8} \mathbf{L}_k(U_R - U_L)|\lambda_k|\mathbf{R}_k, \tag{2.6}$$

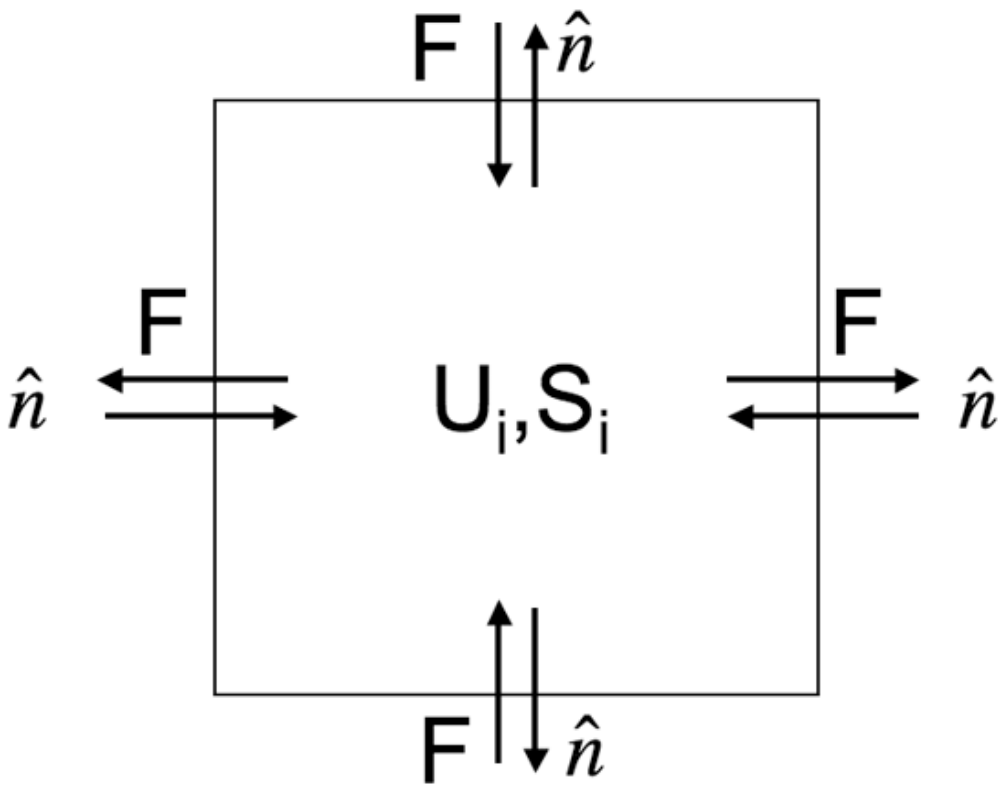

Figure 2.1: The normal fluxes, **F** flowing through the faces of the cells.

with

$$\mathbf{L}_k = l_k \frac{\partial \mathbf{W}}{\partial \mathbf{U}} \tag{2.7}$$

$$\mathbf{R}_k = \frac{\partial \mathbf{U}}{\partial \mathbf{W}} r_k. \tag{2.8}$$

2.2.3 Numerical limiters

Modern higher-order, finite volume schemes use the concept of *Total Variation Diminishing* (TVD) to maintain the scheme monotonicity and to prevent the appearance of a new local extrema in the numerical solution, U. With the spatial index, i, and the temporal index, n, the TV is defined as:

$$TV = \sum_i |U_i - U_{i-1}|, \tag{2.9}$$

with the TVD requirement that

$$TV(U^{n+1}) \leq TV(U^n). \tag{2.10}$$

The manning of eq. 2.10 is that the gradients in the numerical linear reconstruction must be limited, since gradient overshooting will lead to the appearance of oscillations in the numerical solution. In BATS-R-US , the user can choose between number of numerical limiters such as, "minmod", "superbee", and "mc" beta limiter. The different limiters differ from each other by their robustness and accuracy.

In the case of adaptive Cartesian grids, such as in BATS-R-US , a more careful limiting treatment is needed [93]. For a refinement interface such as in Figure 2.2, eq. 2.9 becomes:

$$TV = \sum_{i=1}^{r} S|U_{i-1} - U_i| + \sum_f S_f \left[|U_r - U_{r+1,f}| + \sum_{i=r+2}^{I+1} |U_{i-1,f} - U_{i,f}| \right], \tag{2.11}$$

where S is the face area of the cell. The finer cells are enumerated with the index $i, r+1 \leq i \leq I$ in the longitudinal direction and with the index f in the transversal direction.

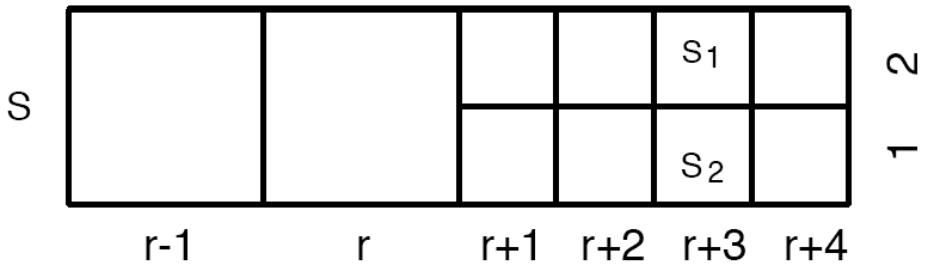

Figure 2.2: Cell enumeration around the refinement interface [93].

2.2.4 The local time stepping algorithm and its convergence rate

In order to speed up the simulation time, one can choose to use a "local time stepping" for steady-state numerical simulations. The local time stepping is the case

in which the time step is calculated individually for each cell. The absolute number of iterations, n, is not very meaningful by itself. To derive a relevant convergence parameter, R, for a particular grid, consider first the time accurate explicit scheme. In this case, the rate of the numerical solution converges to a steady state is inversely proportional to the characteristic time:

$$t_c = \int_{R=1}^{R_{OB}} \frac{\Delta x}{C(x)}, \tag{2.12}$$

during which the physical perturbations propagate from say, the inner boundary to the outer boundary (OB), with C being the characteristic speed. Therefore, the proper convergence parameter is the ratio of the simulation time to the characteristic time:

$$R = \frac{n\Delta t}{t_c} = \frac{n}{\sum_n \frac{1}{CFL(n)}}, \tag{2.13}$$

where I represent the integral along the straight line as a sum by the cells it intersects, with the local Courant-Friedrichs-Levy number $CFL(n) = \frac{C\Delta t}{\Delta x}$.

For a stability of the explicit scheme, I use $CFL \leq 0.8$. The values of the inverse to the CFL number in eq. 2.13 are close to unity only in the smallest cells near the Sun, where the speed C has its maximum value ($\frac{C_{max}\Delta t}{(\Delta x)_{min}} \approx 0.8$). To the contrary, at larger heliocentric distances, the inverse of the CFL number may be 2-3 orders of magnitude larger $\left(\frac{\Delta x}{\Delta x_{min}}\right)\left(\frac{C_{max}}{C(x)}\right) \gg 1$, drastically degrading the convergence.

That is why I use the local time stepping algorithm in simulating a steady state solution, which automatically maintains the local CFL number to be equal to 0.8

everywhere, with the choice of a local time step,

$$\Delta t(x) = 0.8\frac{\Delta x}{C(x)}. \tag{2.14}$$

In this case the convergence parameter becomes:

$$R = \frac{0.8n}{N_x}, \tag{2.15}$$

where N_x is the typical number of cells (of any grid) intersect with the line as described above.

2.2.5 $\nabla \cdot \mathbf{B}$ control in BATS-R-US

In order to follow Maxwell's equations in the MHD numerical solution, we need to maintain the non-hyperbolic constrain of $\nabla \cdot \mathbf{B} = 0$ within the machine roundoff error. However, by simply setting the divergence of the magnetic field to be zero, we change the character of the equations, since the eight MHD conservation laws are not fully independent. Powell [80] demonstrated that by following the MHD equations and by keeping the terms proportional to $\nabla \cdot \mathbf{B}$ and rearranging the equations, we can obtain a set of source terms that are proportional to $\nabla \cdot \mathbf{B}$ in a way that these sources will be advected out of the system as long as the initial and boundary conditions satisfy $\nabla \cdot \mathbf{B} = 0$. This source term is:

$$\mathbf{S} = -\nabla \cdot \mathbf{B} \begin{pmatrix} 0 \\ \mathbf{B} \\ \mathbf{u} \\ \mathbf{u} \cdot \mathbf{B} \end{pmatrix} \tag{2.16}$$

In this case, eq. 2.5 becomes:

$$\frac{d\mathbf{U}_i}{dt}V_i + \sum_{faces} \mathbf{F}\cdot\hat{\mathbf{n}}\, dS = \mathbf{S} = -\begin{pmatrix} 0 \\ \mathbf{B} \\ \mathbf{u} \\ \mathbf{u}\cdot\mathbf{B} \end{pmatrix} \sum_{faces} \mathbf{B}\cdot\hat{\mathbf{n}}\, dS. \tag{2.17}$$

This method of controlling $\nabla \cdot \mathbf{B}$ is called the *eight wave* method and it is the default method in BATS-R-US . Other methods to limit $\nabla\cdot\mathbf{B}$ such as, the projection scheme, constrained transport, and $\nabla\cdot\mathbf{B}$ diffusion [98] are also implemented in BATS-R-US .

2.2.6 Grid structure

The grid used in BATS-R-US is adaptive with blocks of arbitrary size. Each block corresponds to a node of the tree structure and can be devided into eight 'children' blocks if a grid refinement is necessary. Removing refinement from a block can be done in the same way. Each block also holds the information of all the 'ghost-cells' needed for the computation. Figure 2.3 shows the grid cells of a refined block next to an un-refined block (red), together with the ghost-cells around them (green).

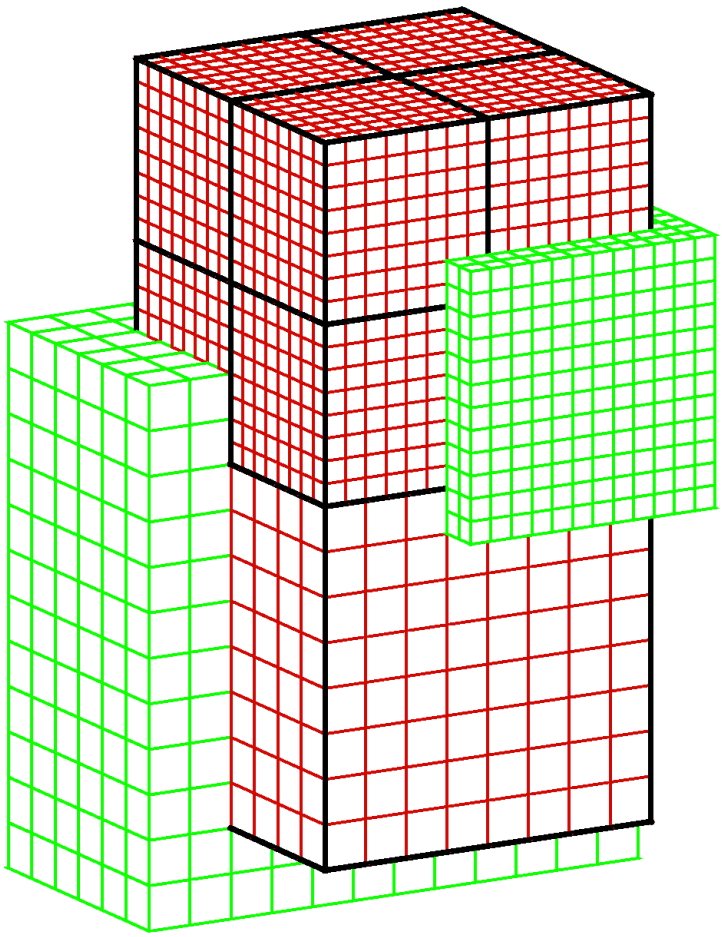

Figure 2.3: The block structure of BATS-R-US . Large cell blocks require the same amount of computation as small cell blocks. Each block is provided with the required set of ghost-cells (green).

The tree structure of BATS-R-US is very convenient for two reasons. First, the block distribution among the nodes makes the code parallelization very easy, since each 'parent' block holds the information needed by all the children blocks. In addition, the number of cells in the refined and un-refined block is the same so that load balancing can be easily achieved. Figure 2.4 shows the tree structure of BATS-R-US .

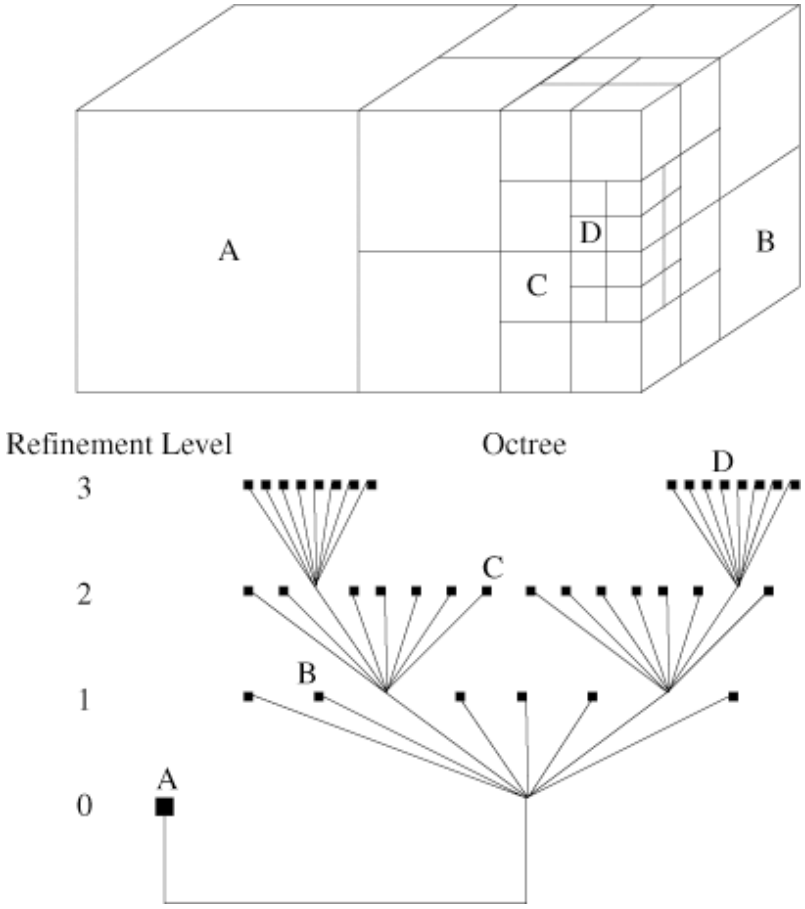

Figure 2.4: Schematics of the parallel architecture of BATS-R-US . Each parent block has the information from all its children blocks.

The AMR criteria in BATS-R-US can be geometric, as well as physics based. The geometrical AMR is usually done when a refinement around a particular region is needed. Examples for geometric AMR are refinement around an object or along a predicted CME trajectory. Geometrical based AMR is usually known in advance and is done at the beginning of the simulation. Alternatively, a more dynamical AMR is the physics based one. This AMR is done when a particular area, usually one with sharp gradients (or shocks), can not be captured by the original resolution. An examples for physics based AMR criteria are:

$$\begin{aligned} &|\nabla \cdot \mathbf{u}|\sqrt{V} \\ &|\nabla \times \mathbf{u}|\sqrt{V} \\ &|\nabla \times \mathbf{B}|\sqrt{V} \end{aligned} \tag{2.18}$$

One use of physics based AMR is the tracking of a CME shock as it propagates in space. Another commonly used physics based AMR situations is AMR around the Earth's magnetopause, or around the heliospheric current sheet, which are less dynamic than CMEs but the criteria for refinement is still physical. Figure 2.5 shows the grid structure of a simulation of the Earth's magnetosphere as it changes due to AMR.

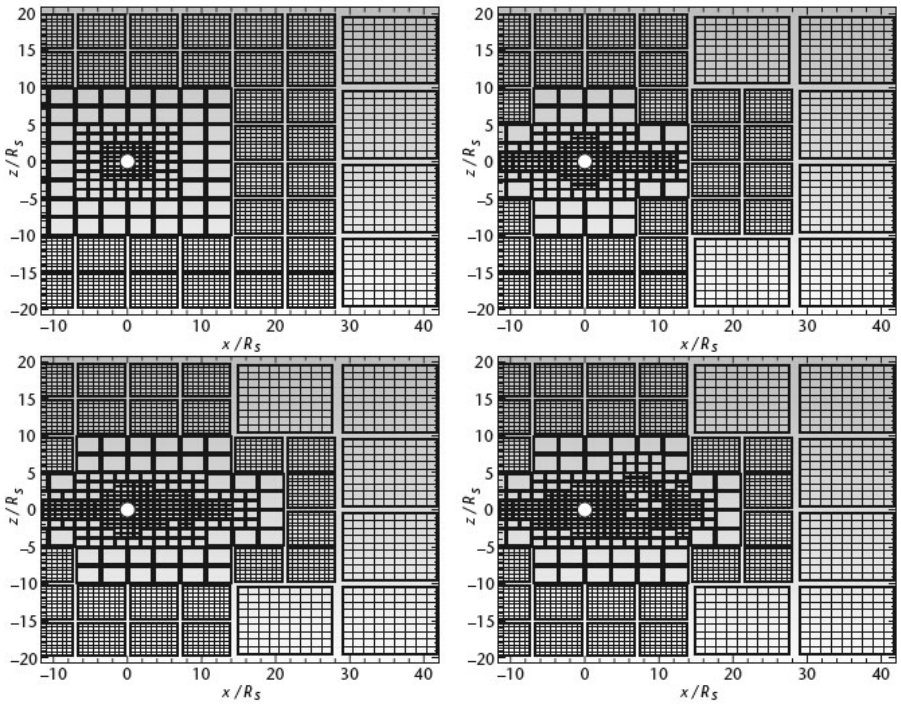

Figure 2.5: An example of of the AMR throughout a simulation of the Earth's magnetosphere from the initial grid state (top-left) to the final grid state (bottom-right).

2.3 The Space Weather Modeling Framework

In order to perform numerical simulations of large and complex systems in more details and higher resolution, one should adopt the concept of numerical framework. The basic idea behind this concept is that the whole domain should be split into separate sub-domains, where separate numerical models are applied to each one of the domains. Each model can have its own grid structure and its own physical characteristics, and the models are coupled through a common interface. The space environment is a great example of how the use of a framework can significantly increase our capabilities due to it's wide range of spatial and temporal scales.

The SWMF has been developed at the Center for Space Environment Modeling (CSEM) and it contains separate modules for simulating the space environment from the surface of the Sun to upper atmospheres of the Earth and other planets. The physical domains are:

1. Solar Corona (SC), BATS-R-US based.
2. Inner Heliosphere (IH), BATS-R-US based.
3. Global Magnetosphere (GM), BATS-R-US based.
4. Upper Atmosphere (UA), Global Ionosphere Thermosphere Model (GITM).
5. Inner Magnetosphere (IM).
6. Solar Energetic Particles (SP), based on U. of Arizona particle transport code.
7. Radiation Belt (RB).
8. Polar Wind (PW).
9. Ionosphere Electrodynamics (IE).

The framework architecture is designed in a way so the run is done using a single executable. The coupling is done through a standard interface coupler, which ensures that each model receive the needed information in the correct units, frame of reference etc. In addition, SWMF contains a large set of utilities that can be used by each of the modules, such as, parallelized algorithms for field line tracing, interpolations, transformation between space physics coordinate systems, and more. The SWMF architecture is designed in a way that the code will run in an efficient matter. Figure 2.6 shows the general structure of the SWMF, the different domains and the coupling between them.

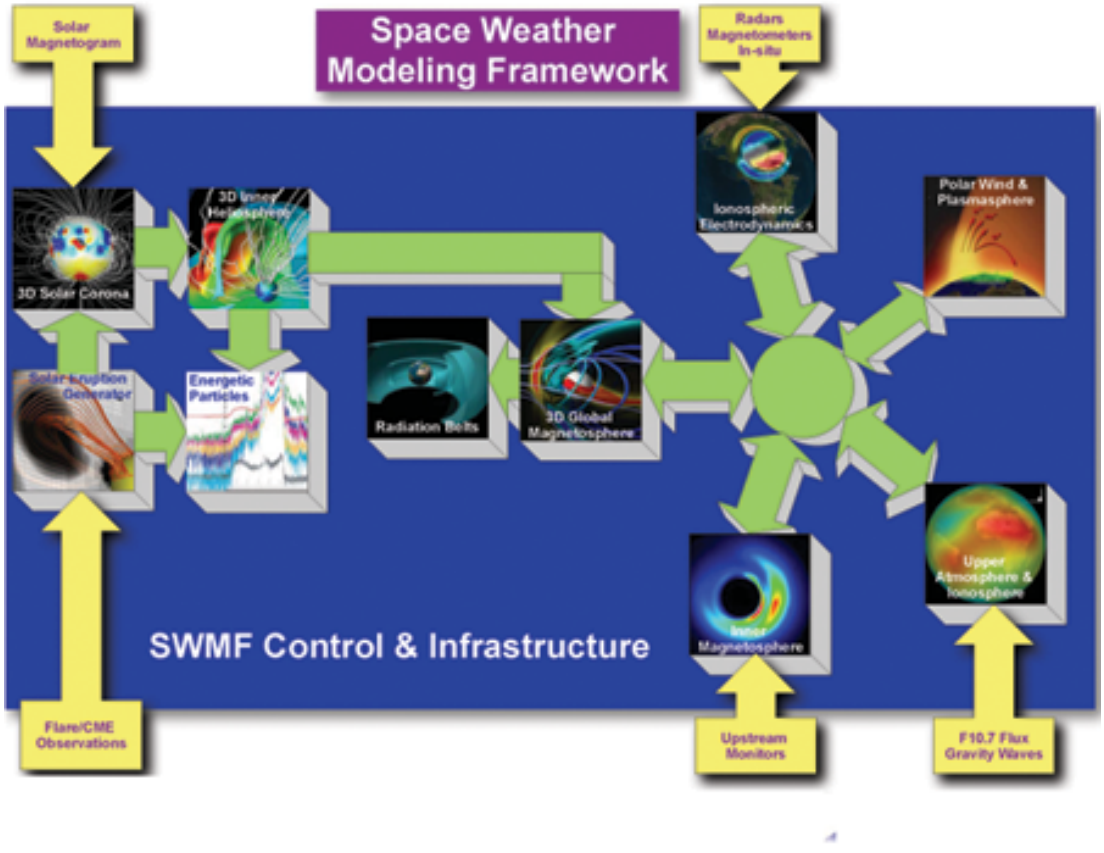

Figure 2.6: Module structure and coupling architecture of the SWMF.

2.4 Numerical Model for the Solar Corona and Heliosphere

2.4.1 The potential field approximation

The solar corona is dominated by its magnetic field. Therefore, it is important to know what is the three dimensional structure of the magnetic field in order to study the physical processes in the corona. Since the solar magnetic field can be routinely measured only at the photosphere, where the plasma density is high enough for measuring the Zeeman Splitting, one needs to find a way to approximate the global structure of the coronal magnetic field. The most commonly used method to approximate the coronal magnetic field is the so-called 'potential field' approximation [2]. In this approximation, it is assumed that the Alfvén speed is much larger than the speed of convective motions in the low corona, so the field line relaxation time is much shorter than the typical advection time scale. In other words, the field line will respond quickly to any motion we apply on it (this motion can be seen as electric current) so in practice the magnetic field is static. Under the assumption that there are no currents in a physical system, we can write Ampere's law as follows:

$$\nabla \times \mathbf{B} = 0, \tag{2.19}$$

and we can write $\mathbf{B}$ as a gradient of some scalar potential ψ:

$$\mathbf{B} = -\nabla\psi. \tag{2.20}$$

Since we also know that

$$\nabla \cdot \mathbf{B} = 0, \tag{2.21}$$

combining eq. 2.20 with eq. 2.21 results in the Laplace equation for the scalar potential:

$$\nabla^2\psi = 0. \tag{2.22}$$

The general solution for this equation in spherical coordinates for $R_0 < r < R_s$ is:

$$\psi(r,\theta,\phi) = \sum_{n=1}^{\infty}\sum_{m=0}^{n}\left[R_0\left(\frac{R_0}{r}\right)^{n+1} + R_s \cdot c_n\left(\frac{r}{R_s}\right)^{n}\right] \times \left(g_n^m \cos m\phi + h_n^m \sin m\phi\right) P_{nm}(\theta), \tag{2.23}$$

which gives $\psi = 0$ at $r = R_s$ for the choice of $c_n = -\left(\frac{R_0}{R_s}\right)^{n+2}$, particularly as $R_s \to \infty$. P_{nm} are the associated Legendre Polynomials, which are a function of $\cos\theta$. The coefficients g_n^m and h_n^m can be determined from the photospheric magnetic field data and have magnetic field dimension.

Following the above solution, we can obtain the solution for the magnetic field components (Altschuler et al. 1969, eqs. 8-10):

$$B_r = -\frac{\partial\psi}{\partial r} = \sum_{n=1}^{\infty}\sum_{m=0}^{n}\left[(n+1)\left(\frac{R_0}{r}\right)^{n+2} - n\left(\frac{r}{R_s}\right)^{n-1} c_n\right] \times \left(g_n^m \cos m\phi + h_n^m \sin m\phi\right) P_n^m(\theta), \tag{2.24}$$

$$B_\theta = -\frac{1}{r}\frac{\partial\psi}{\partial\theta} = -\sum_{n=1}^{\infty}\sum_{m=0}^{n}\left[\left(\frac{R_0}{r}\right)^{n+2} + c_n\left(\frac{r}{R_s}\right)^{n-1}\right] \times \left(g_n^m \cos m\phi + h_n^m \sin m\phi\right)\frac{\partial P_n^m(\theta)}{\partial\theta}, \tag{2.25}$$

$$B_\phi = -\frac{1}{r\sin\theta}\frac{\partial\psi}{\partial\phi} = \sum_{n=1}^{\infty}\sum_{m=0}^{n}\left[\left(\frac{R_0}{r}\right)^{n+2} + c_n\left(\frac{r}{R_s}\right)^{n-1}\right] \times \frac{m}{\sin\theta}\left(g_n^m \sin m\phi - h_n^m \cos m\phi\right) P_n^m(\theta). \tag{2.26}$$

We can determine the harmonic coefficients from the observed photospheric values of B_r as follows. The orthogonality relation over a sphere with $r = 1$ for the general

Legendre functions is:

$$\frac{1}{4\pi}\int_{\theta=0}^{\pi}\int_{\phi=0}^{2\pi} P_{nm}(\theta)\left\{\begin{array}{c}\cos m\phi\\ \sin m\phi\end{array}\right\} P_{n'm'}(\theta)\left\{\begin{array}{c}\cos m'\phi\\ \sin m'\phi\end{array}\right\}\sin\theta d\theta d\phi = W\delta_{nn'}\delta_{mm'}, \tag{2.27}$$

where W is the normalization factor. For the general Legendre functions,

$$W = \frac{2}{2n+1}\frac{(n+m)!}{(n-m)!}, \tag{2.28}$$

and

$$W = \frac{1}{2n+1} \tag{2.29}$$

for the Schmidt normalization, so the relation between the Schmidt (P_n^m) and the general Legendre functions (P_{nm}) is:

$$P_n^m(\theta) = \left\{2\frac{(n-m)!}{(n+m)!}\right\}^{1/2} P_{nm}(\theta). \tag{2.30}$$

In BATS-R-US , the polynomials are calculated with the Schmidt normalization. For $r = R_0 = 1$, the radial magnetic field becomes:

$$B_r(\theta,\phi) = \sum_{n=1}^{\infty}\sum_{m=0}^{n} R_n\left\{\begin{array}{c}g_n^m\\ h_n^m\end{array}\right\} P_n^m(\theta)\left\{\begin{array}{c}\cos m\phi\\ \sin m\phi\end{array}\right\}, \tag{2.31}$$

where $R_n = \left[(n+1) + n\left(\frac{1}{R_s}\right)^{2n+1}\right]$.

Following eq. 2.27, we can obtain the harmonic coefficients from the photospheric magnetic data, assuming the Schmidt normalization of the Legendre functions (Altschuler et al. 1969):

$$\left\{\begin{array}{c}g_n^m\\ h_n^m\end{array}\right\} = \frac{2n+1}{4\pi R_n}\int_{\theta=0}^{\pi}\int_{\phi=0}^{2\pi} B_r(r=R_\odot,\theta,\phi)P_n^m(\theta)\left\{\begin{array}{c}\cos m\phi\\ \sin m\phi\end{array}\right\}\sin\theta d\theta d\phi, \tag{2.32}$$

where

$$B_r = \begin{cases} B_{magnetogram} & \text{for radial magnetogram,} \\ \frac{B_{magnetogram}}{\sin\theta} & \text{for Line-of-Sight magnetogram.} \end{cases}$$

The discretized version of eq. 14 is (Altschuler et al. 1969, eq. 15):

$$\begin{Bmatrix} g_n^m \\ h_n^m \end{Bmatrix} = \frac{1}{A}\frac{2n+1}{R_n} \sum_{i=0}^{N_\theta - 1} \sum_{j=0}^{N_\phi - 1} B_r(i,j) \cdot da_{i,j} \cdot P_n^m(\theta_i) \begin{Bmatrix} \cos m\phi_j \\ \sin m\phi_j, \end{Bmatrix} \tag{2.33}$$

where $da_{i,j} = \sin\theta_i d\theta d\phi$ and $A = \sum_{i=0}^{N_\theta - 1} \sum_{j=0}^{N_\phi - 1} da_{i,j} = 4\pi$ for $r = R_\odot$.

Figure 2.7 shows examples of the three-dimensional structure of the coronal magnetic field computed using the potential field approximation.

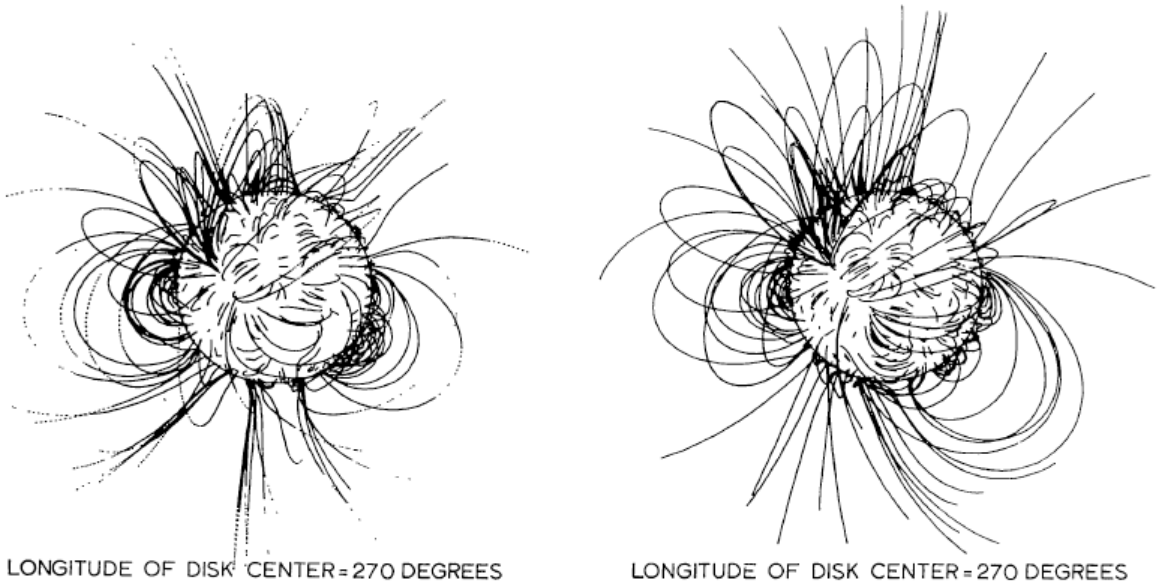

Figure 2.7: Examples of the three-dimensional structure of the coronal magnetic field computed using the potential field approximation from Altschuler & Newkirk, 1969 [2].

2.4.2 The synoptic solar wind

Numerical reproduction of the solar corona steady-state conditions has been extensively investigated since the famous work by (Pneuman and Kopp 1971 [79]). Traditionally, the deposition of energy and/or momentum into the solar wind has been described by means of some empirical source terms [100, 66, 67, 95, 114, 42, e.g.]. In these models, the sources of plasma heating and solar wind acceleration are typically modeled in a qualitative sense, and the spatial profiles for the deposition of the energy or momentum are usually modeled by exponentials in radial distance. In more realistic models, the solar wind is heated and accelerated by the energy and momentum interchange between the solar plasma and large-scale Alfvén turbulence [47, 24, 10, 102, 101].

Due to the small number of observations at 1 AU, it is reasonable to adopt semi-empirical models. Assimilating a long history of solar wind observations, these models are very efficient and quite accurate. A particular example is the Wang-Sheeley-Arge model (WSA) [6, 5]. This model uses the observed photospheric magnetic field to determine the coronal field configuration, which is then used to estimate the distribution of the final speed of the solar wind, u_{sw}. The common disadvantage of semi-empirical models is that they are physically incomplete.

I use the model by [19] to obtain the steady-state SC and IH solution. The SC and IH modules of SWMF are versions of the BASTRUS global MHD code, which is fully parallel and has adaptive mesh refinement capabilities (see [80]). Our SC model is driven by high-resolution SOHO MDI magnetograms. I use the magnetogram data to calculate the potential magnetic field, assuming the source surface is at $R_{ss} = 2.5R_{\odot}$, where $R_{\odot}$ is the solar radius, and use this distribution of the magnetic field as an initial condition.

The heating and acceleration of the solar wind plasma are achieved by using a non-uniform spatial distribution of γ. In order to obtain a more realistic distribution, I use the empirical Wang-Sheeley-Arge (WSA) model as an input to our model [6]. The WSA model is found to be very reliable although in principle, our model can use any empirical prediction for the solar wind speed such as in [30]. The WSA model uses the potential field distribution to obtain the magnetic flux tube expansion factor defined as [109]:

$$f_s = \frac{|B(R_s)|R_s^2}{|B(R_0)|R_0^2}. \tag{2.34}$$

The WSA model provides an empirical relation for the spherical distribution of the solar wind speed at 1AU as a function of f_s and the angular distance of a magnetic field footpoint from the coronal hole boundary, θ_b. In our model, I use the following formula [5]:

$$u_{sw} = 265 + \frac{1.5}{(1+f_s)^{1/3}}\left\{5.9 - 1.5e^{\left[1-(\theta_b/7)^{5/2}\right]}\right\}^{7/2} \text{ km s}^{-1}. \tag{2.35}$$

I assume that far from the Sun the total energy is dominated by the energy of the bulk motion and that the thermal and gravitational energy are negligible. I also assume that at the coronal base the bulk kinetic energy is zero. Due to energy conservation, we can use the Bernoulli equation to relate the two ends of a streamline (or magnetic field line):

$$\frac{u_{sw}^2(\theta,\phi)}{2} = \frac{\gamma_0(\theta_0,\phi_0)}{[\gamma_0(\theta_0,\phi_0)-1]}\frac{p_0(\theta_0,\phi_0)}{\rho_0(\theta_0,\phi_0)} - \frac{GM_\odot}{R_\odot}. \tag{2.36}$$

Here u_{sw} is the input solar wind speed from the WSA model, G is the gravitational constant, and $M_\odot$ is the solar mass. γ_0, p_0, and ρ_0 are the photospheric values for the

polytropic index, pressure, and mass density. The coordinates θ_0, ϕ_0 represent the location of the field line footpoint, $u_{sw}(\theta, \phi)$ originated from. I interpolate γ from its photospheric value to a spherically uniform value of 1.1 on the source surface at $r = 2.5R_\odot$. γ is linearly varied from 1.1 to 1.5 for $2.5R_\odot < r < 12.5R_\odot$, and $\gamma = 1.5$ above $12.5R_\odot$. Figure 2.8 shows the spatial distribution of γ. Once the spatial distribution of γ is obtained, I solve the MHD equations self-consistently using this location dependent polytropic index in the energy equation to obtain the steady state solution for the SC and solar wind.

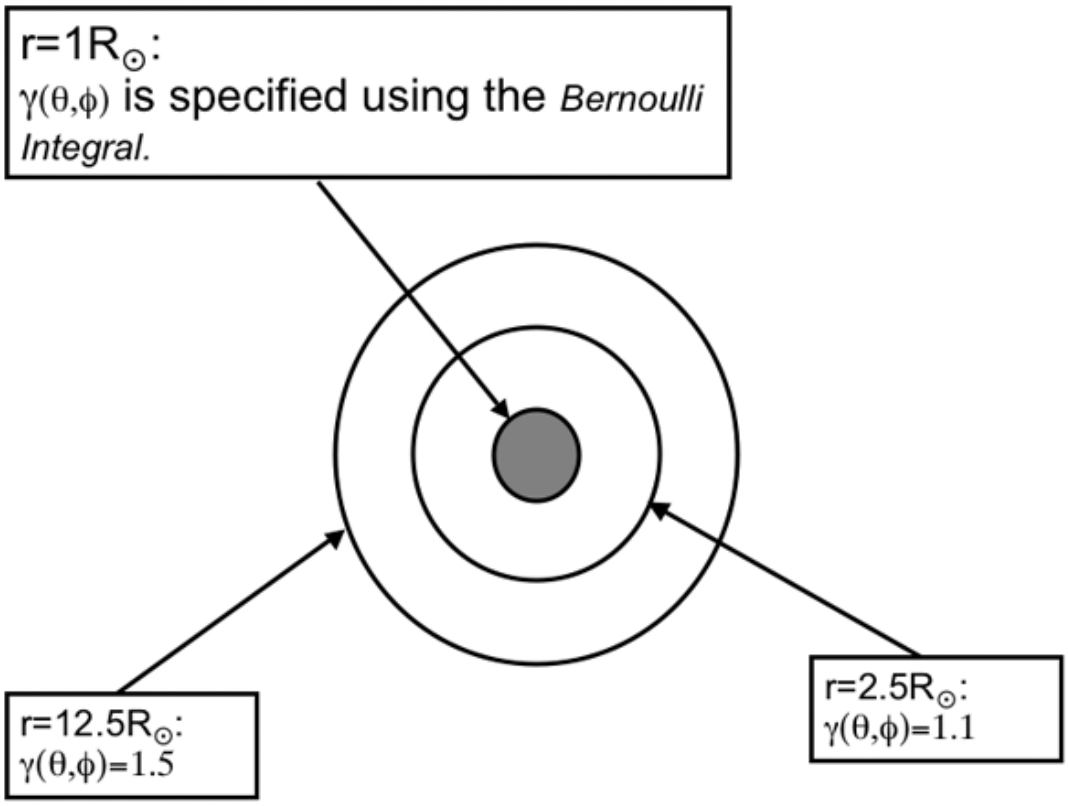

Figure 2.8: The spatial distribution of γ used in our model. γ is specified on the solar surface using the Bernoulli integral and been interpolated to spherically uniform value of 1.1 at $r = 2.5R_\odot$. γ is linearly varied to a value of 1.5 for $2.5R_\odot < r \leq 12.5R_\odot$.

The above distribution of γ enables us to reproduce the bi-modal structure of the solar wind speed. However, the distributions of the coronal density and temperature

are still not determined. It is known that the faster wind originates from coronal holes, where the density is lower than the density in the closed field regions. In order to obtain this observed property, I scale the base density, ρ_0, and the base temperature, T_0, at each point on the solar surface with the inverse of the input speed from the WSA model. I would like our model to be driven only by the magnetogram data without any particular parameterization for each Carrington Rotation (CR). Therefore, I parameterize the model for the general cases of solar minimum and solar maximum conditions.

I use 9 levels of grid refinement in the SC model to obtain a grid cell size of $0.02R_\odot$ on the solar surface. I refine the grid throughout the simulation to obtain a grid cell size of $0.2R_\odot$ near the current sheet. I run the SC model without the IH model for 10000 iterations until a steady state is obtained.

Since the solar wind is super-Alfvénic at the SC-IH boundary, all the information propagates outward. Therefore, it is sufficient to couple the models only for a single iteration if the SC module is already in a steady state. In our model, the spherical SC-IH boundary is set at $r = 17R_\odot$, while the Cartesian outer boundary for SC is set at $x, y, z = 24R_\odot$. When the coupled mode is turned on, the inner boundary in IH is driven by the SC values at $r = 17R_\odot$, while the outer boundary conditions (BCs) for SC are constrained by the IH values at the Cartesian distance of $24R_\odot$ from the center of the Sun. Therefore, the SC steady state solutions for the SC stand-alone run and coupled SC-IH run are not identical (but close). After obtaining a steady state in SC, I turn on the IH module for a coupled run of 2500 iterations. I then turn off the SC module until a full steady state in IH is achieved after another 3500 iterations. I refine the grid in the IH module to obtain a grid cell size of $r = 0.2R_\odot$ near the current sheet.

In order to obtain a more physical solution for the heliospheric current sheet, we implemented the Roe Solver (RS) to our model [92] (see App. B). The RS is the most exact and least diffusive Godunov-Type numerical solver in BATS-R-US . The use of the RS is practically equivalent to the use of another level of grid refinement. Therefore, it should better resolve the heliospheric current sheet, where magnetic reconnection occurs and the ideal MHD approximation breaks down. This is the first implementation of this new and highly sophysticated numerical solver.

I run our model on the NASA ALTIX supercomputer with the use of 64 processors for each CR. With this amount of processors, it takes about one week of wall clock time to obtain a steady state solution for 14 Carrington Rotations.

2.5 Validation of the MHD Model

2.5.1 Solar minimum

I ran the model for CRs 1916-1929 (November, 1996 to November, 1997). During this period the Sun was under solar minimum conditions and the solar magnetic field configuration was dipolar.

The relationship between the total magnetic flux predicted by the magnetogram-driven potential field model and the total magnetic flux observed at 1AU is still under debate. Currently, the MDI data provider recommends that I multiply the magnetogram values by a factor of 1.8. However, for solar minimum conditions, I obtain a better result for the magnetic field with the use of a scaling factor of 2.5. For solar minimum, I use a base density value of $\rho_0 = 4.3 \times 10^8\ cm^{-3}$.

Figure 2.9 shows a cut along the $y = 0$ plane in the frame of reference rotating with the Sun, which represents the central meridian of CR 1922. Color contours represent the radial solar wind speed, while streamlines represent the magnetic field lines. I obtain a thin current sheet surrounded by slow solar wind speed of $300 - 400\ km\ s^{-1}$, which extends up to 20° above and below the current sheet.

Figures 2.10-2.13 show a comparison of the simulation results with ACE and WIND 1AU data. The comparisons are for solar wind radial speed, magnetic field magnitude, plasma number density, and plasma temperature. Shaded transitions mark the Carrington rotations. The red line represents hourly averaged satellite data obtained from http://cdaweb.gsfc.nasa.gov, while the black line represents an extraction of the MHD variables along the satellite trajectory during the particular CR in the steady state simulation domain using the same time interval as the satellite data. The yellow bars mark the periods of time when CMEs were observed [16, 48]. Since these are dynamical transients, the steady state model should not be

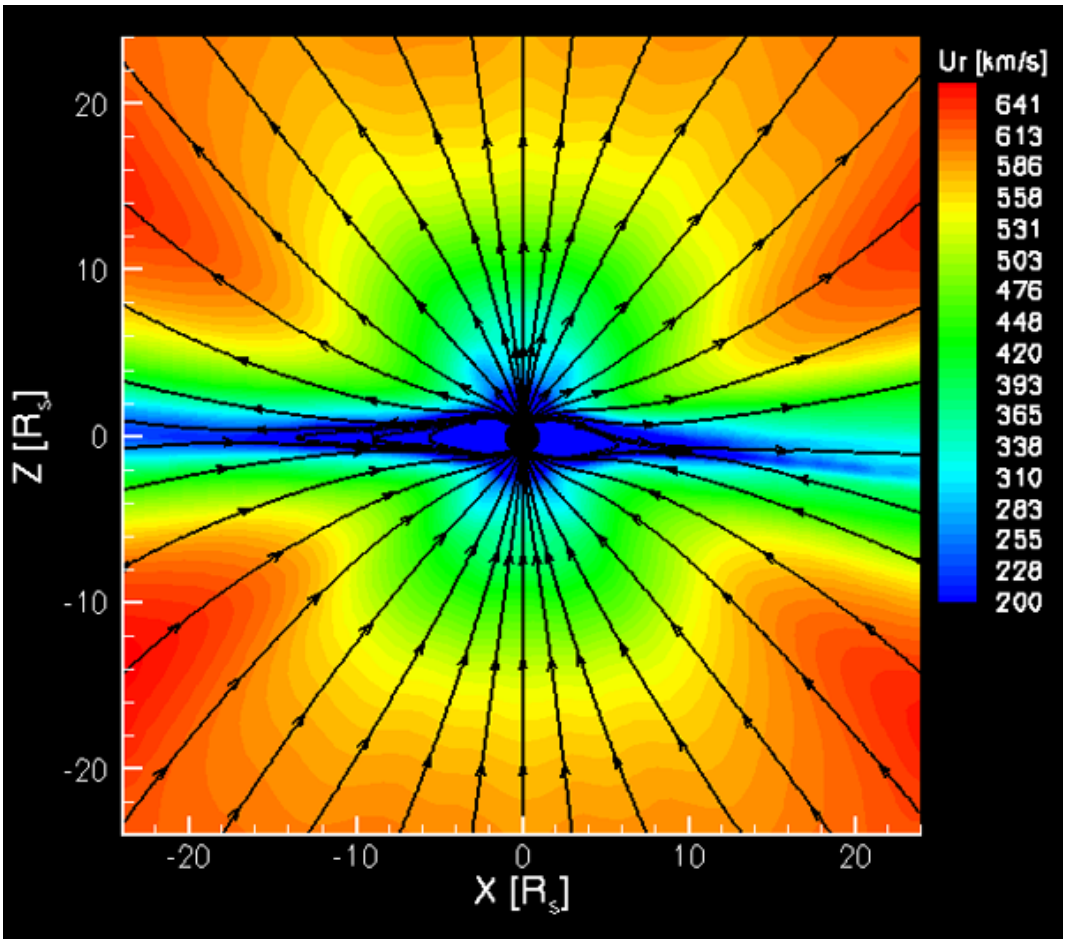

Figure 2.9: A cut in the steady state solution for the SC during CR1922. Color contours represent the radial solar wind speed and streamlines represent the magnetic field lines.

expected to match the observations at these particular periods. Nevertheless, the model predicts rather well the periodic co-rotating interaction regions (CIRs). In order to avoid the effect of the CME transients on the statistics, I set both data and model values to be zero during these periods.

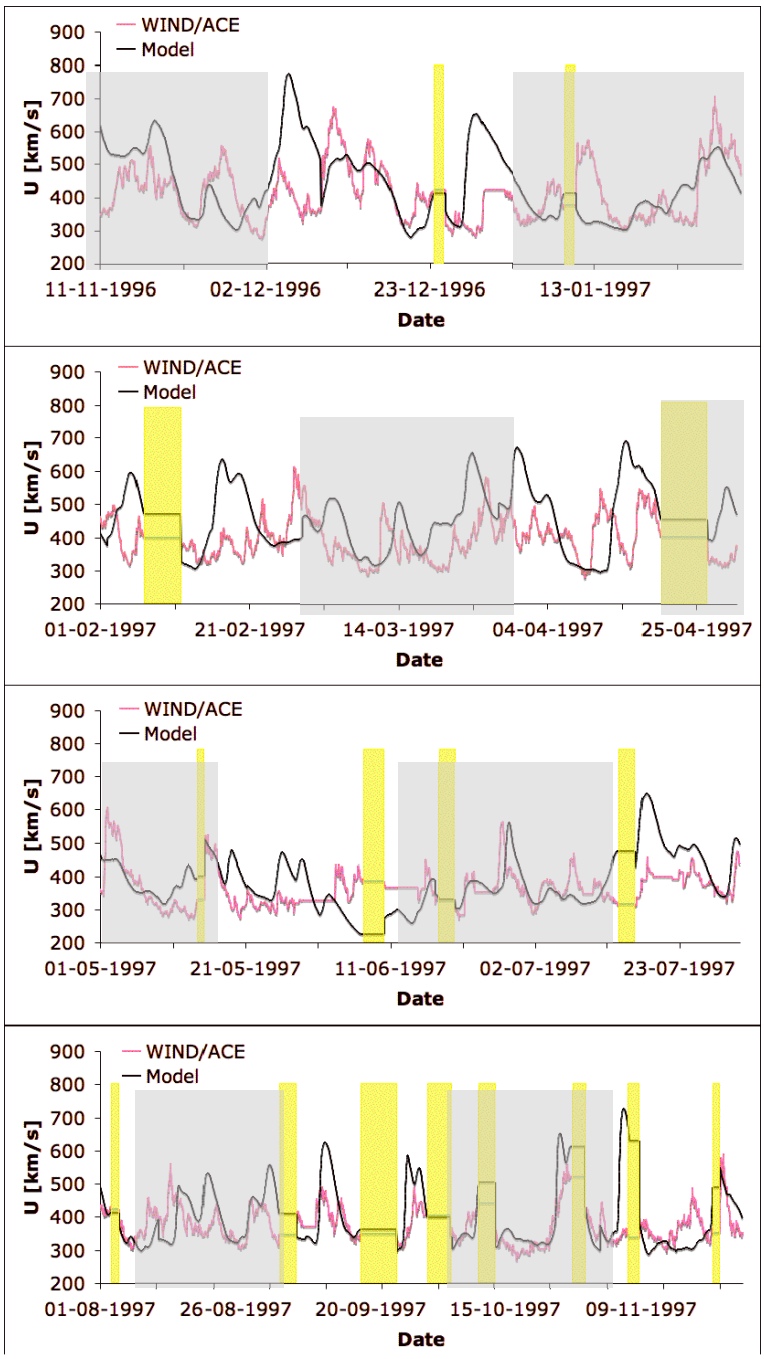

Figure 2.10: A comparison of the simulation results with ACE and WIND data at 1AU for solar wind radial speed.

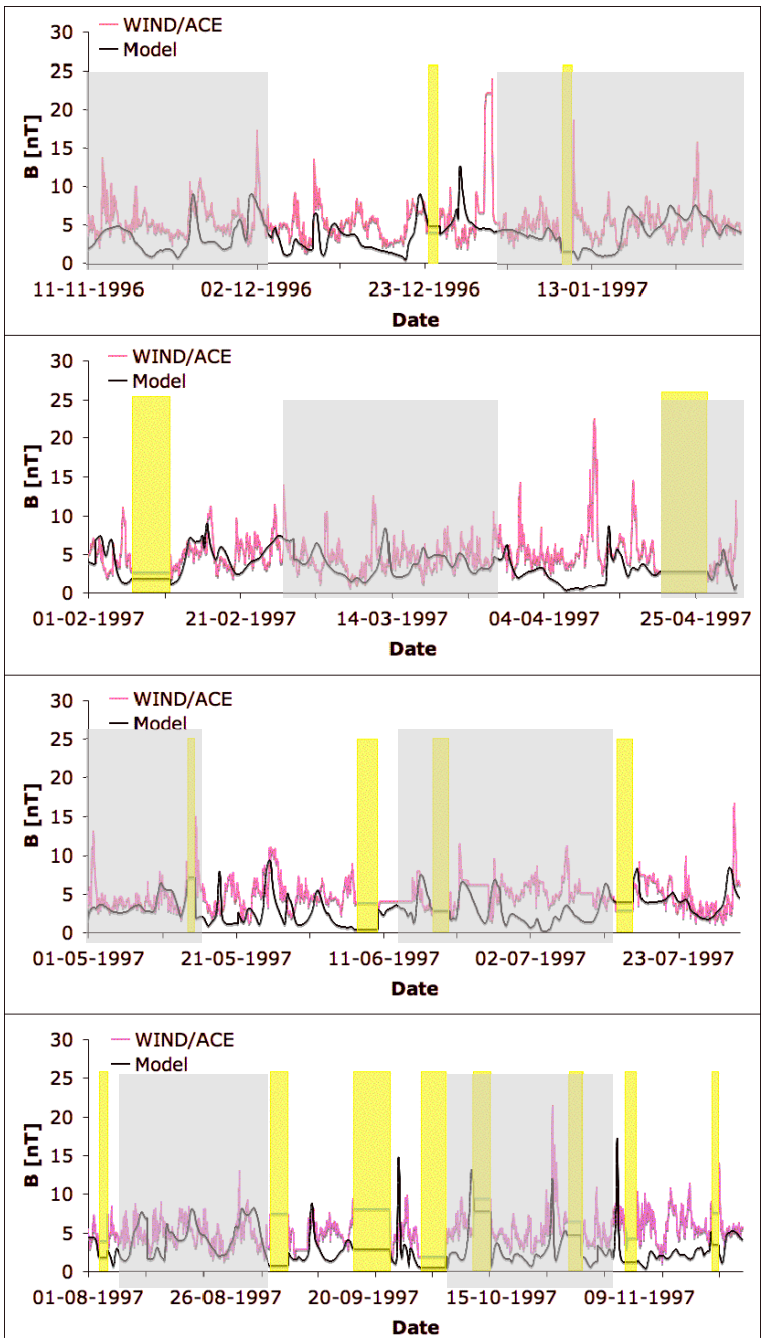

Figure 2.11: A comparison of the simulation results with ACE and WIND data at 1AU for magnetic field magnitude.

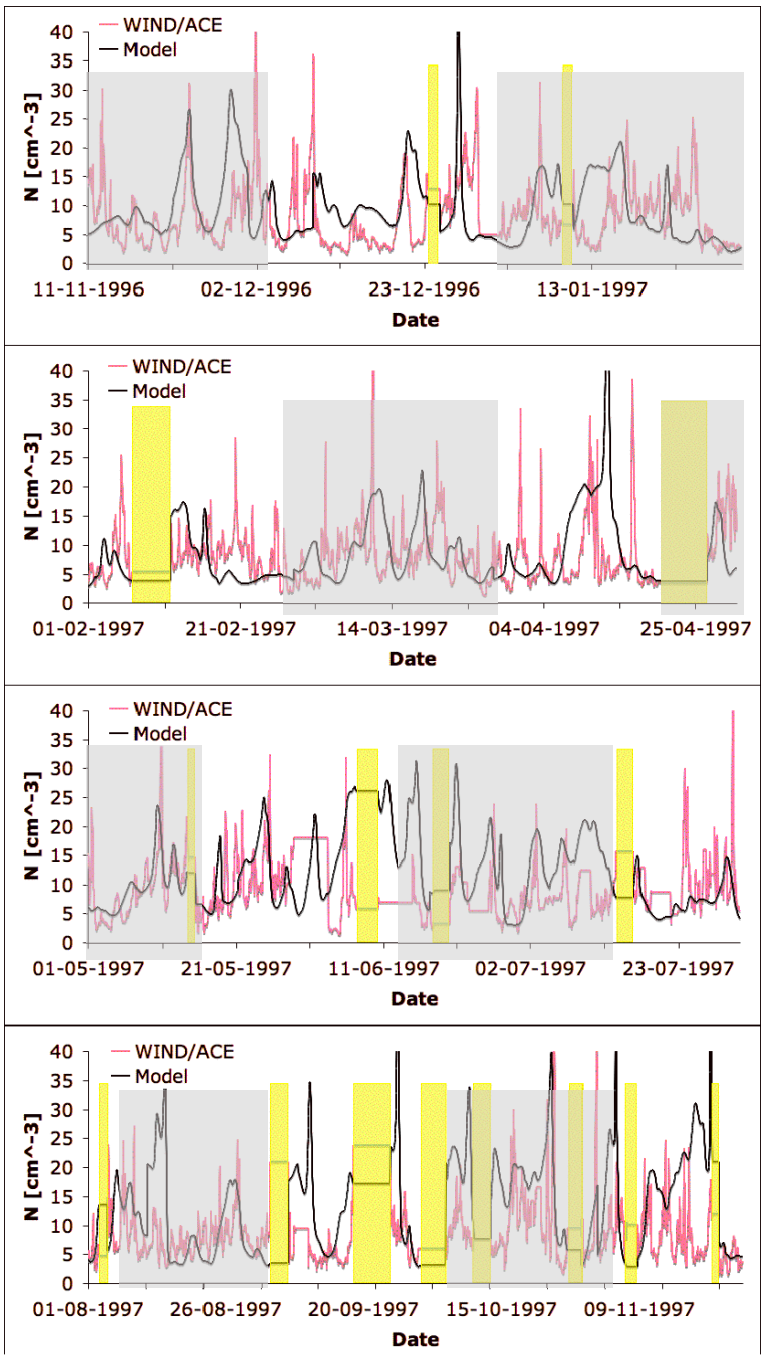

Figure 2.12: A comparison of the simulation results with ACE and WIND data at 1AU for plasma number density.

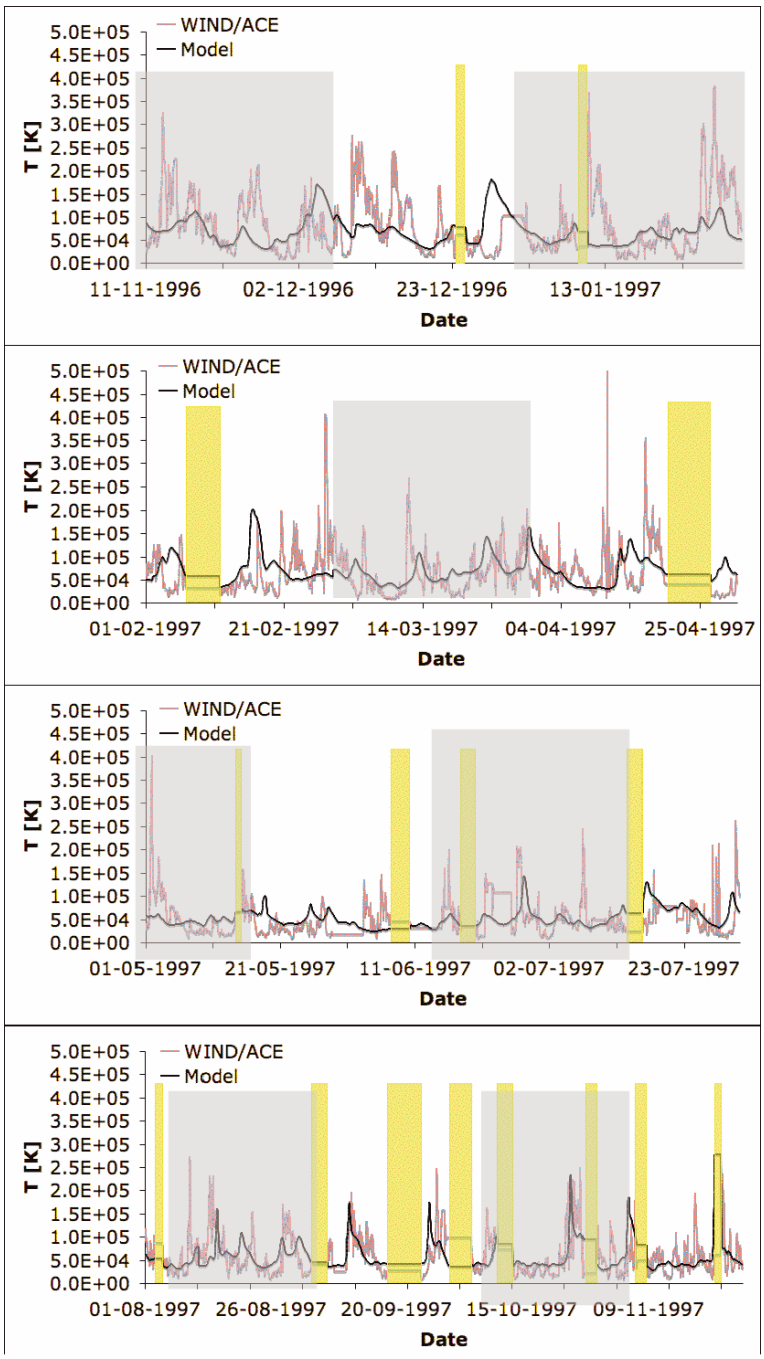

Figure 2.13: A comparison of the simulation results with ACE and WIND data at 1AU for plasma temperature.

Table 2.1 shows statistical analysis of the results for solar minimum conditions. It shows the cross-correlation (CC) between the model and the data (excluding the CME transients) and normalized root mean square (RMS) error. The values are for the solar wind radial speed, u_r, plasma number density, N, magnetic field, B, and plasma temperature, T. The CC between the data and the model is very good (0.8) for u_r and reasonable (0.4) for the other variables. In particular, the model provides reasonable magnitudes of all the magnetohydrodynamic variables simultaneously, and the normalized RMS error is less than 1 (it is only 27% for u_r).

Overall, the model predicts interplanetary features rather well (which can be obtained by a steady-state model) such as CIRs and transients from fast to slow solar wind. However, in some cases, the inaccuracy in the solar wind speed shifts the features onset time earlier or later as compared with the observations.

Table 2.1: Statistics for solar minimum results.

	Cross-correlation	Normalized RMS
u_r	0.82	27%
N	0.35	87%
B	0.4	59%
T	0.4	65%

2.5.2 Solar maximum

I run the model for CRs 1972-1984 (January,2001 to January,2002). During this period the Sun was under solar maximum conditions and the solar magnetic field was highly structured and was not dipolar any more.

For solar maximum conditions, the magnetic flux obtained in the simulation is smaller than the observed flux at 1AU by a factor of at least 1.5, even when the magnetogram scaling factor is 4. For solar maximum case, I multiply the model result for the magnetic field at 1AU by a factor of 2, after using a scaling factor of 4 for the input MDI magnetogram. I discuss this magnetic flux issue in Section 4.2.

For solar maximum, I use base density value of $\rho_0 = 3.5 \times 10^8\ cm^{-3}$, which is slightly smaller than the base density used for solar minimum.

Figure 2.14 is similar to Figure 2.9 but for solar maximum conditions during CR1973. One can see that the heliospheric current sheet is highly tilted and the slow solar wind extends to higher magnetic latitudes.

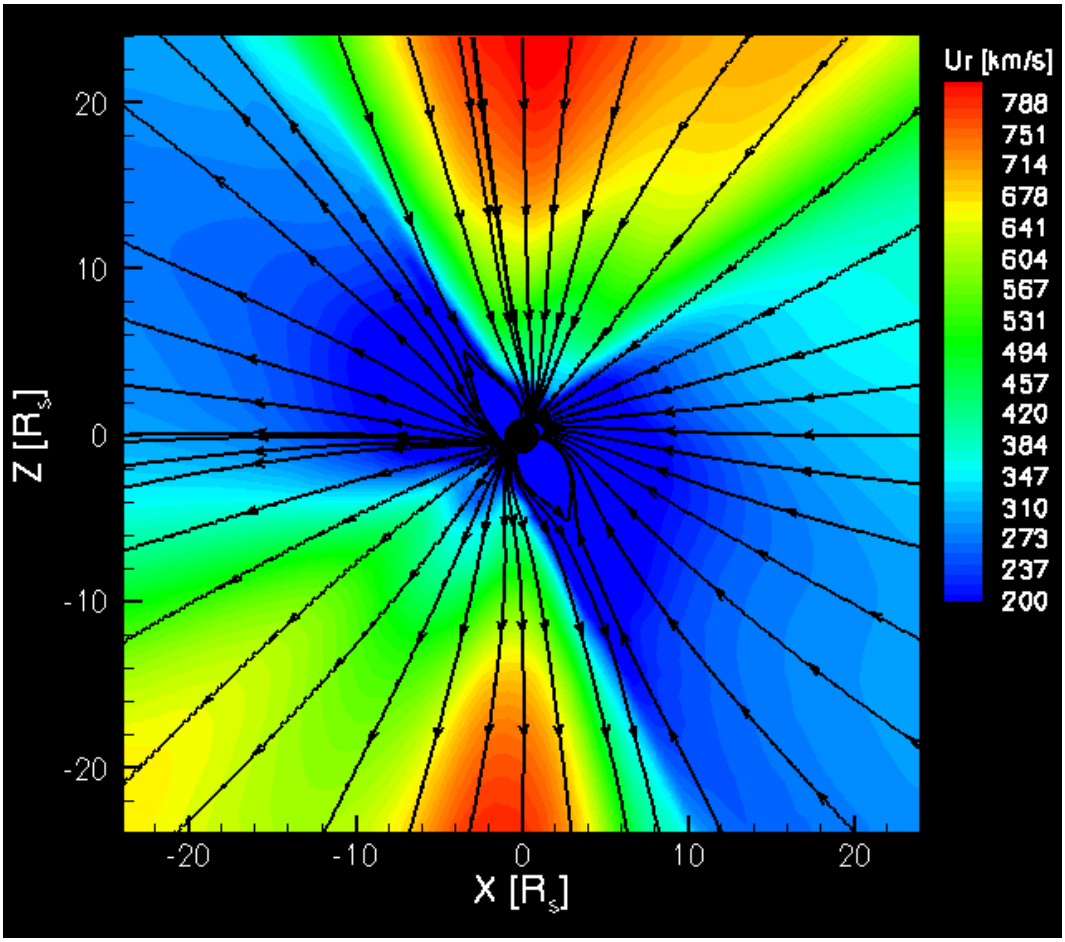

Figure 2.14: A cut in the steady state solution for the SC during CR1973. Color contours represent the radial solar wind speed and streamlines represent the magnetic field lines.

Figures 2.15-2.18 show a comparison of the model results with ACE data. Display settings are the same as Figures 2.10-2.13, and one can see that the amount of CME transients (yellow bars) is larger than in the case of solar minimum.

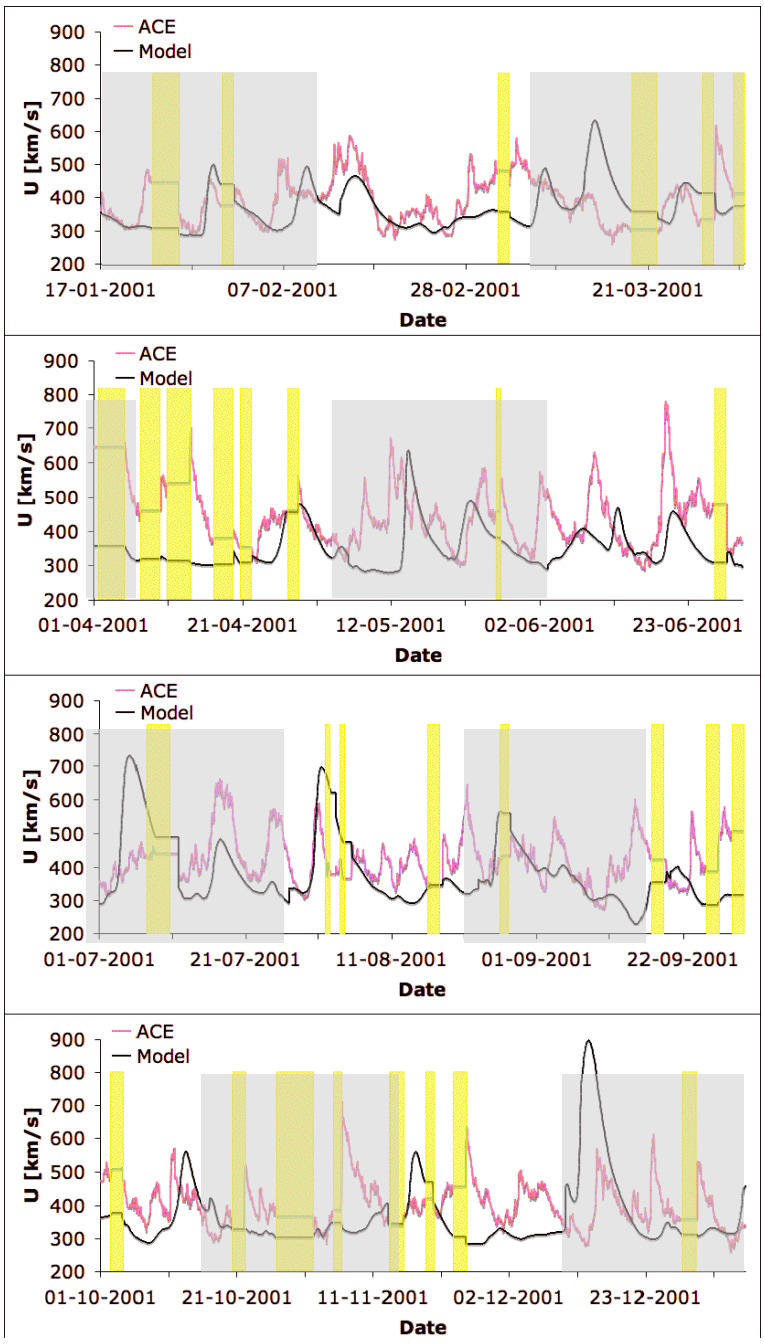

Figure 2.15: A comparison of the simulation results with ACE data at 1AU for solar wind radial speed.

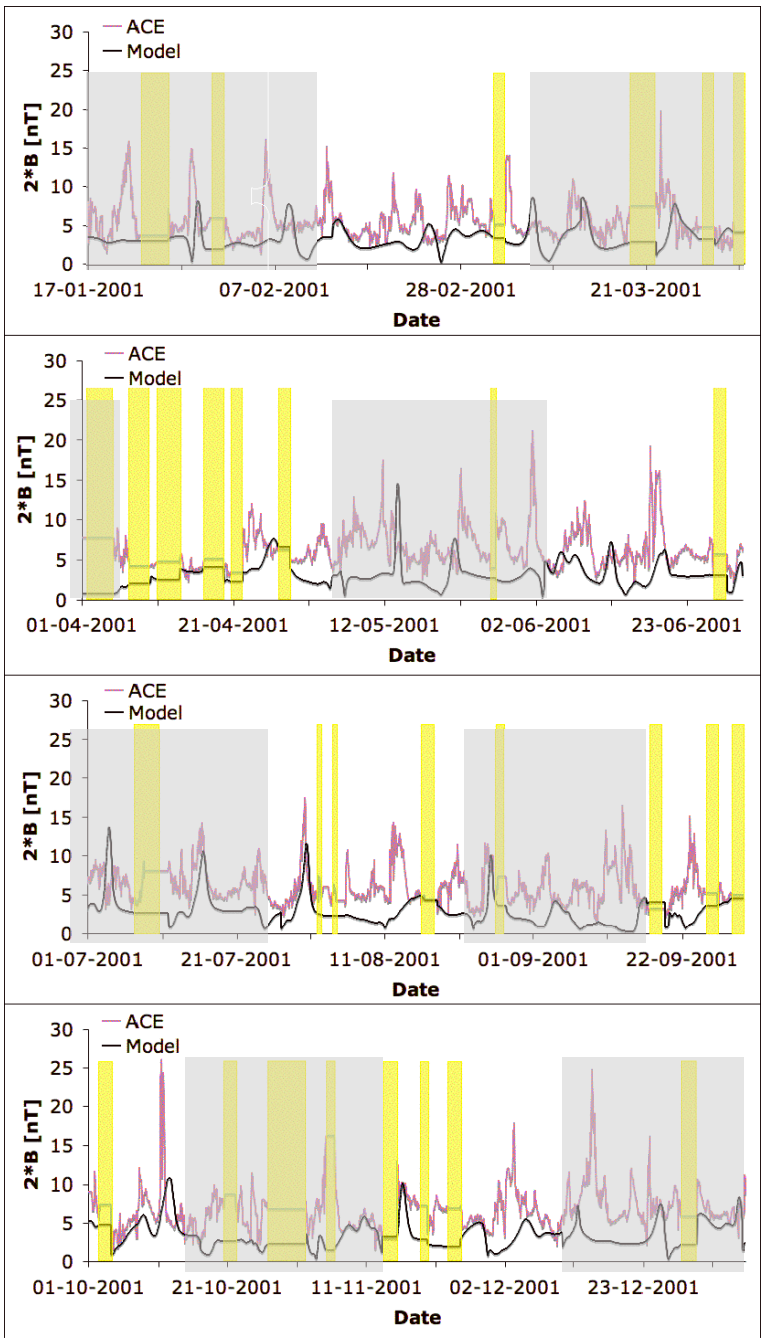

Figure 2.16: A comparison of the simulation results with ACE data at 1AU for magnetic field magnitude. The magnetic field from the simulation is multiplied by 2.

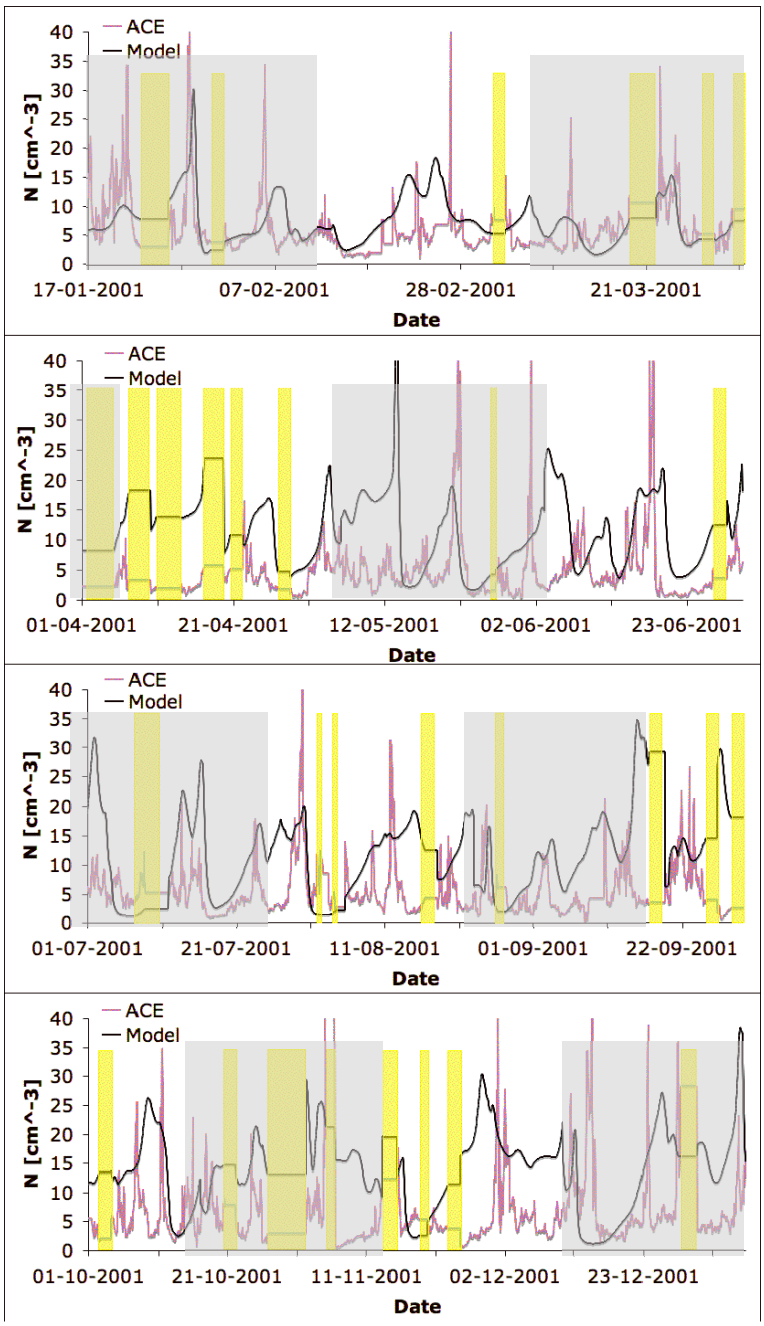

Figure 2.17: A comparison of the simulation results with ACE data at 1AU for plasma number density.

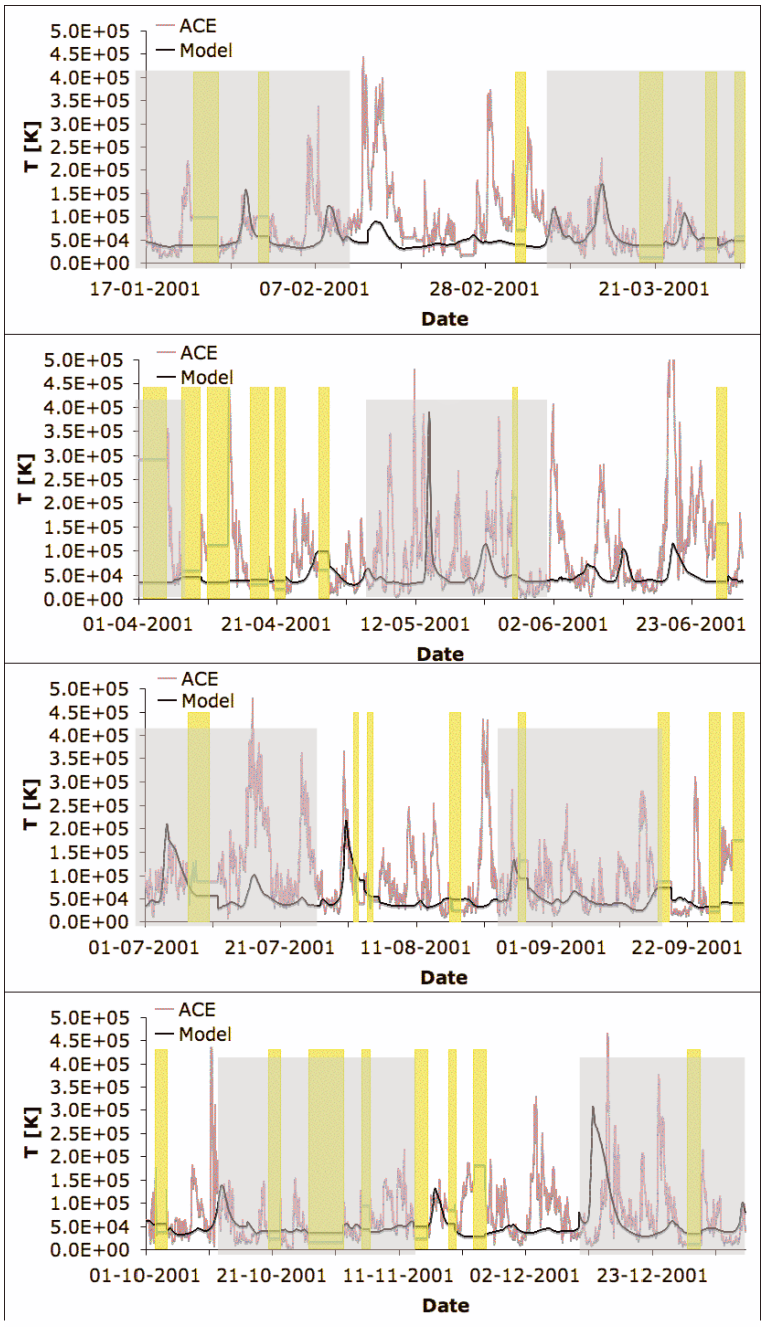

Figure 2.18: A comparison of the simulation results with ACE data at 1AU for plasma temperature.

Table 2.2: Statistics for solar maximum results.

	Cross-correlation	Normalized RMS
u_r	0.79	29%
N	0.32	97%
B	0.5	62%
T	0.32	75%

Table 2.2 shows a statistical analysis of the solar maximum results. Overall, the statistics is similar to solar minimum case, except for the fact that it has been done with the models result for the magnetic field multiplied by another factor of 2.

2.6 Discussion on the Results of the MHD Model

In this work, I attempt to validate our model by comparing its output with satellite data at 1AU. The success was not guaranteed because the satellite measures the solar wind parameters along a particular trajectory, and the local values could be poorly predicted even by a global model, which is correct overall. Especially subject to errors are the model predictions for the vicinity of the current sheet. With the model prediction for the sheet location offset by only few grid points, the predicted solar wind speed would be much higher than observed. Nevertheless, the model predictions of the measurements are rather good, even for solar minimum when the satellite is located close to the current sheet. It is also important that we benefit from the reliability and simplicity of the WSA model without loss of accuracy.

For solar maximum, the most meaningful result is the fact that the magnetic field magnitude at 1AU cannot be reproduced by the MHD model without using a very large scaling factor for the magnetogram data. This result is consistent with the idea that during solar maximum, about $30 - 50\%$ of the observed heliospheric open flux originates from active regions and CMEs interchange reconnection [33, 68, 110, 87, 71, 81]. Because the surface value of γ in our model is uniform in the closed field regions (where the expansion factor goes to infinity), our model is essentially

"blind" to this region and cannot reproduce the magnetic flux originated from active regions. Although the prediction of the heliospheric open flux by the MHD model is not perfect, it is still useful in predicting space weather events. This is due to the fact that the most crucial parameter for space weather forecasting is the arrival time of the interplanetary shock and the orientation of B_z (which I do not attempt to predict in this work). If the model can provide a reasonable prediction for the speed, density, and B_z, we should expect the magnitude of the background magnetic field to be less important. However, the B_z of the wind is often compressed and amplified in the sheath to a level that is geoeffective.

In this work, I adjust the model parameters for each type of solar conditions in order to investigate whether this model can be operational. It appears that the results could be slightly improved by parameterizing the model for each particular CR, in particular, the solar wind speed and the arrival time of the periodic features such as CIRs.

2.7 Conclusions for the MHD Model

I have developed a three-dimensional model for the solar corona and the inner heliosphere. I have performed a long-term validation of the model for one year of solar minimum and one year of solar maximum using comparison of the model results with satellite observations at 1AU [20]. Overall, the model is found to predict rather well the magnitude of the magnetohydrodynamical variables, as well as the quiet heliosphere periodic features, in particular for solar minimum conditions. For solar maximum conditions, the model predicts the solar wind speed, density, and temperature reasonably well. However, the model's prediction for the magnetic field magnitude at 1AU is still not reliable enough.

It is important to note that even though the model still needs some improvements, it provides a very good solution considering the fact that it is driven by magnetograms. This model, as well as the WSA model, has a dependency on the potential field approximation and the location of the source surface, which introduces another degree of freedom. Even though the model seems to be useful, I assume it will provide better result with the application of a more self-consistent solar wind heating mechanism such as Alfvén wave heating.

In addition to space weather forecasting, the model can provide information about the large-scale structure and long-term evolution of the heliospheric magnetic field. This information can be useful to investigate large number of physical phenomena such as particle transport, evolution of the Parker spiral, interaction of the solar wind with the outer planets and comets, and the solar dynamo. In the context of space weather, I plan to investigate the model's capabilities to predict B_z at 1AU, which is a parameter of great importance for predicting geomagnetic activity.

2.8 Model Solution with Fisk's Heating Function

I run the model for the solar corona with Fisk's solution for the final solar wind speed (eq. 1.13). I define T_e to be a function of $\left[\frac{B_r(R_\odot)}{|\mathbf{B}(R_\odot)|}\right]^2$ so that $T_e = 800,000\ K$ in coronal holes and $T_e = 1.5 \times 10^6\ K$ in the helmet streamers. These parameters were taken from Feldman et. al 1999 [28] and one can show that these temperatures match final solar wind speed of $400 - 800\ km\ s^{-1}$ with the proper choice of the constant A.

Figure 2.19 shows a comparison between the Fisk's model with the WSA model results. The main conclusion is that even though the input speed between the models is not identical, the large scale steady-state is similar. This simulation requires further investigation, since the final speed from the Fisk's model is more structured.

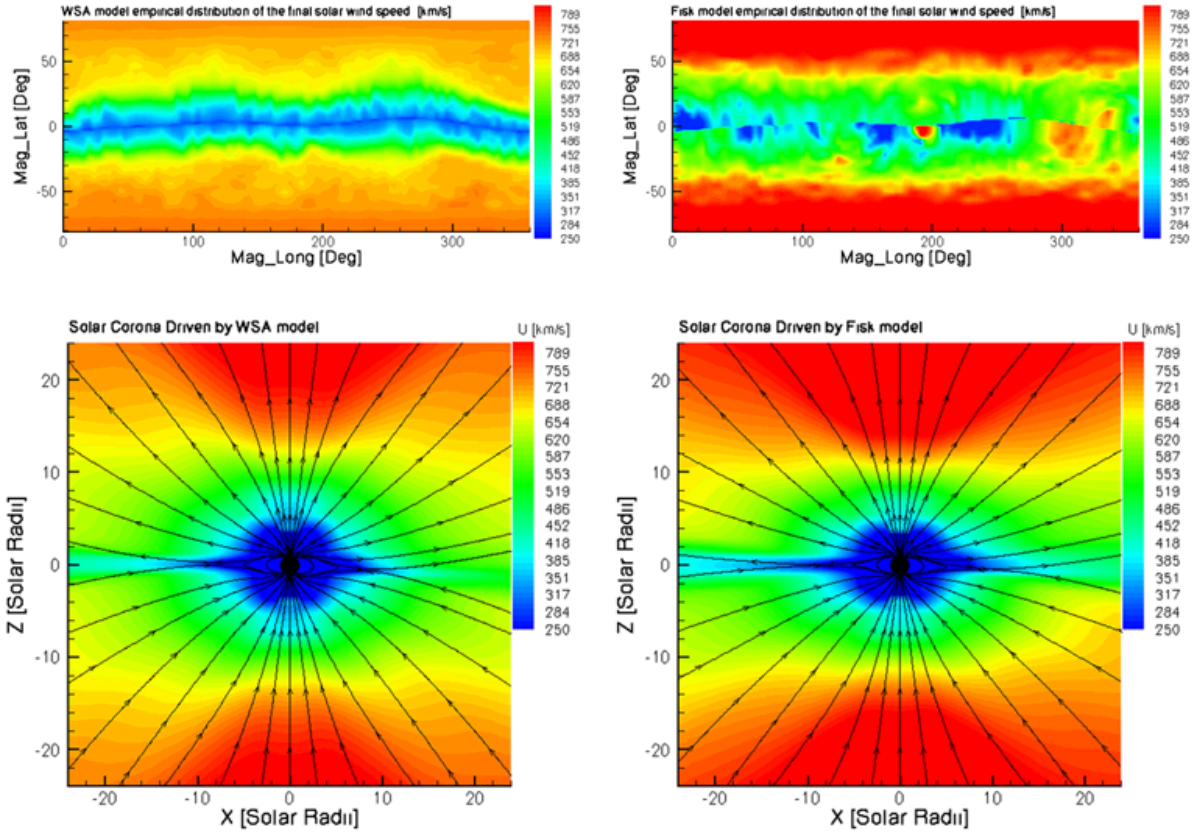

Figure 2.19: Comparison between the results for the WSA model (left) and Fisk's model (right) for the final speed distribution (top) and the steady-state solution for the solar corona (bottom). Color contours represent the solar wind speed and streamlines represent magnetic field lines.

CHAPTER III

Magnetic Reconnection Processes in the Solar Corona

"Perhaps most troubling at least to me is the behavior of the poloidal field. In the above discussion we converted the toroidal field into a poloidal field by the effect. Yet if you look at the Sun the poloidal field basically opens into the heliopshere. The field at the poles of the Sun at solar minimum forms the heliopsheric magnetic field, and reverse polarity every 11 years. We will argue that the poloidal field is quite constant during the solar cycle, and moves on the solar surface by interactions with closed flux. Its behavior has nothing to do with an internal dynamo. This is something that has not been resolved."

Lennard Fisk - class notes on the Sun and the Heliosphere

3.1 Magnetic Reconnection Processes and the Solar Meridional Flow

In this chapter I investigate the transport of the open magnetic flux of the Sun as part of the general circulation of the solar magnetic field. This work is the first numerical work to study the possible coupling between the internal solar dynamo and the evolution the magnetic field in the solar corona. solar dynamo models, on one hand, treat the global circulation of the internal magnetic field of the Sun without taking into account the coronal field. Solar corona models, on the other hand, take

into account only the field above the surface and the inner boundary conditions are specified in some arbitrary manner (but with strong physical or observational basis though). With the current computational capabilities, we are still unable to perform a complete coupled numerical simulation of the solar interior and the solar corona. For this reason, we need to investigate one aspect of this coupling at a time.

Meridional motions are significant both in the photospheric flux-transport models [108, 106, 111, 107, 61, 60], and in flux-transport dynamo models [26, 25]. It has been demonstrated by both types of models that an average meridional flow with a magnitude on the order of $10 - 20\ m\ s^{-1}$ is required to maintain the magnetic dynamo, and to obtain the field reversal. In addition, some recent papers suggest that a modification of the meridional flow can explain the variations from one solar cycle to another [88, 26, 107].

The surface motions on the photosphere consist of differential rotation, random convective motions, and meridional flow. While the differential rotation has been extensively investigated using GONG and SOHO MDI measurements [45, 44, 86], and the random motion has been studied by several authors [53, 108, 89, 15], it is difficult to characterize the meridional flow due to its weak signal compared to the differential motion. Early estimates of the meridional flow from day-to-day ground based Doppler measurements [27] obtained a flow of the order of $20\ m\ s^{-1}$. More recent Doppler estimates were done using GONG and MDI data [45, 11], and were in agreement with an average flow of $20\ m\ s^{-1}$. However, these measurements showed that the flow can be enhanced by a factor of 2-3 during the solar cycle. Helioseismology analysis of MDI data [116] obtained a meridional flow on the order of $20\ m\ s^{-1}$ as well. A different approach to estimate the photospheric meridional flow was done by tracking the motions of magnetic features on the solar surface using

magnetogram data [51, 52, 91]. The average meridional flow was found to be of the order of 10 $m\ s^{-1}$ with variations of up to 5 $m\ s^{-1}$ during the solar cycle. All the above observations agree with the theoretical restriction of a maximum meridional flow speed on the order of $10 - 20\ m\ s^{-1}$.

As mention above, the meridional flow is important for the transport of magnetic flux on the Sun. The magnetic flux of the Sun is composed of closed magnetic flux regions, where both ends of the magnetic field lines are attached to the Sun, and open magnetic flux regions, where one end of the field lines is attached to the Sun and the other end is dragged by the solar wind into the heliosphere. While the closed magnetic field lines are located within the Alfvénic point, the heliospheric magnetic field is controlled by the open magnetic flux. During solar minimum conditions, the open flux geometry is of two coronal holes with opposite polarity separated by a single current sheet; the magnetic polarity is reversed approximately every 11 years, possibly due to rotation of the current sheet [85, 32]. It has been observed that the open magnetic flux of the Sun remains virtually constant throughout the solar cycle comparing to the total flux [106, 110]. In addition, it has been argued that CMEs do not change the background amount of open flux through the process of interchange reconnection [23, 31]. Under these assumptions, Fisk and co-workers, in a series of papers [29, 31, 33, 32], constructed a new transport model for the evolution of the open magnetic flux of the Sun. The model proposed by Fisk and co-workers (hereby Fisk model) is an alternative for the common use of the potential field approximation (see Section 2.4.1) in describing the solar magnetic field. The potential field approximation is a very convenient tool to describe a static configuration of the solar corona magnetic field and to get the location of the boundary between the open and closed magnetic flux regions. It is also very straightforward to implement in numerical

models since it requires only the harmonic coefficient extracted from the measured line-of-sight photospheric magnetic field and the use of associated Legendre polynomials. However, the potential field approximation can only give a static snapshot in time and does not describe the continuous *dynamic* evolution of the coronal magnetic field.

The Fisk model, in turn, proposes a *dynamic* model for the evolution of the open magnetic flux in the photosphere, solar corona, and heliosphere through solar differential rotation and magnetic reconnection of open field lines with closed loops. The effect of solar differential rotation on the evolution of the heliospheric magnetic field as predicted by the model has been studied both theoretically [90, 23, 14, 13] and numerically [57]. In this chapter, we present a numerical simulation of the transport of open magnetic flux on the surface of the Sun. We solved the two-dimensional advection-diffusion equation for the open (radial) component of the solar magnetic field taken from [31]:

$$\frac{\partial B_o}{\partial t} = \nabla^2(\kappa B_o) - \nabla \cdot (\mathbf{u} B_o). \tag{3.1}$$

The advection term in the equation represents the real motion of the plasma on the solar surface and the components of $\mathbf{u}$ are the solar differential rotation and uniform meridional flow. The diffusion term represents two diffusion processes: (1) diffusion of field lines footpoints in the network lanes and (2) diffusion due to reconnection of open field lines with closed loops proposed by [31]. We investigate the steady state solution for the photospheric magnetic field for solar minimum and solar maximum conditions. We then compare the results for a case in which we use only the uniform network lanes diffusion, and for another case, in which we include the diffusion

due to reconnection. Previous work has been done to study the evolution of the open magnetic flux on the solar surface [106, 111, 110, 107, 61, 60]. However, these studies did not include the effect of magnetic reconnection in the diffusion term as our model does. Flux transport through reconnection process can be described as a modification of the large-scale advection motion [31]. Therefore, diffusion due to magnetic reconnection can be an effective mechanism to modify the surface flow on the Sun, in particular, the meridional flow which has been observed to have temporal variations. We investigated the role of diffusion resulting from magnetic reconnection in the temporal variations of the meridional flow.

3.2 Physical Model

3.2.1 Theory

The theoretical description of the model for the transport of open magnetic flux due to reconnection with loops follows [31]. There are several assumptions that the model makes. As mentioned in the previous section, it is assumed that the open magnetic flux remains virtually unchanged during the solar cycle. The size of the loops is much smaller than the size of supergranules, and the loops are randomly oriented. The magnetic flux concentrations on the surface act like particles, so that the random motion of the field line footpoints in the network lanes as well as the motion due to magnetic reconnection can be described as a diffusive process. Every time two field lines with opposite polarity meet each other in the low corona they reconnect. When two loops meet, they reconnect to create a larger loop and a smaller loop of secondary importance. When an open filed line meets a loop, the magnetic reconnection causes the open field line to be transported by a distance of the scale of the size of the loop. In both cases, a smaller loop is created and the model assumes that this loop subducts and gets out of the system.

The mathematical derivation of the model takes into account the rate of emergence of loops, average size, and average amount of magnetic flux of the loops on the solar surface. In addition, some numerical factors arise due to the fact that the diffusion coefficient, κ, is a two-dimensional tensor, and also because magnetic reconnection occurs only on one side of the loop.

The theory manifests in equation (3.1). The components of the advective velocity $\mathbf{u} = (u_\theta, u_\phi)$ are [111, 107]:

$$u_\phi = 13.38 - 2.30 \sin^2 L - 1.62 \sin^4 L \;\; deg\ day^{-1},$$

which represents the solar differential rotation and,

$$u_\theta = v_m \cos^2 L |\sin L|^{0.025},$$

with

$$v_m = 10\ m\ s^{-1},$$

which represents the poleward meridional flow. Here L is the heliospheric latitude.

The diffusion coefficient, κ, is given by:

$$\kappa = \frac{\delta \bar{h}^2}{2\delta t}\left(1 + \frac{B_l}{B_o}\right). \tag{3.2}$$

The term $\delta\bar{h}^2/(2\delta t)$ represents the constant diffusion coefficient due to the random motion of the field line footpoints in the network lanes with a typical value of 600 $km^2\ s^{-1}$ [106, 32]. This diffusion coefficient is modified by the magnetic reconnection processes, and it depends on the density of the open magnetic flux, B_o, and on the magnetic flux contained in the loops emerging on the surface, B_l.

Equation (3.1) can be written in the following convenient form:

$$\frac{\partial B_o}{\partial t} = -\nabla \cdot [(\mathbf{u} + \mathbf{w}) B_o] + \kappa \nabla^2 B_o, \tag{3.3}$$

where

$$\mathbf{w} = -\frac{1}{B_o}\nabla\left(\frac{\delta\bar{h}^2}{2\delta t}B_l\right). \tag{3.4}$$

Here $\mathbf{w}$ is the additional velocity due to the reconnection events. This velocity depends on the gradient of B_l. Therefore, if the rate of emergence of loops is smaller at the poles, there will be an effective poleward motion in addition to the meridional flow. In our simulation, we introduced the following linear dependence of B_l on B_o:

$$B_l = 10 - 8.5\frac{|B_o|}{\max|B_o|} \quad [G]. \tag{3.5}$$

The physical reason for this relation is the fact that the loops are destroyed by reconnection faster where the open magnetic flux is larger.

Equation (3.5) states that the magnetic flux of emerging loops B_l is strong (about 10 G) in regions where the magnitude of B_o is weak (outside of coronal holes) and weak (about 1.5 G) in regions where the magnitude of B_o is strong (inside coronal holes) [31].

In general, equations (3.3,3.4) describe a mechanism to modify the convective component ($\mathbf{u}$) of the open flux on the solar surface. The azimuthal component of $\mathbf{w}$ modifies the differential rotation (u_ϕ), while the meridional component of $\mathbf{w}$ modifies the large-scale surface meridional motion (u_θ). Equation (3.3) demonstrates that the global motion on the photosphere is a combination of both advective and diffusive motions. It also demonstrates how the processes above the photosphere are important for the general circulation of the magnetic field of the Sun.

3.2.2 Grid and Boundary Conditions

For our simulation, we used a uniform, two-dimensional spherical mesh of 180×360 grid points with one degree resolution in θ and ϕ, respectively. The boundary

conditions in longitude (ϕ) are periodic and for the poles ($\theta = 0, \pi$), we use the 180 degrees cross cells as the ghost cells for the first grid points from the pole.

3.2.3 Numerical Scheme

The advective term, **A**, of equation (3.1) is discretized with a conservative two-stage Lax-Wendroff scheme. The diffusive term, **D**, is added using an implicit time and central spatial discretization:

$$B_o^{n+1} = B_o^n + \mathbf{A}(B_o^n) + \mathbf{D}(B_o^{n+1}). \tag{3.6}$$

This linear system is solved using BiCGSTAB method [104].

If the diffusive term had been solved explicitly, the stability condition would allow a time step of the order of $\Delta t = 10^{-1}$ sec. The CFL stability condition for the advective term allowed a time step of the order of $\Delta t = 50$ sec. We applied filtering by averaging the first and last latitude grid rows; this filtering practically increased the size of the smallest cells and, as a result, the time step allowed by the CFL stability condition increased as well. The use of filtering and implicit scheme for the diffusive term allowed a time step of $\Delta t = 150$ sec, which resulted in a much faster convergence to steady state.

3.2.4 Initial Conditions

The initial distribution of the open magnetic flux was set using the Potential Field Source Surface extrapolation [1]. The harmonic coefficients were taken from the Stanford WSO webpage (http://soi.stanford.edu/~wso) and the field configuration was mapped to the solar surface. Although we use the observed field configuration, our investigation does not require the use of the real field and can instead use an idealized dipole configuration. Figure 3.1 shows the initial distribution of the magnetic flux for solar minimum (CR1908) and for solar maximum (CR1959).

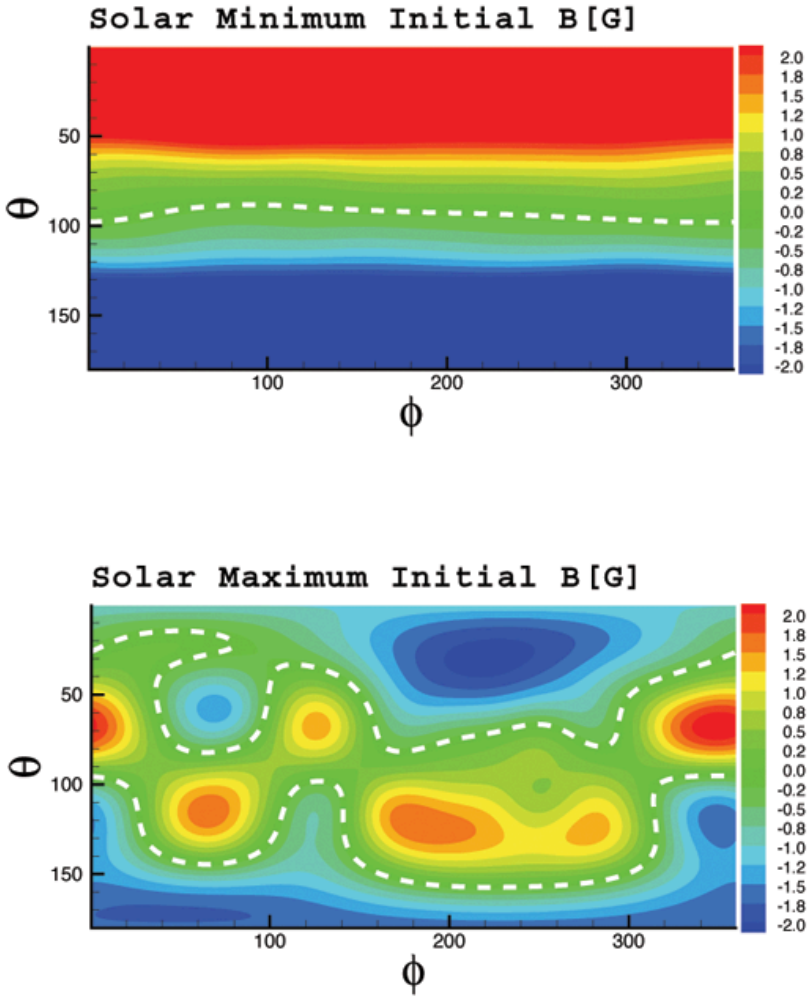

Figure 3.1: Initial distribution of the open magnetic flux (radial magnetic field) on the solar surface for solar minimum conditions (CR1908 - top) and for solar maximum conditions (CR1959 - bottom). The white dashed line marks the location of the current sheet.

3.3 Simulation Results

We simulated the transport of open magnetic flux on the surface of the Sun. For each iteration, in addition to advancing the solution for the magnetic flux density, we calculated the diffusion coefficient, κ, and the velocity, $\mathbf{w}$, which is a result of the reconnection process. Figure 3.2 shows the diffusion coefficient and the components of $\mathbf{w}$ for solar minimum and solar maximum initial conditions.

For solar minimum case, there is a preferred, large-scale, poleward gradient in κ, and $\mathbf{w}_\theta$ has a magnitude of $2 - 7\ m/s$, which is the same scale as the background meridional flow. The sign of $\mathbf{w}_\theta$ corresponds to latitude, meaning that negative flow is northward and positive flow is southward. We calculated $\mathbf{w}$ for solar minimum configurations with opposite polarities (CR1766, CR1908) and in both cases the flow was poleward. The magnitude of $\mathbf{w}_\phi$ is negligible compared to the magnitude of $\mathbf{w}_\theta$ in the case of solar minimum, and the magnitude of both components is very large close to the current sheet, due to the strong gradient in this region (as a result of the change in the sign of the magnetic field). However, in the Fisk model, reconnection does not occur in the current sheet, therefore, this region does not contribute to $\mathbf{w}$. In our simulation, although the magnitude of $\mathbf{w}$ in these regions is high, it always appears in pairs of positive and negative velocity in a relatively small area. As a result, the net effect of $\mathbf{w}$ is canceled in these regions, and we expect to see a significant effect only in large-scale regions with a preferred direction of $\mathbf{w}$.

In the case of solar maximum, the gradient of κ is isotropic and there are opposite components of $\mathbf{w}$ in most regions, so we expect the net effect of the reconnection processes to be smaller.

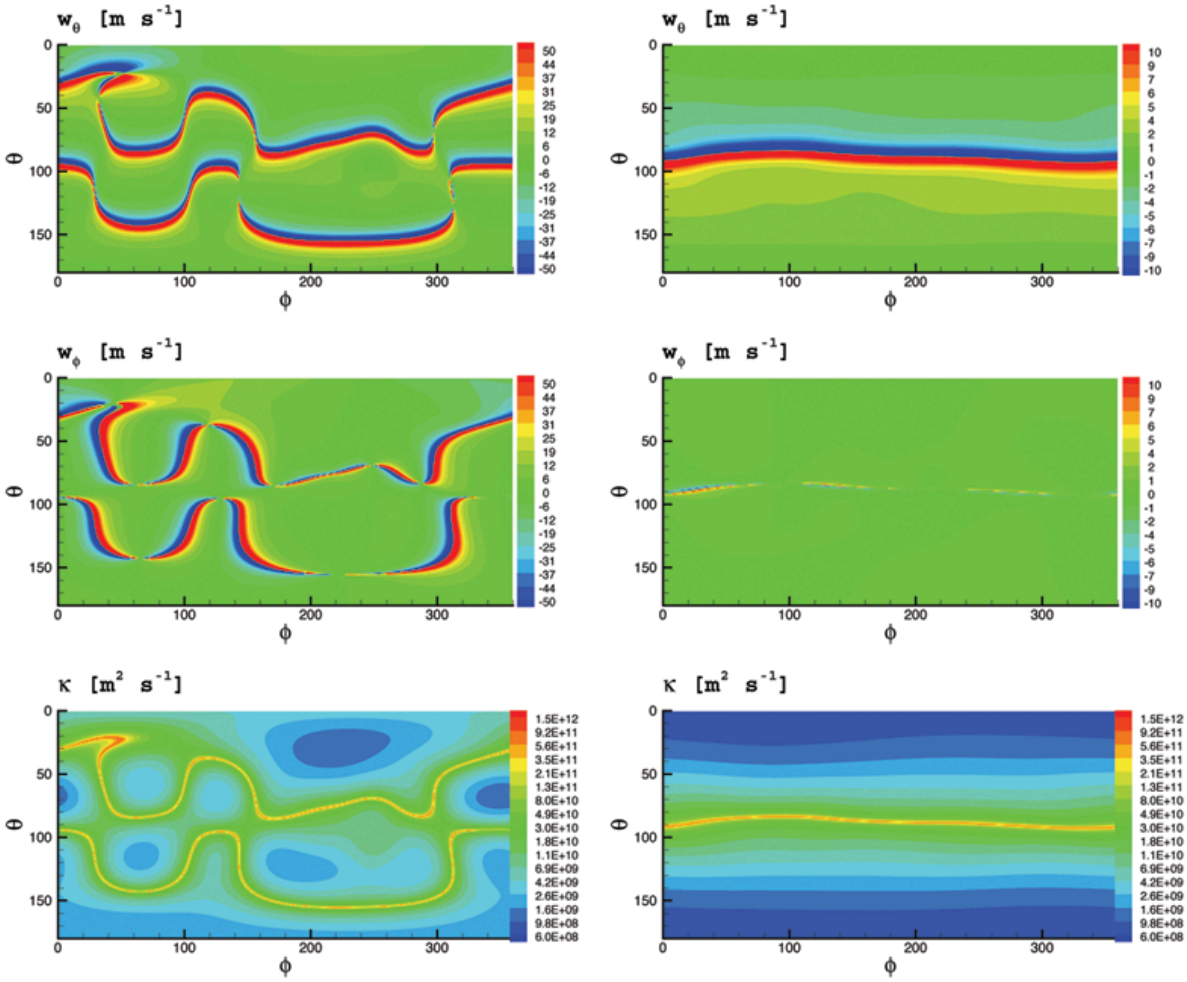

Figure 3.2: Meridional (top) and Azimuthal (middle) components of **w** and κ (bottom) for initial distribution of solar maximum (left) and solar minimum (right).

3.3.1 Solar Minimum Case

Figure 3.3 shows the steady state solution for solar minimum case. A steady state is achieved when the poleward motion is balanced by the equatorward diffusion, which is dominated by the uniform diffusive motion of the field line footpoints in the network lanes. For the case of uniform diffusion, a steady state is achieved after about 2 years (about 30 CR), and the "Coronal holes boundary" is located at about 50 degrees from the poles. In the case of non-uniform diffusion a steady state is achieved after 2.5 years (about 45 CR) and the boundary moves poleward to about 35 degrees from the poles.

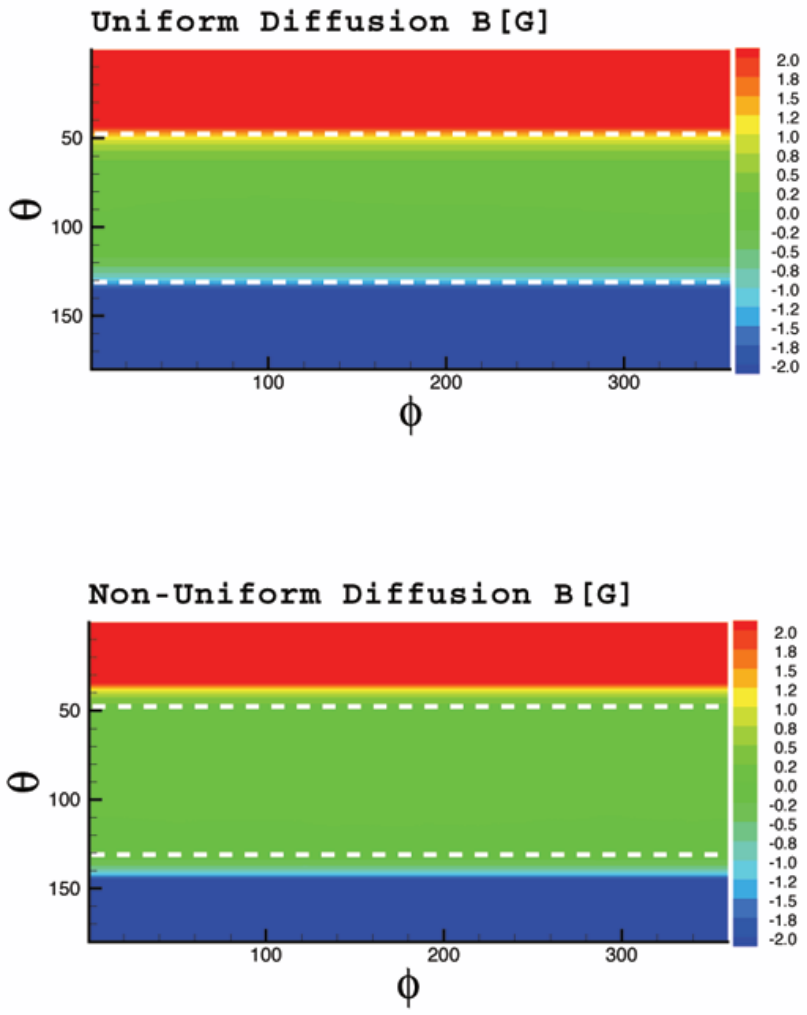

Figure 3.3: Steady-state solution for solar minimum conditions with uniform diffusion (top) and with non-uniform diffusion (bottom). The white dashed line marks the location of the boundaries of the coronal holes for the case of uniform diffusion.

Figure 3.4 shows the distribution of the magnetic field for the initial conditions and for the steady state with uniform and non-uniform diffusion coefficient at $\phi = 180°$. We found that in the solar minimum steady state solution, the meridional motion is enhanced by the magnetic reconnection processes. The enhancement is due to a large-scale preferred direction in the gradient of κ and in $\mathbf{w}_\theta$. During solar minimum conditions, the solar magnetic field is organized in a dipolar shape with two separate regions of open and closed magnetic field lines. Each of these regions has a typical rate of emergence of loops on the solar surface so the spatial change in the rate of emergence of loops is also directed poleward. All of the above lead us to the conclusion that the effect of diffusion due to reconnection processes is significant in a structured configuration of the solar magnetic field. This is mainly due to the fact that all the parameters, which control the behavior of the reconnection diffusion, in particular the rate of emergence of loops, have different characteristics in regions of open and closed magnetic field lines.

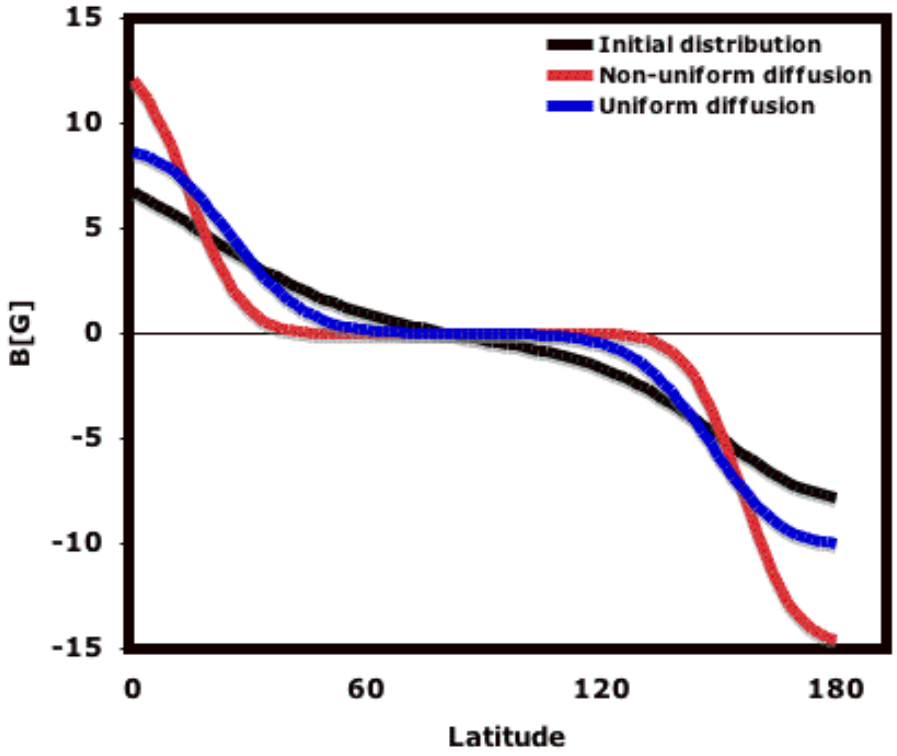

Figure 3.4: A latitudinal cut at $\phi = 180°$ for the solar minimum case at steady state. The black line represents the initial state, the blue line represents the steady state solution with uniform diffusion, and the red line represents the steady state solution with non-uniform diffusion.

Since the meridional component of $\mathbf{w}$ depends on B_l, variations from cycle to cycle in the rate of emergence of new flux can cause changes in the solar surface meridional transport. As mentioned in Section I, it has been suggested that variations in the solar surface meridional flow can explain the variations in the solar cycle. Our simulation showed that reconnection of open field lines with closed loops is an effective mechanism to modify the meridional flow.

3.3.2 Solar Maximum Case

Figure 3.5 shows the steady state solution for solar maximum conditions with uniform diffusion due to footpoints motion in the network lanes, and non-uniform diffusion, which also includes the effect of reconnection. It can be seen that the steady state solutions for the cases of uniform and non-uniform diffusion are very similar. The reason that the two cases are almost the same can be found in Fig 3.2. In the solar maximum configuration the solar magnetic field is unstructured. The gradient in κ is isotropic and, as a result, there is no preferred enhancement in the background flow. Solar maximum configuration results in local enhancements of the background flow. However, these local enhancements appear in pairs of opposite velocities so the large-scale net increase is very small.

Our simulation shows that the effect of diffusion due to magnetic reconnection is significant for the case of structured magnetic configuration (solar minimum conditions) and is small for the case of unstructured magnetic configuration (solar maximum conditions).

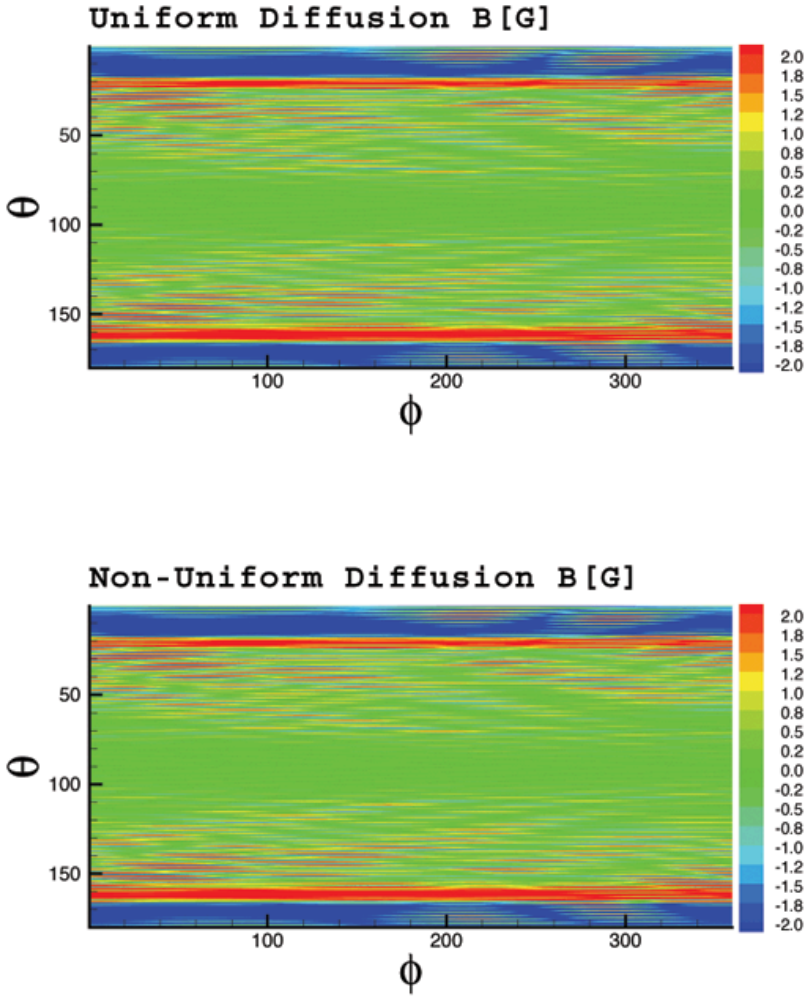

Figure 3.5: Steady-state solution for solar maximum conditions with uniform diffusion (top) and with non-uniform diffusion (bottom).

3.4 Discussion on the Flux-transport Model

We investigated the temporal evolution of the photospheric open magnetic flux for solar minimum configuration and solar maximum configuration. The study included the effect of diffusion of the open field lines due to magnetic reconnection, in addition to field line footpoints diffusion in the network lane and advective motion. Our two-dimensional simulation demonstrates that magnetic reconnection processes between open field lines and closed loops plays an important role in the transport of the open magnetic flux on the photosphere. We found that the effect of magnetic reconnection is significant for solar minimum conditions, but small for solar maximum conditions. In addition, we found that during solar minimum conditions, the flow is enhanced mainly poleward. Therefore, the effect of reconnection of open field lines with closed loops can be an effective mechanism to modify the solar surface meridional transport of the open flux and cause variations over the solar cycle. [15] found that large observed magnetic features tends to diffuse faster than small magnetic features. This is consistent with the idea that the displacement of an open field line as a result of reconnection is dependent on the size of the reconnected loop; in other words, the larger the loop, the larger the displacement. [91] mention that meridional flow is stronger in regions where the flux butterflies are steepest, which is consistent with the flow dependence on the spatial gradient of the emerging flux. Our simulation also demonstrates the importance of the large-scale effects and may raise the following question: Since all estimates of meridional flow result in an average flow pattern, is it possible that all the meridional motions are actually the same large-scale average motions due to the random walk of footpoints and the random magnetic reconnection events? If this is the case, then photospheric flux-transport models should be focused

more on the investigation of random motions on the photosphere. Since equatorward flow in the deep Sun, which is required due to mass conservation considerations, has not been observed yet, it may be helpful to investigate the problem in terms of magnetic diffusion and random behavior of the deep Sun magnetic fields.

Our simulation [18] shows the complexity of the solar magnetic field, and gives us physical insight into the importance of the convection zone, and the solar corona, as a single coupled system. We demonstrated that the distribution of the rate of emergence of flux on the photosphere can control the magnitude of the meridional flow and affect the variations from one solar cycle to another. However, the distribution of new emerging flux is dependent on internal processes, which can determine the variations, and these processes are not fully understood.

CHAPTER IV

Simulation of a Sun-to-Earth Space Weather Event

"The sea was angry that day, my friends, like an old man trying to send back soup in a deli."

George Costanza

The importance of space weather forecasting has become increasingly evident in recent years. The major March, 1989 Quebec blackout, demonstrated the potential hazard in such a phenomenon [12]. In order to predict the impact of a space weather event, we need to know the solar wind conditions in the vicinity of the Earth. Currently, the only source of real-time available data are the solar wind parameters measured by satellites far from the Sun. Such data provide a forecasting time of about an hour before the actual geoeffective impact takes place [36]. In order to extend our forecasting time, we need a tool, that can predict the solar wind conditions close to the Earth within a time frame that is significantly shorter than the CME travel time from the Sun to the Earth.

Solar, Heliospheric and INterplanetary Environment (SHINE), is a National Science Foundation (NSF) supported scientific community for solar and heliospheric physics exploration. Among its activities, the SHINE community has chosen several campaign events for the purpose of studying CME events from Sun to the Earth.

The May 12, 1997 CME event is one of these campaign events. This particular SHINE campaign event had been chosen, because it is separated in time from other CME events and it occurred during solar minimum [9, 78, 96, 54, 4, 58, 64, 112, 49, 76, 77, 41, 46]. Nevertheless, some particular features of this event are difficult to reproduce in numerical simulations, because the description of the solar wind for solar minimum is not accurate enough. In this work, we use the SWMF to simulate the May 12, 1997 CME event from Sun to the Earth in order to validate the physical correctness of the models adopted in the framework.

Previous work has been done to simulate a CME's propagation into the interplanetary space using the observed conditions of the ambient solar wind and the CME properties (Wu et al. 1996, Groth et al. 2000, Vandas et al. 2002, Manchester et al. 2004, Odstrcil et al. 2004 [113, 42, 105, 63, 70]). These simulations were driven by pre-specifying the observed values in to the inner boundary conditions or by some arbitrary eruption from the Sun.

In this work (Cohen et al. 2008 [21]), we do not impose the solar corona observations as either initial or boundary conditions, but rather we constrain the self-consistent solution with the observed properties of both the ambient solar wind and the CME. After the background solar wind solution is obtained using the model described in Chapter II, we superimpose a semi-circular, out-of-equilibrium flux rope (based on Titov and Démoulin 1999 [97]) and propagate the resulting CME from the Sun to the Earth. We then compare the SC result with a series of LASCO white-light images, and the IH result with WIND observations. This way, the CME in the model is much more realistic, even though it is not obtained by a complete physics-based mechanism.

This is the first simulation of real Sun-to-Earth CME event with realistic input

parameters. This simulation is part of the effort to develope real-time space weather forecasting system.

4.1 Simulation of the May 12, 1997 event

In order to simulate the May 12, 1997 CME event, we obtain the ambient solution for CR1922 using the solar corona model described in Section 2.4.2. It is important to note that while the WSA model is useful in practice, it only provides the solar wind speed and the magnetic field polarity at 1 AU. The MHD model, on the other hand, provides a three dimensional spatial distribution of the solar wind parameters everywhere, so that it is possible to investigate transient CME moving through the background solution. The main advantage of our ambient solar wind model is that we impose the empirical, observation based input model onto the self-consistent MHD solution.

We run the simulation on a Center for Space Environment Modeling (CSEM) local Mac cluster using 40 processors. The smallest grid cell size in the SC model is $dx = R_\odot/42$; the grid cell size at 1AU is $dx = 4R_\odot$, and it is finer in the heliospheric current sheet ($dx = 1R_\odot$). The steady-state solar corona solution is obtained within 10 hours of computing time, while the CME travel time of four days is simulated within three days of computing time.

Figure 4.1 shows a comparison of the steady-state simulation results with in-situ WIND observations at 1 AU for the period of time prior to the CME event. The density, temperature, and magnetic field differences between the model and data are less than a factor of two. The simulated speed of this particular period, however, is higher than that observed. We would like to note that we ran the ambient model for another Carrington Rotation (CR1958), which is near solar maximum, and the

agreement of the simulated speed with the observed one at 1 AU is significantly better in that case [19]. A possible reason for the difference in the quality of the results for solar minimum and solar maximum is discussed in Section 4.2 below.

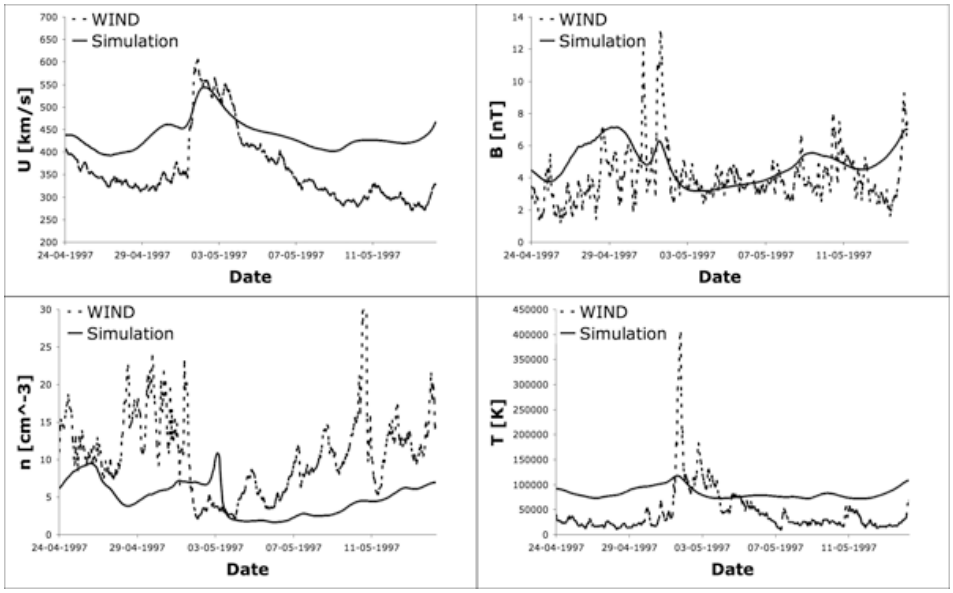

Figure 4.1: Simulation results (solid curve) and WIND data (dotted curve) for the ambient solar wind conditions of CR1922. Plots are shown for solar wind speed (top-left) magnetic field (top-right) number density (bottom-left) and temperature (bottom-right) respectively.

In order to model the CME eruption, we superimposed an out-of-equilibrium flux rope solution onto the steady-state SC model [82]. The flux rope location and orientation are chosen to match the magnetogram and EIT observations of AR 8038 during the eruption on May 12, 1997. Figure 4.2 shows the magnetogram of CR1922 with black arrow pointing to wards NOAA Active Region 8038.

The free energy released in the eruption depends on the ratio between the rope radius to the height of the loop above the surface (or the loop's radius), and on the magnitude of the toroidal current. We tune these parameters to match the observed CME properties taken from the SOHO LASCO CME catalog [115]. Figure 4.3 shows the flux rope embedded in the SC model in the vicinity of the active region.

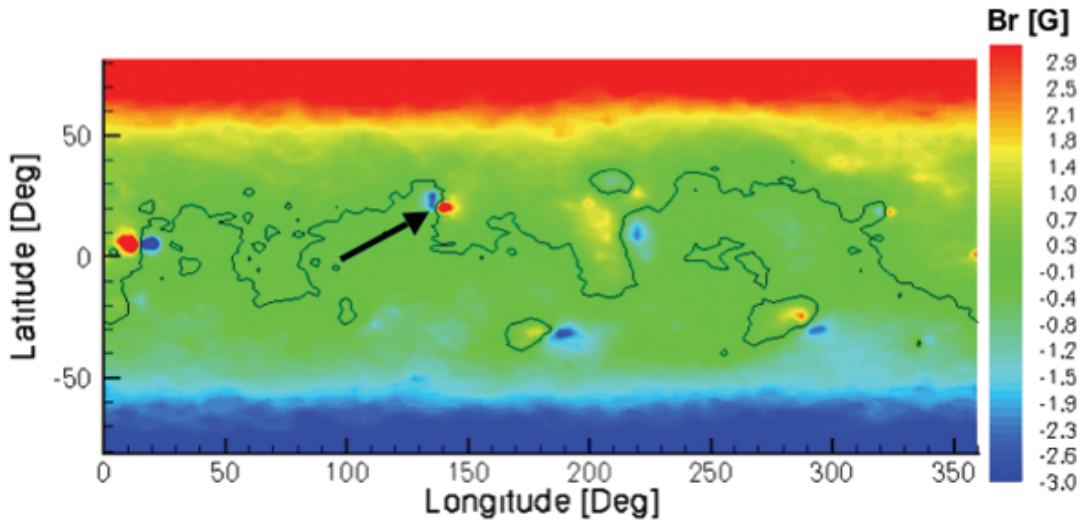

Figure 4.2: Magnetogram of Carrington Rotation 1922. NOAA Active Region 8038 is shown by the black arrow. The background color indicates the radial component of the magnetic field; red color represents positive polarity, whereas blue color shows the negative magnetic polarity. The black line represents the polarity inversion line.

Figure 4.4 shows the CME propagation in SC model after 10 hours, which is about the time the CME crosses the SC-IH boundary. This boundary is located at $17R_{\odot}$ and the total size of SC model is $24 \times 24R_{\odot}$. The CME front speed at this time is ≈ 650 km s^{-1}.

Figures 4.5 and 4.6 show a comparison of synthetic white-light images produced by our simulation and LASCO C2 and C3 images, respectively. Both artificial and real images are made of temporal running differences of integrated density images. Light color represent higher density region, while dark color represent low density region. The white arrows show similarities in the location of the CME front, while the yellow arrows mark similarities in the dark spots due to the streamer expansion.

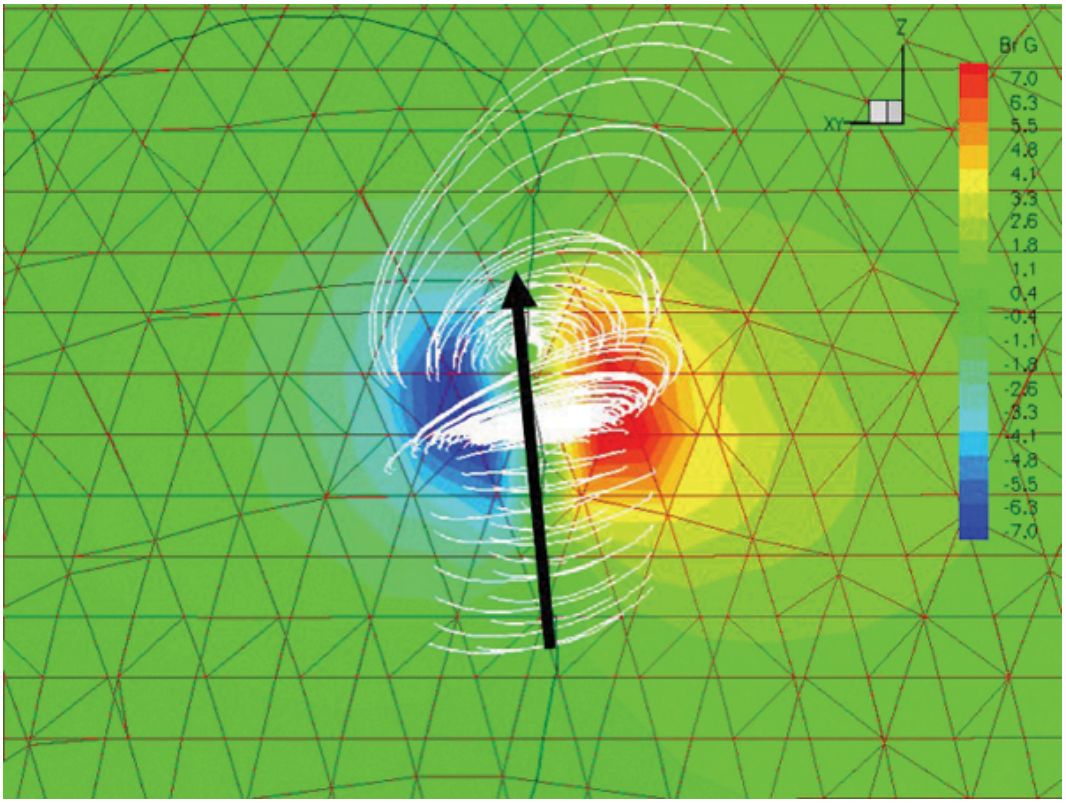

Figure 4.3: Zoom on the vicinity of the active region ($15°N < \theta < 30°N, 125° < \phi < 150°$). Color contours are the same as in Figure 4.2. White streamlines represent the magnetic field lines of the superimposed flux rope, black arrow represents the flux rope orientation, and red triangles represent the grid.

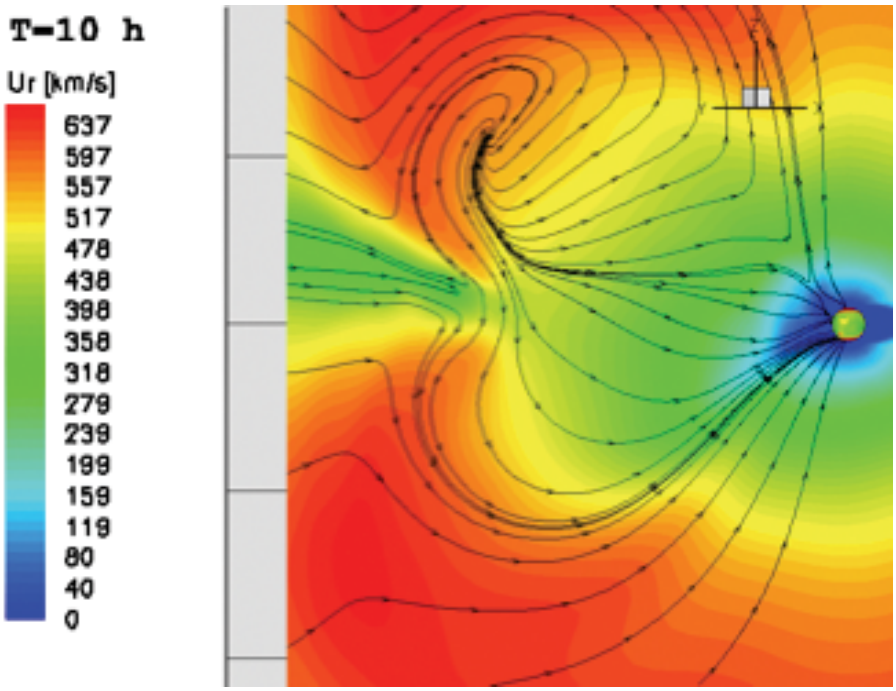

Figure 4.4: The CME propagation after 10 hours as it approaches the outer boundary of SC model, located at $24R_{\odot}$. Color contours represent flow speed and streamlines represent magnetic field lines.

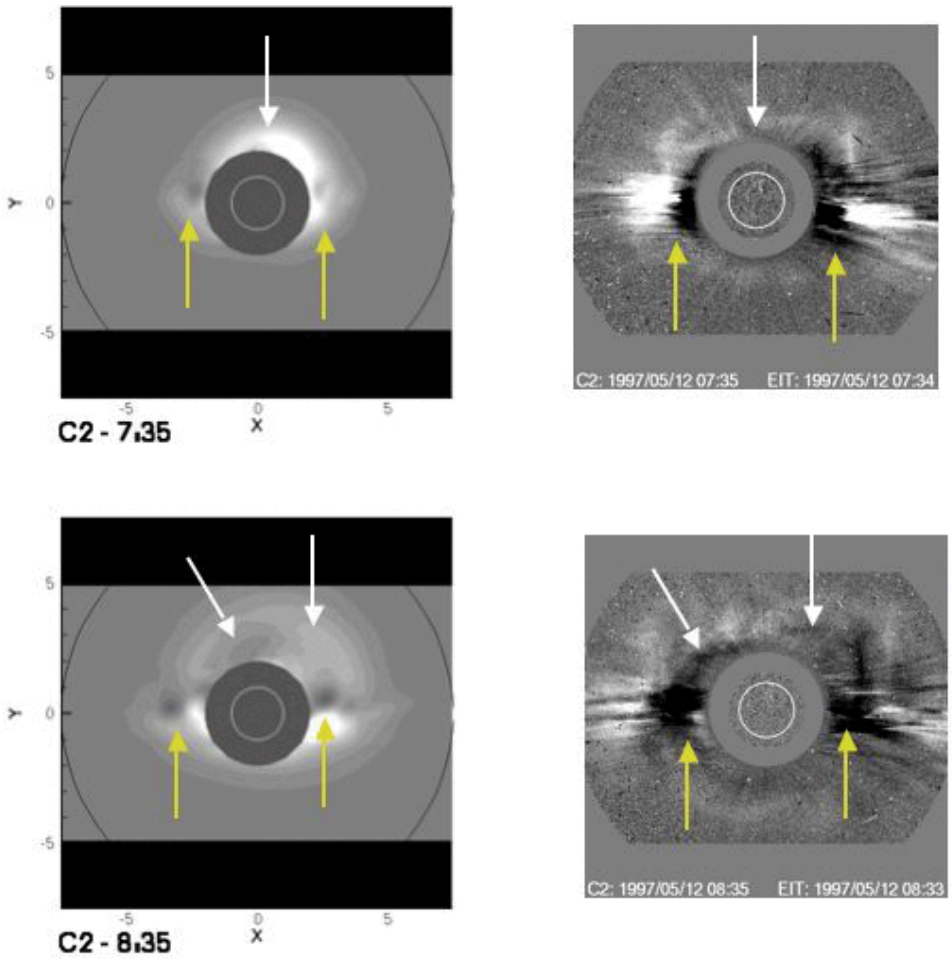

Figure 4.5: Synthetic white-light images produced by the simulation (left) and observed LASCO C2 white-light images (right) at $t = 7:35$ (top) and $t = 8:35$ (bottom).

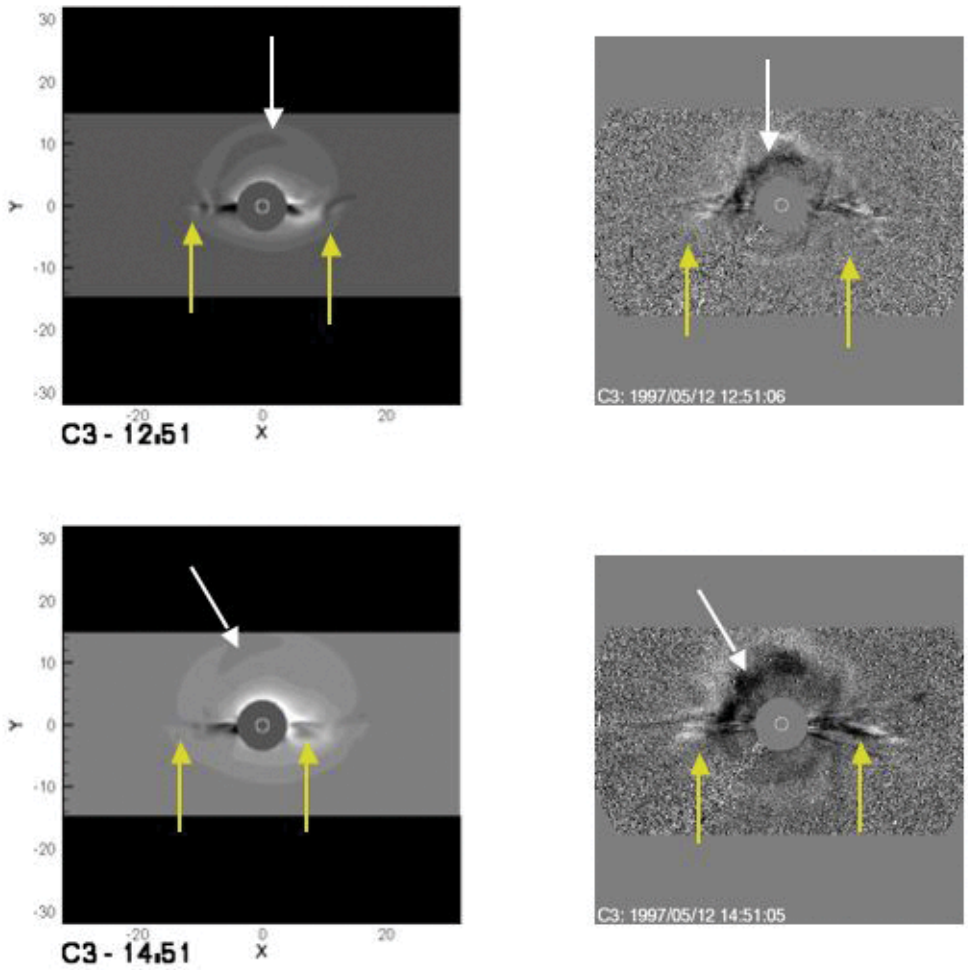

Figure 4.6: Synthetic white-light images produced by the simulation (left) and observed LASCO C3 white-light images (right) at $t = 12:51$ (top) and $t = 14:51$ (bottom).

Figure 4.7 shows comparison of the simulation result with WIND observations at 1 AU. The main difference is that the simulated CME speed is higher than the observed one, so that the simulated shock arrival time is earlier than observed arrival time. This is due to the fact that the speed in the ambient solar wind model was higher than observed. However, the magnitude of the density peak and the temperature peak match well the values observed at the shock.

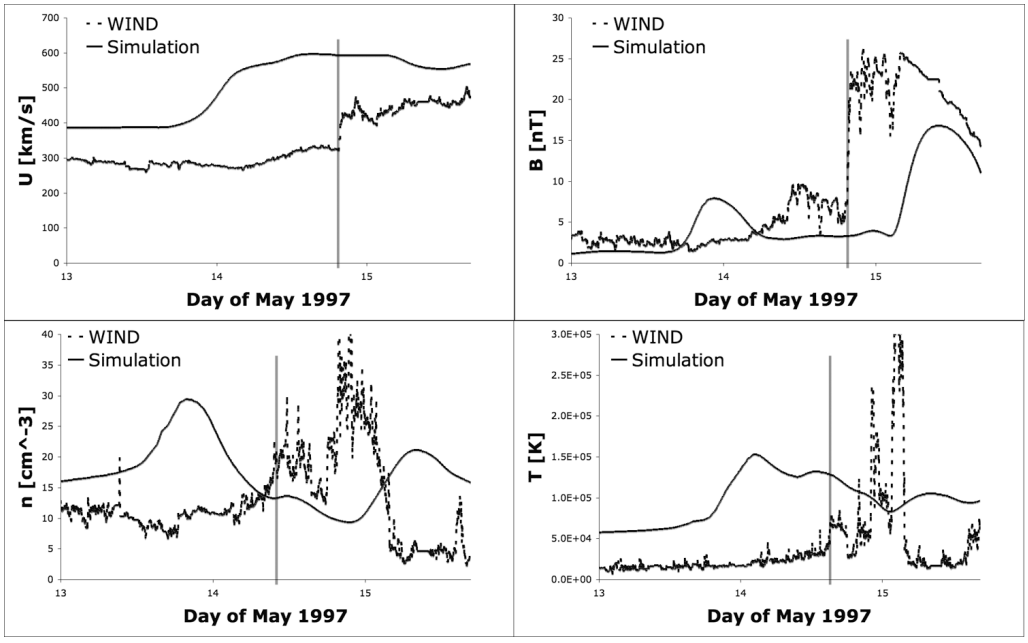

Figure 4.7: Simulation results (solid curve) and WIND data (dotted curve) for the May 12, 1997 CME event. Plots are shown for solar wind speed (top-left) magnetic field (top-right) number density (bottom-left) and temperature (bottom-right), respectively. The gray lines mark the actual shock arrival time.

4.2 Discussion of the Initial Results

We simulate the May 12 1997 space weather event from the Sun to 1 AU. It appears that the background solar wind conditions are not sufficiently reproduced in the simulation. To some extent,this is due to the WSA model, which does not well reproduce solar minimum conditions due to the sensitivity of spacecraft location with respect to the location of the current sheet [5]. For a CME as slow as $u \approx 600$ km s^{-1}, the extra advection due to the inaccurately simulated background solar wind (which is too fast, see Fig. 4.1), yields an early shock arrival (see Fig. 4.7). It seems that the flux rope should be resolved on a finer resolution so that its integrity can be maintained as it originates from a small scale active region. This way, the interaction of the eruptive flux rope with the surrounding magnetic flux will be more precise, and the properties of the magnetic cloud at 1 AU will be in better agreement with observations. With the current resolution of the active region, even the result for magnetic field magnitude at 1 AU is not in good agreement with the observed value. With better resolution of the active region, as well as the implementation of vector magnetogram data in our model, we expect to get better agreement for the field magnitude, as well as for the magnetic field components. An accurate reproduction of the magnetic field components, in particular B_z, reflects good resolution of the magnetic cloud propagation and integrity.

We demonstrate the effect of the background with the simulation results of a second event for which the modeled velocity agrees well with observations. Figures 4.8 and 4.9 show results for a simulation of the April 21, 2002 CME event, which occurred under solar maximum conditions. It is clear that the simulation results for both the background solar wind and for the event itself, in the case of the 2002 event,

are in better agreement with observations than the results for the 1997 event. The discrepancy in the shock arrival in the 2002 CME event is about 4 hours, while the discrepancy in the shock arrival in the 1997 CME event is more than 24 hours.

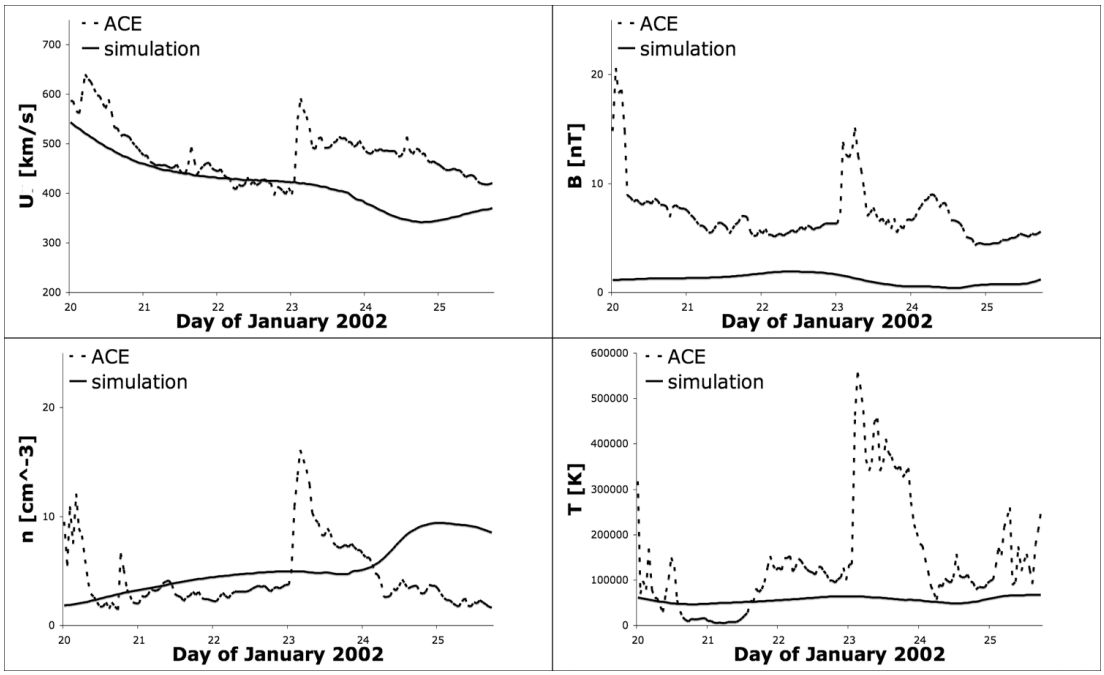

Figure 4.8: Simulation results (solid curve) and ACE data (dotted curve) for steady-state heliosphere driven by MDI magnetogram as of April 18, 2002. Plots are shown for solar wind speed (top-left) magnetic field (top-right) number density (bottom-left) and temperature (bottom-right) respectively.

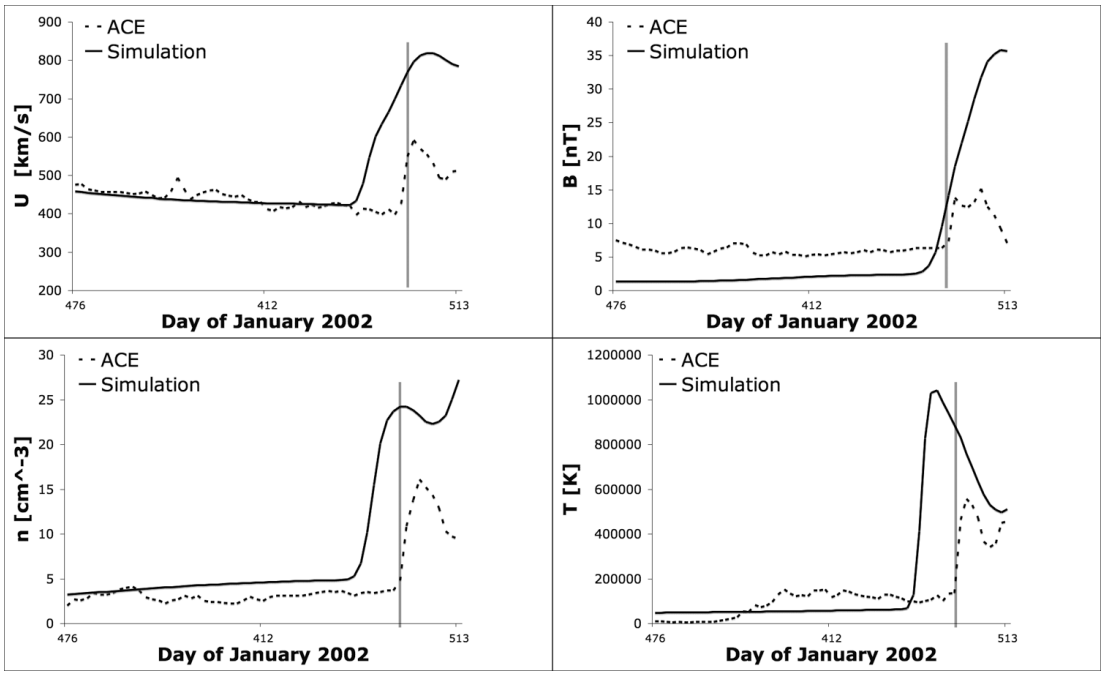

Figure 4.9: Simulation results (solid curve) and ACE data (dotted curve) for the April 21, 2002 CME event. Plots are shown for solar wind speed (top-left) magnetic field (top-right) number density (bottom-left) and temperature (bottom-right), respectively. The gray lines mark the actual shock arrival time.

4.3 Improved Simulation

In order to obtain a better solution for our simulation, we modified its setup as follow. First, we implemented the Roe solver to the SC model (see section B). This modification enables us to obtain a more accurate solution for the ambient solar wind. In particular, this solver provides a better numerical solution for the heliospheric current sheet, which appears as V shape lines in the previous simulation due to over-reconnection. The Roe solver also resolves better the vicinity of the flux-rope and prevents it from over-reconnecting with the ambient field. Figure 4.10 shows a comparison of the ambient solar wind model and WIND observations at 1 AU three days prior to the CME arrival. One can see that this comparison is better than the one in Figure 4.1.

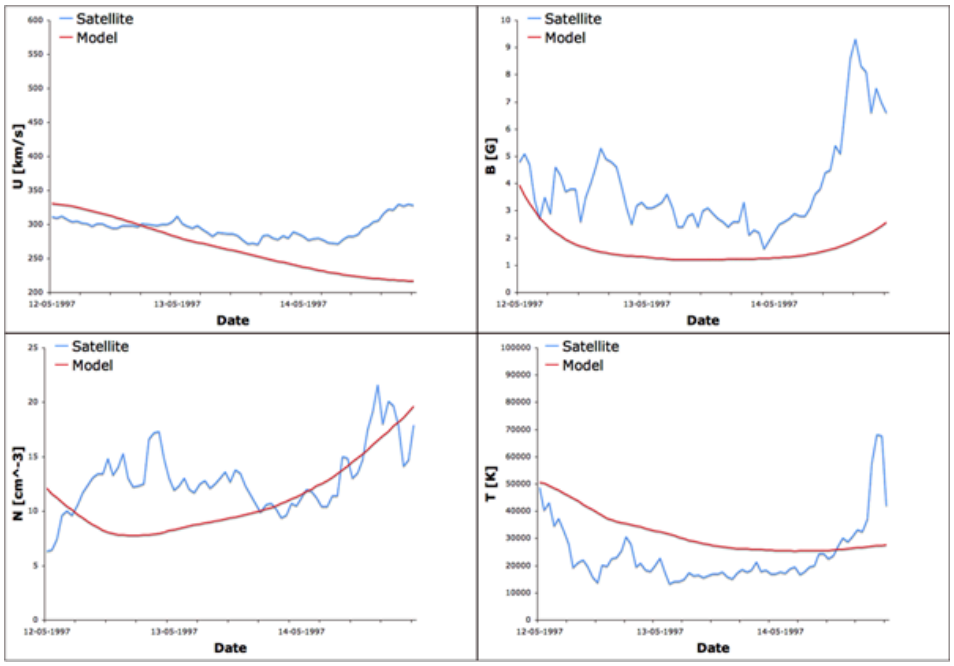

Figure 4.10: A comparison of the steady state simulation results (red line) with WIND data (blue line) for Solar wind radial speed (top left), magnetic field (top right), number density (bottom left), and temperature (bottom right) three days prior to the CME arrival.

Figures 4.11 and 4.12 show a comparison of the artificial white-light images pro-

duced by the simulation with LASCO white-light images for C2 and C3, respectively. It can be seen that the location of the CME front matches in both cases, as well as the general structure in the C2 case. In C3 however, the simulated CME seemed to be flatenned. This might be due to reconnection with the ambient magnetic field. In any case, the location and width of the CME matches rather well to the observed line-of-sight images. This indicates that the coronal density in the model based on the Roe solver is well reproduced.

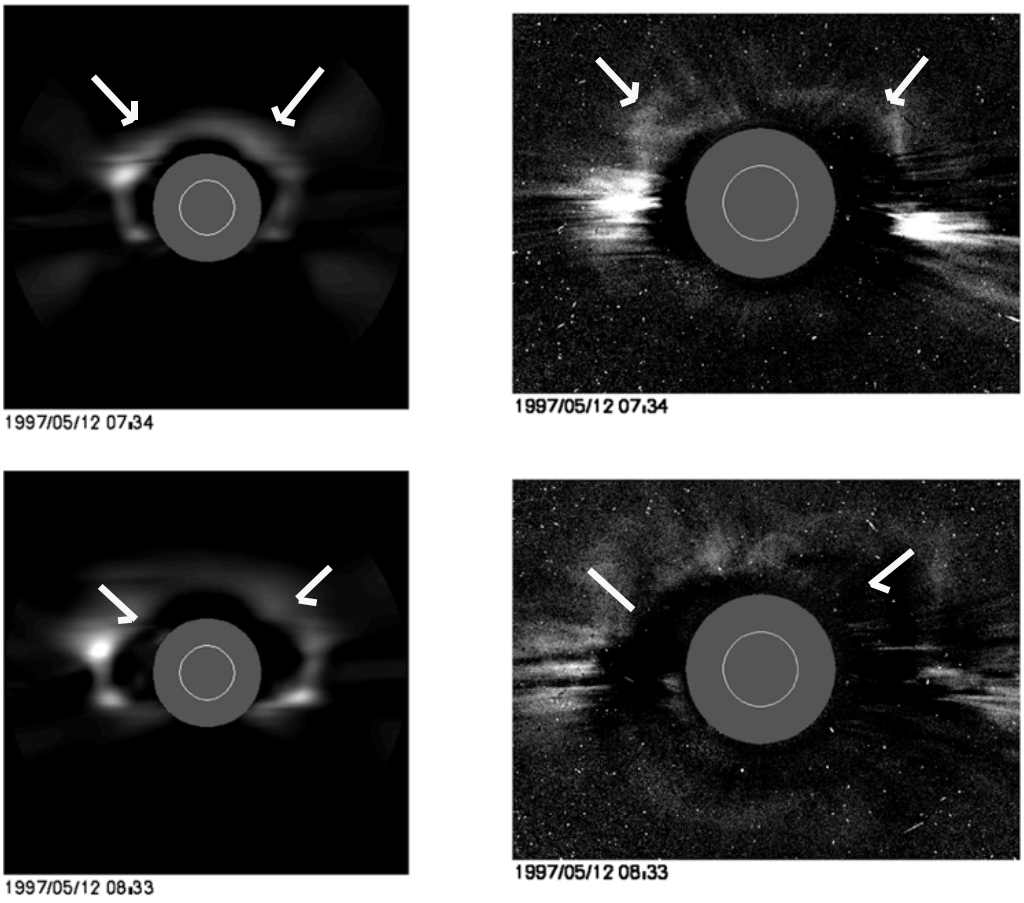

Figure 4.11: Synthetic white-light images produced by the simulation (left) and observed LASCO C2 white-light images (right) at $t = 7:34$ (top) and $t = 8:33$ (bottom). White arrows mark the CME front.

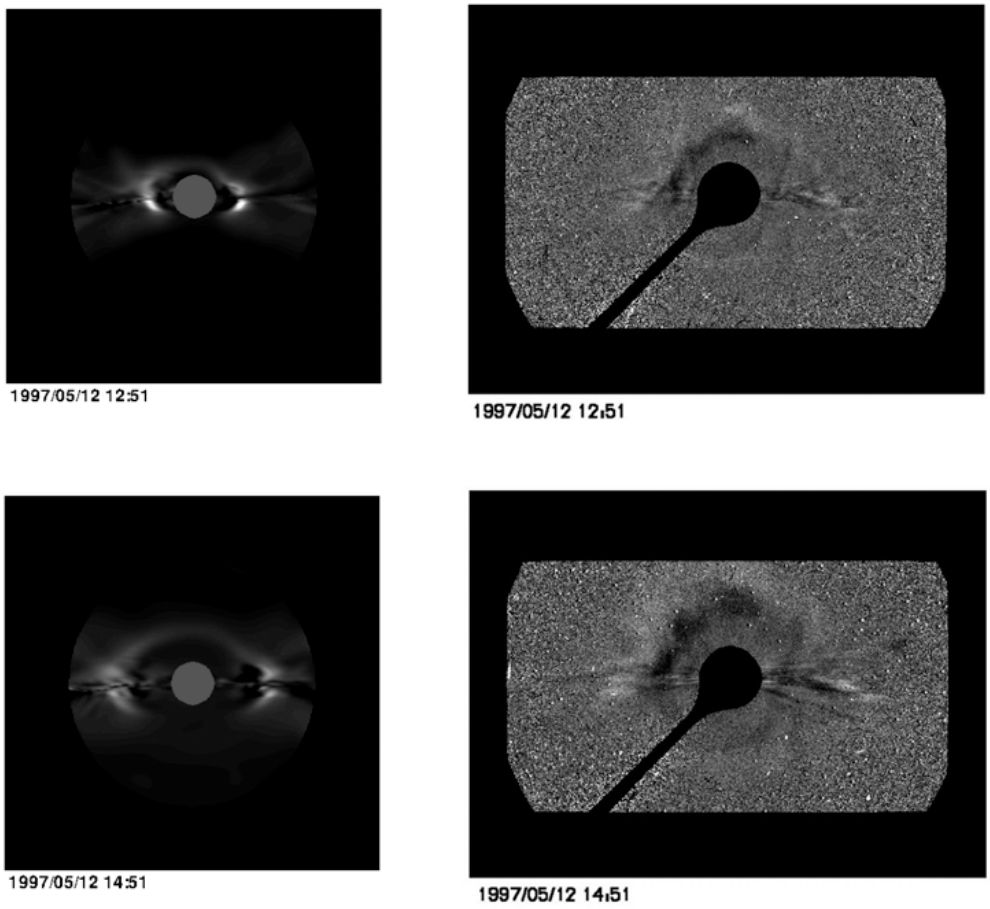

Figure 4.12: Synthetic white-light images produced by the simulation (left) and observed LASCO C3 white-light images (right) at $t = 12 : 51$ (top) and $t = 14 : 51$ (bottom). The orientation of the CME seems to be twisted by 90 degrees due to interaction with the ambient magnetic field.

Figure 4.13 shows the CME in the corona after 10h of simulation time from the top, side and front. Color contours represent the solar wind speed, while iso-surface represent a density ratio of 4 between the current and initial density.

Figure 4.14 shows a comparison of the simulation result with WIND data at 1AU. This time the shock arrival time matches much better the observed arrival time compared to the first simulation, where the shock appears one day earlier. The density jump is of about 4 as it should be. However, the magnitude of the magnetic field is too low since the flux-rope diffuses away as it reaches 1 AU.

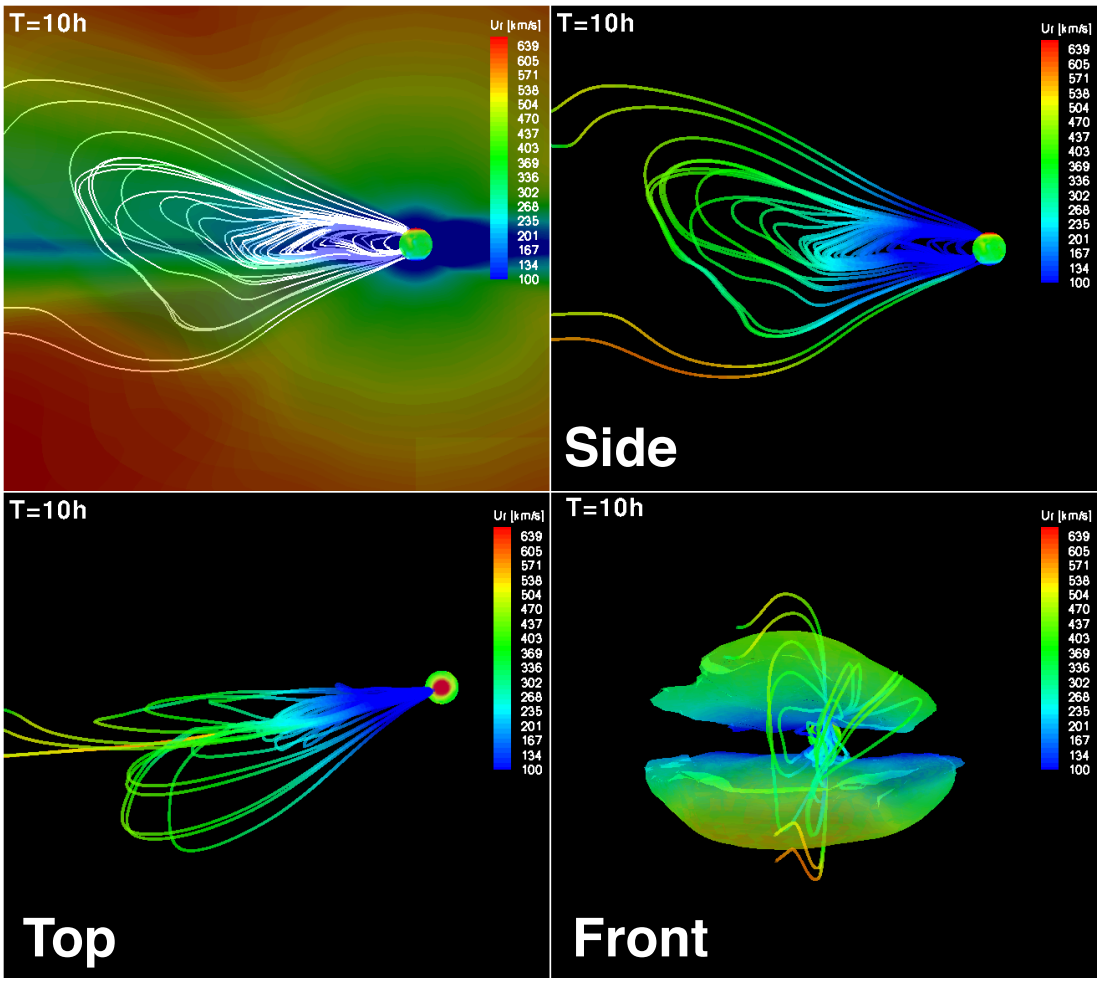

Figure 4.13: The CME in the corona after 10h of simulation time from the top, side and front. Color contours represent the solar wind speed, while iso-surface represent a density ratio of 4 between the current and initial density.

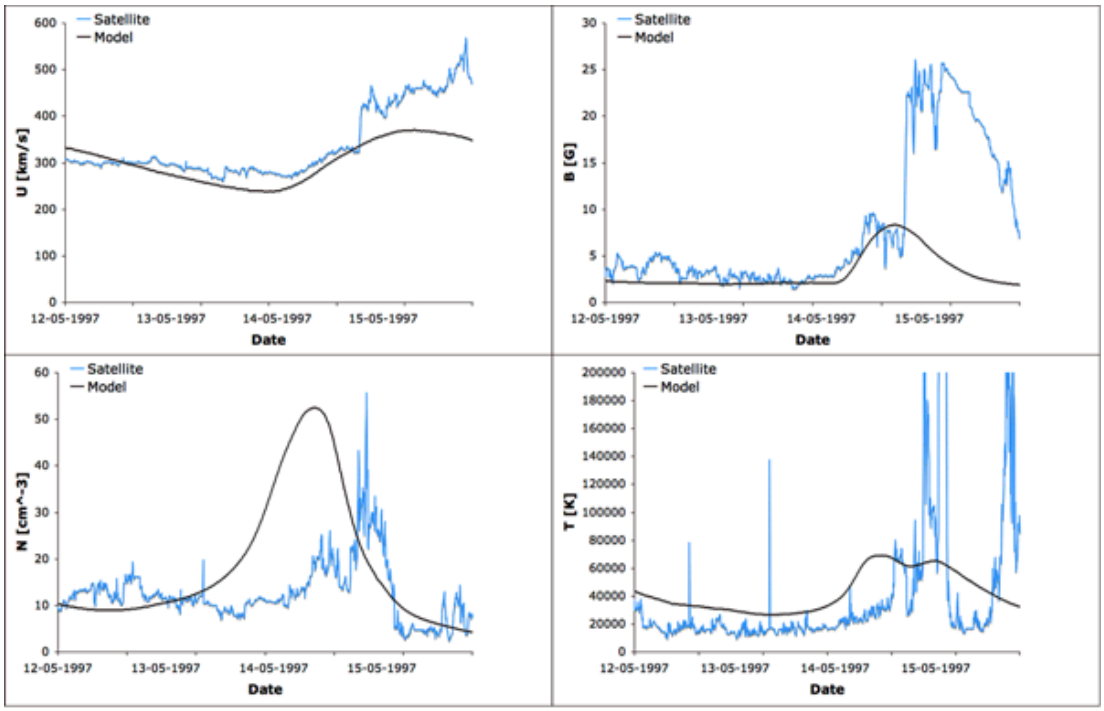

Figure 4.14: A comparison of the simulation results (black line) with WIND data (blue line) for Solar wind radial speed (top left), magnetic field (top right), number density (bottom left), and temperature (bottom right), respectively. The gray lines mark the actual shock arrival time.

4.4 Conclusions for the Simulation of a CME Event

Following this simulation, we arrive at two main conclusions. First, our simulation demonstrates how crucial the model's ambient solar wind conditions are and how they affect the accuracy of the CME propagation. This is especially true for CMEs whose speed and magnetic field strength are of the same order as those in the background solar wind, such as the event simulated in this paper. The chosen campaign event, which occurred during solar minimum conditions, and was isolated in time from other CMEs, provides an excellent example to benchmark our computational models of the solar corona and inner heliosphere with real observations. We also conclude that the active region must be resolved highly resolved so the integrity of the flux rope can be maintained all the way to 1 AU.

Our second conclusion concerns the practical application of a simulation of a Sun-to-Earth space weather event. Our comparison demonstrates that the CME properties, which are required for the simulation's initial setup such as the free energy, density, origin, and orientation can be automatically obtained from the available magnetic field and white-light observations. The STEREO and HINODE missions should provide a wider range of data to be used for the simulation's initiation, including vector magnetograms and three dimensional observations of the CME.

This work represents a step forward in the development of real-time, automatic, space weather forecasting tools. Our future efforts will focus on improving the background solar wind model and the CME initiation model.

CHAPTER V

Conclusions and Future Work

5.1 Summary of this Work

In this work I present a series of numerical investigations of the solar corona. The work has three major parts:

- **Global MHD model for the solar corona and inner heliosphere:** I developed a global MHD model for the solar corona and for the inner heliosphere. This model provides the ambient condition for the solar wind and it has been validated with long-term satellite data.

- **Flux-transport model for the open magnetic flux of the Sun:** I developed a flux-transport model for the photosphere in order to study the effect of magnetic reconnection on the transport of the Sun's open magnetic flux. This simulation showed that this process is important and can modify the magnitude of the surface meridional flow, which controls the magnitude of the particular solar cycle.

- **Numerical Simulation of a Sun-to-Earth CME Event:** I performed a numerical simulation of the May 12, 1997 CME event from the Sun to the Earth. This simulation demonstrated how the SWMF can be used for the operational

purposes of space weather forecasting. This simulation also addressed the issues and problems expected in the process in order to improve it in the future.

The main conclusion of this work is that numerical tools nowdays really get to the point where they can be used to solve big and complex physical problems. The physical system of the solar corona is an excellent example of such system and our simulations have demonstrated how does this system can be better understood using computer models. We can expect that the benefits of numerical models will grow due to the growth of our computation capabilities.

5.2 Future Work

Following the conclusions of this work, I have three main suggestions. First, we should develop a global model for the solar corona, which contains a self-consistent heating mechanism. This will remove a major part of the constrains from the current model and should improve it. Second, I propose to further investigate the role of the open flux in the long-term evolution of the solar and heliospheric magnetic field. In particular, I believe in the necessity of a coupled model of the convection zone and the solar corona. Third, I propose to investigate the behavior of other stars in the context of our Sun in order to learn more about its behavior and evolution.

At this point, when I am completing my PhD, I am happy to know that there are plenty of open questions in the field of Space and Solar Physics, which guarantee many years of fun!!!

APPENDICES

APPENDIX A

Physical Constants and Notation

Notation:

ρ - mass density	n - number density
u - velocity	p - pressure
B - magnetic field	E - electric field
j - current density	T - temperature
σ - conductivity	μ - permeability
ε - permittivity	$\odot$ - solar parameters

Physical Constants:

Boltzmann constant:	$k = 1.3807 \times 10^{-23}\ J\ K^{-1}$
Elementary charge:	$e = 1.6022 \times 10^{-19}\ C$
Electron mass:	$m_e = 9.1094 \times 10^{-31}\ kg$
Proton mass:	$m_p = 1.6726 \times 10^{-27}\ kg$
Gravitational constant:	$G = 6.6726 \times 10^{-11}\ m^3\ s^{-2}\ kg^{-1}$
Speed of light in vacum:	$c = 2.9979 \times 10^{8}\ m\ s^{-1}$
permeability of free space:	$\mu_0 = 4\pi \times 10^{-7}\ H\ m^{-1}$
permittivity of free space:	$\varepsilon_0 = 8.8542 \times 10^{-12}\ F\ m^{-1}$
Plank constant:	$h = 6.6261 \times 10^{-34}\ J\ s$
Stephan-Boltzmann constant	$\sigma = 5.67051 \times 10^{-8}\ W\ m^{-2}\ s^{-1}\ K^{-4}$

APPENDIX B

The Roe Solver

An alternative approach to the eight-wave scheme is introduced in a recent paper by Sokolov et al. [92] and is implemented as well in BATS-R-US . The $\nabla \cdot \mathbf{B} = 0$ condition requires the continuity of the magnetic field normal component, B_n, through any surface. If a discontinuity appears in B_n across the face of the control volume, the RP for the MHD equations is ill-posed. However, if B_n is continuous, then the initial jumps in seven other MHD variables determine seven amplitudes of the CWs and the RP is well-posed. This approach differs from the eight wave scheme in the sense that in the eight wave method, an extra CW is added, while in this approach one of the jump conditions is eliminated by maintaining, B_n contineous across the face.

The general conservation law is introduced in the form:

$$\frac{\partial \mathbf{U}}{\partial t} + \nabla \cdot \mathbf{F} = 0. \tag{B.1}$$

The approach proposed by Godunov [38] and implemented in the eight wave scheme introduces the source term proportional to $\nabla \cdot \mathbf{B}$:

$$\frac{\partial \mathbf{U}}{\partial t} + \nabla \cdot \mathbf{F} + \mathbf{G}\,(\nabla \cdot \mathbf{B}) = 0\,. \tag{B.2}$$

The conserved variables, $\mathbf{U}$, and their fluxes, $\mathbf{F}$, are (with the notation for inner product, $\otimes$):

$$\mathbf{F}(\mathbf{W}) = \mathbf{u} \otimes \mathbf{U} + p_{tot}\,(0, \mathbf{I}, 0, \mathbf{u})^T - \mathbf{B} \otimes \mathbf{G}(\mathbf{W})\,, \tag{B.3}$$

$$\mathbf{W} = (\rho, \mathbf{u}, \mathbf{B}, p)^T\ ,\ \mathbf{U}(\mathbf{W}) = (\rho, \rho\mathbf{u}, \mathbf{B}, E)^T\ ,\ \mathbf{G}(\mathbf{W}) = (0, \mathbf{B}, \mathbf{u}, \mathbf{u}\cdot\mathbf{B})^T\ , \tag{B.4}$$

$$E = \frac{\rho u^2}{2} + \frac{B^2}{2} + \frac{P}{\gamma - 1}\,,\ p_{tot} = p + \frac{B^2}{2}. \tag{B.5}$$

Godunov [38] showed that as $\nabla\cdot\mathbf{B} = 0$ holds, Eqs.(B.1) and (B.2) have coinciding solutions, but their quasi-linear formulations differ. The advantage of Eq.(B.2) is that its Jacobian is non-degenerated.

For the Godunov-like scheme the Jacobian need not be, but the numerical flux must be, the basic element. Thus, to benefit from the idea of the Jacobian modification, it should be applied to the numerical flux. For Eq.(B.1) the finite volume formulation reads: $\mathbf{U}_i(t+\Delta t) - \mathbf{U}_i(t) = -(\Delta t/V_i)\sum_j \sigma_{ij}(\mathbf{F}_n)_{ij}$, where Δt is the time step, the index j enumerates the neighbors of the control volume, V_i, $\sigma_{ij}\mathbf{n}_{ij}$ is a face area vector, $(\mathbf{F}_n)_{ij}$ is the numerical flux, subscript i, j, ij denote the variables in the correspondent control volume or at the face between them, and subscript n denotes the dot product by the unity vector, $\mathbf{n}_{ij}$, normal to the face: $\mathbf{F}_n = \mathbf{n}_{ij}\cdot\mathbf{F}$, $B_n = \mathbf{n}_{ij}\cdot\mathbf{B}$ etc. Assume that a discretization for $\nabla\cdot\mathbf{B}$ in terms of the face values of B_n,

$$(\nabla\cdot\mathbf{B})_i = \frac{1}{V_i}\sum_j \sigma_{ij}(B_n)_{ij}\,, \tag{B.6}$$

turns to zero. In this case the SDTB added to the finite volume formulation:

$$\mathbf{U}_i(t+\Delta t) - \mathbf{U}_i(t) = -\frac{\Delta t}{V_i}\sum_j \sigma_{ij}(\mathbf{F}_n)_{ij} - \Delta t\mathbf{G}_i\,(\nabla\cdot\mathbf{B})_i\ , \tag{B.7}$$

modifies the numerical fluxes: $(\mathbf{F}_n)_{ij} \rightarrow (\mathbf{F}_n)_{ij} + (B_n)_{ij}\mathbf{G}_i$, but not their total. Now we can reduce constructing the numerical scheme for the total of the numerical flux and source term proportional to $\nabla \cdot \mathbf{B}$ to the well-posed RP.

To analyze Eq.(B.7), it is re-written using the entity, $(\sum_j \sigma_{ij}\mathbf{n}_{ij}) \cdot (\mathbf{F}_i + \mathbf{B}_i \otimes \mathbf{G}_i) = 0$:

$$\mathbf{U}_i(t+\Delta t) - \mathbf{U}_i(t) = -\frac{\Delta t}{V_i} \sum_j \sigma_{ij} \left[(\mathbf{F}_n)_{ij} + B_{nf}\mathbf{G}_i - (\mathbf{F}_n)_i - (B_n)_i \mathbf{G}_i \right]. \tag{B.8}$$

The following equation holds for the total of the flux and the STDB in Eq.(B.8):

$$(\mathbf{F}_n)_i - \mathbf{G}_i \left[B_{nf} - (B_n)_i \right] = \widetilde{\mathbf{F}}_n(\widetilde{\mathbf{W}}_i) - (u_n)_i \left[B_{nf} - (B_n)_i \right] \mathbf{U}_8^{(R)}, \tag{B.9}$$

where $\mathbf{U}_8^{(R)} = (0, 0, \mathbf{n}_{ij}, B_{nf})^T$ is one of the right eigenvectors of the Jacobian of Eq.(B.2). In the modified set of primitive variables, $\widetilde{\mathbf{W}}_i = \mathbf{W}_i + (0, 0, [B_{nf} - (B_n)_i]\mathbf{n}_{ij}, 0)^T$, $(B_n)_i$ is substituted for the value at face, $B_{nf} = (B_n)_{ij}$. Thus, by applying Eq.(B.9) to the state i and j one achieves the *continuity* in B_n across the face ij.

An Extra Magnetic Pressure (EMP), P_M, is involved in the modified flux, $\widetilde{\mathbf{F}}_n$: $\widetilde{E}_i = E_i + (P_M)_i$, $(\widetilde{P}_{tot})_i = (P_{tot})_i + (P_M)_i$, $(P_M)_i = \left[B_{nf} - (B_n)_i \right]^2 / 2$.

We choose $(B_n)_{ij}$ to be an arithmetic average of the cell-centered values:

$$(B_n)_{ij} = \frac{1}{2} \left[(B_n)_i + (B_n)_j \right]. \tag{B.10}$$

Consider the explicit first order Godunov-like scheme according to Eq.(B.7). It is conservative as long as $(\nabla \cdot \mathbf{B})_i$ turns to zero. Using Eqs.(B.8)-(B.10), we obtain:

$$\mathbf{U}_i(t+\Delta t) - \mathbf{U}_i(t) = -\frac{\Delta t}{V_i} \sum_j \sigma_{ij} \left\{ (\mathbf{F}_n)_{ij} - (\widetilde{\mathbf{F}}_n)_i + \frac{(u_n)_i}{2} \left[(B_n)_j - (B_n)_i \right] \mathbf{U}_8^{(R)} \right\}.$$

The RS should be applied to handle the flux difference above. Note that the flux in the ith cell state comes in a modified form, with B_n equal to the face value

$(B_n)_{ij}$. Therefore, the left hand side initial condition in the RP will be at the same value of B_n. Repeating the same considerations for jth control volume, we find that the right hand side initial condition for the RP equals $\widetilde{\mathbf{W}}_j$, so that B_n is *continuous* through the face. The EMP is also continuous through the face: $(P_M)_i = (P_M)_j = \left[(B_n)_i - (B_n)_j\right]^2/8$. The RP is well-posed and the RS7, $\widetilde{\mathbf{F}}_n^{RS7}(\widetilde{\mathbf{W}}_i, \widetilde{\mathbf{W}}_j)$, gives a numerical flux. However, an extra diffusive flux proportional to $\mathbf{U}_8^{(R)}$ should be added to stabilize the residual part of the STDB. Finally the Godunov-like numerical flux in Eq.(B.7) is as follows:

$$(\mathbf{F}_n)_{ij} = \widetilde{\mathbf{F}}_n^{RS7}\left(\widetilde{\mathbf{W}}_i, \widetilde{\mathbf{W}}_j\right) + \frac{1}{2} D_8 \left[(B_n)_i - (B_n)_j\right] \mathbf{U}_8^{(R)} \,. \tag{B.11}$$

The following choice of the extra diffusion coefficient ensures the scheme monotonicity both for ith and for jth control volumes:

$$D_8 = \max\left[0\,,\, (u_n)_i\,,\, -(u_n)_j\right] \,. \tag{B.12}$$

A distinctive feature of the present approach is the use of the EMP. It is present in the conserved variables and fluxes (hence, in the governing equations for the RP) in the same manner as the magnetic pressure at parallel shocks. We assume that in the RS the EPM evolves in accordance with the same governingequation ($P_M \sim \rho^2$), which may be used in the form of a conservation law,

$$\frac{\partial (P_M/\rho)}{\partial t} + \nabla \cdot (\mathbf{u} P_M/\rho) = 0 \,. \tag{B.13}$$

The way to handle the EPM in the RS7 solver depends on the solver choice. Particularly, in the Godunov scheme with the exact RS one would need to solve Eq.(B.13) together with the MHD SCL. On the other hand, for a more simple HLL-type solver [43] the EMP modifies only the fluxes in the left and right states as well as the speed

of sound:

$$a^2 = \frac{\gamma P}{\rho} + \frac{2P_M}{\rho}\,, \tag{B.14}$$

which is to be used in calculating the maximum perturbation speed.

Figure B.1 illustrates the above approach. [94] mentioned that the numerical diffusion in the explicit Godunov-like scheme can be interpreted as the conservative averaging in the initial conditions in the RP. Applying this observation to the extra diffusive flux, one can interpret its effect as substituting B_n for its averaged value, $(B_n)_{ij} = B_{nf}$, in the region $-D_8\Delta t < x - x_f < D_8\Delta t$, $x = \mathbf{n}_{ij} \cdot \mathbf{x}$ being the spatial coordinate along the direction of $\mathbf{n}_{ij}$ and x_f being the face position. While averaging the magnetic energy in the same region, the EMP arises from the difference between the averaged magnetic pressure and the magnetic pressure of the averaged field: $D_8\Delta t((1/2)(B_n^2)_i + (1/2)(B_n^2)_j - B_{nf}^2) = 2D_8\Delta t P_M$. Now, Eq.(B.9), applied to the ith side of the ijth face, can be interpreted as the Hugoniot relationship at the discontinuity, moving with the speed $(u_n)_i$, which dynamically separates the $\widetilde{\mathbf{W}}_i$ state from ith state and accounts for the effect from the source term during the time step: $-(u_n)_i[\widetilde{\mathbf{U}}((\widetilde{\mathbf{W}}_i) - \mathbf{U}_i] + [\widetilde{\mathbf{F}}_n(\widetilde{\mathbf{W}}_i) - (\mathbf{F}_n)_i] = -\mathbf{G}_i[B_{nf} - (B_n)_i]$. In the region of the RS7 fan B_n is continuous and the EMP is present.

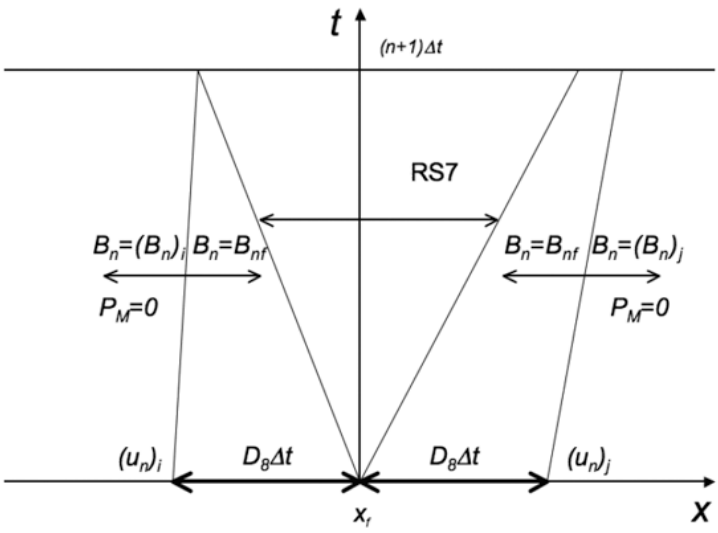

Figure B.1: The geometry of the RS7 fan and side discontinuities.

BIBLIOGRAPHY

BIBLIOGRAPHY

[1] M. D. Altschuler, R. H. Levine, M. Stix, and J. Harvey. High Resolution Mapping of the Magnetic Field of the Solar Corona. *Sol. Phys.*, 51:345–375, March 1977.

[2] M. D. Altschuler and G. Newkirk. Magnetic Fields and the Structure of the Solar Corona. I: Methods of Calculating Coronal Fields. *Sol. Phys.*, 9:131–149, September 1969.

[3] J. J. Aly. On some properties of force-free magnetic fields in infinite regions of space. *Astrophys. J.*, 283:349–362, August 1984.

[4] A. Anttila and T. Sahla. ERNE observations of energetic particles associated with Earth-directed coronal mass ejections in April and May, 1997. *Ann. Geophys.*, 18:1373–1381, November 2000.

[5] C. N. Arge, J. G. Luhmann, D. Odstrcil, C. J. Schrijver, and Y. Li . Stream Structure and Coronal Sources of the Solar Wind During the May 12th, 1997 CME. *J. Atm. and Sol.-Ter. Phys.*, 66:1295–1309, October 2004.

[6] C. N. Arge and V. J. Pizzo. Improvement in the Prediction of Solar Wind Conditions Using Near-Real time Solar Magnetic Field Updates. *J. Geophys. Res.*, 105:10,465–10,479, May 2000.

[7] M. Aschwanden. *Physics of the Solar Corona, an Introduction*. Springer, 2004.

[8] H. W. Babcock. The Topology of the Sun's Magnetic Field and the 22-YEAR Cycle. *Astrophys. J.*, 133:572, March 1961.

[9] D. N. Baker, X. Li, S. G. Kanekal, K. W. Ogilvie, R. P. Lepping, J. B. Blake, L. B. Callis, G. Rostoker, H. J. Singer, and G. D. Reeves. A strong CME-related magnetic cloud interaction with the Earth's magnetosphere: ISTP observations of rapid relativistic electron acceleration on May 15, 1997. *Geophys. Res. Lett.*, 25:2975–2978, August 1998.

[10] A. Barnes. Theory of Magnetohydrodynamic Waves – The WKB Approximation Revisited. *J. Geophys. Res.*, 97:12,105–12,112, August 1992.

[11] S. Basu and H. M. Antia. Changes in Solar Dynamics from 1995 to 2002. *Astrophys. J.*, 585:553–565, March 2003.

[12] L. Bolduc. GIC observations and studies in the Hydro-Qubec power system. *J. Atm. and Sol.-Ter. Phys.*, 64:1793–1802, November 2002.

[13] R. A. Burger and M. Hitge. The Effect of a Fisk-Type Heliospheric Magnetic Field on Cosmic-Ray Modulation. *Astrophys. J. Lett.*, 617:L73–L76, December 2004.

[14] R. A. Burger, Y. van Niekerk, and M. S. Potgieter. An Estimate of Drift Effects in Various Models of the Heliospheric Magnetic Field. *S. Sci. Rev.*, 97:331–335, May 2001.

[15] R. Cameron and A. Hopkins. A new estimate of the solar meridional flow. *Sol. Phys.*, 183:263–276, December 1998.

[16] H. V. Cane and I. G. Richardson. Interplanetary Coronal Mass Ejections in the Near-Earth Solar Wind During 1996-2002. *J. Geophys. Res.*, 108:SSH 6–1, April 2003.

[17] B. W. Carroll and D. A. Ostlie. *An Introduction to Modern Astrophysics*. Addison, Wesley, Longman, 1996.

[18] O. Cohen, L. A. Fisk, I. I. Roussev, G. Toth, and T. I. Gombosi. Enhancement of Photospheric Meridional Flow by Reconnection Processes. *Astrophys. J.*, 654:1537–1542, July 2006.

[19] O. Cohen, I. V. Sokolov, I. I. Roussev, C. N Arge, W. B. Manchester, T. I. Gombosi, R. A. Frazin, H. Park, M. D. Butala, F. Kamalabadi, and M. Velli. A Semi-Empirical Magnetohydrodynamical Model of the Solar Wind. *Astrophys. J. Lett.*, 645:L163–L166, January 2007.

[20] O. Cohen, I. V. Sokolov, I. I. Roussev, and T. I. Gombosi. Validation of a synoptic solar wind model. *J. Geophys. Res.*, 113:A03104, March 2008.

[21] O. Cohen, I. V. Sokolov, I. I. Roussev, N. Lugaz, W. B. Manchester, T. I. Gombosi, and C. N. Arge. Validation of a Global 3D Heliospheric Model With Observations for the May 12, 1997 CME Event. *J. Atm. and Sol.-Ter. Phys.*, 70:583–592, February 2008.

[22] S. R. Cranmer, A. A. van Ballegooijen, and R. J. Edgar. Self-consistent Coronal Heating and Solar Wind Acceleration from Anisotropic Magnetohydrodynamic Turbulence. *Astrophys. J. Sup.*, 171:520–551, August 2007.

[23] N. U. Crooker, J. T. Gosling, and S. W. Kahler. Reducing Heliospheric Magnetic Flux from Coronal Mass Ejections Without Disconnection. *J. Geophys. Res. (Space Physics)*, 107(A2):1,028, February 2002.

[24] R. L. Dewar. Interaction Between Hydrodynamic Waves and a Time-Dependent, Inhomogeneous Medium. *Phys. of Fluids*, 13:2,710–2,719, 1970.

[25] M. Dikpati. Solar magnetic fields and the dynamo theory. *Adv. S. Res.*, 35:322–328, 2005.

[26] M. Dikpati, G. de Toma, P. A. Gilman, C. N. Arge, and O. R. White. Diagnostics of Polar Field Reversal in Solar Cycle 23 Using a Flux Transport Dynamo Model. *Astrophys. J.*, 601:1136–1151, February 2004.

[27] T. L. Duvall, Jr. Large-scale solar velocity fields. *Sol. Phys.*, 63:3–15, August 1979.

[28] U. Feldman, K. G. Widing, and H. P. Warren. Morphology of the Quiet Solar Upper Atmosphere in the $4\times10^4 < T_e < 1.4\times10^6$ K Temperature Regime. *Astrophys. J.*, 522:1,133–1,147, September 1999.

[29] L. A. Fisk. Motion of the Footpoints of Heliospheric Magnetic Field Lines at the Sun: Implications for Recurrent Energetic Particle Events at High Heliographic Latitudes. *J. Geophys. Res.*, 101(A7):15,547–15,554, July 1996.

[30] L. A. Fisk. Acceleration of the Solar Wind as a Result of the Reconnection of Open Magnetic Flux with Coronal Loops. *J. Geophys. Res.*, 108(A4):1,157, April 2003.

[31] L. A. Fisk. The Open Magnetic Flux of the Sun. I. Transport by Reconnections with Coronal Loops. *Astrophys. J.*, 626:563–573, June 2005.

[32] L. A. Fisk and N. A. Schwadron. The Behavior of the Open Magnetic Field of the Sun. *Astrophys. J.*, 560:425–438, October 2001.

[33] L. A. Fisk, N. A. Schwadron, and T. H. Zurbuchen. Acceleration of the Fast Solar Wind by the Emergence of New Magnetic Flux. *J. Geophys. Res.*, 104:19,765–19,772, September 1999.

[34] T. G. Forbes. A Review on the Genesis of Coronal Mass Ejections. *J. Geophys. Res.*, 105:23,153–23,166, October 2000.

[35] A. C. Fraser-Smith. Centered and eccentric geomagnetic dipoles and their poles, 1600 - 1985. *Reviews of Geophysics*, 25:1–16, 1987.

[36] H.. Gleisner and J. Watermann. Concepts of medium-range (1-3 days) geomagnetic forecasting. *Adv. in Spc. Res.*, 37:1116–1123, August 2006.

[37] G. Gloeckler, T. H. Zurbuchen, and J. Geiss. Implications of the Observed Anti-Correlation Between Solar Wind Speed and Coronal Electron Temperature. *J. Geophys. Res. (Space Physics)*, 108(A4):1,158, April 2003.

[38] S. K. Godunov. Symmetric form of the equations of Magnetohydrodynamics. In *Numerical methods for mechanics of continuum medium*, volume 1, page 1, 1972.

[39] T. I. Gombosi. *Gaskinetic Theory*. Cambridge University Press, 1994.

[40] T. I. Gombosi. *Physics of the Space Environment*. Cambridge University Press, 1998.

[41] N. Gopalswamy and M. L. Kaiser. Solar eruptions and long wavelength radio bursts: The 1997 May 12 event. *Adv. in Spc. Res.*, 29:307–312, 2002.

[42] C. P. T. Groth, D. L. DeZeeuw, T. I. Gombosi, and K. G. Powell. Global Three-Dimensional MHD Simulation of a Space Weather Event: CME Formation, Interplanetary Propagation, and Interaction with the Magnetosphere. *J. Geophys. Res.*, 105:25,053–25,078, November 2000.

[43] A. Harten, P. D. Lax, and B. Van Leer. On Upstream Differencing and Godunov-Type Schemes for Hyperbolic Conservation Laws. *SIAM Review*, 25:35–61, 1983.

[44] D. Hathaway, P. Gilman, J. W. Harvey, F. Hill, R. B. Howard, H. P. Jones, J. Kasher, J. B. Leibacher, J. Pintar, and G. W. Simon. GONG Observations of Solar Surface Flows. *Science*, 272:1306, May 1996.

[45] D. H. Hathaway. Doppler Measurements of the Sun's Meridional Flow. *Astrophys. J.*, 460:1027, April 1996.

[46] H. Isobe, T. Yokoyama, M. Shimojo, T. Morimoto, H. Kozu, S. Eto, N. Narukage, and K. Shibata. Reconnection Rate in the Decay Phase of a Long Duration Event Flare on 1997 May 12. *Astrophys. J.*, 566:528–538, February 2002.

[47] S. A. Jacques. Momentum and Energy Transport by Waves in the Solar Atmosphere and Solar Wind. *Astrophys. J.*, 215:942–951, August 1977.

[48] L. Jian, C. T. Russell, J. G. Luhmann, and R. M. Skoug. Properties of Interplanetary Coronal Mass Ejections at 1AU During 1995-2004. *Sol. Phys.*, 239:393–436, December 2006.

[49] V. K. Jordanova, C. J. Farrugia, R. M. Thorne, G. V. Khazanov, G. D. Reeves, and M. F. Thomsen. Modeling ring current proton precipitation by electromagnetic ion cyclotron waves during the May 14-16, 1997, storm. *J. Geophys. Res.*, 106:7–22, January 2001.

[50] J. A. Klimchuk. On Solving the Coronal Heating Problem. *Sol. Phys.*, 234:41–77, March 2006.

[51] R. W. Komm, R. F. Howard, and J. W. Harvey. Meridional Flow of Small Photospheric Magnetic Features. *Sol. Phys.*, 147:207–+, October 1993.

[52] S. Latushko. Meridional drift in the large-scale solar magnetic field pattern. *Sol. Phys.*, 149:231–241, February 1994.

[53] R. B. Leighton. Transport of Magnetic Fields on the Sun. *Astrophys. J.*, 140:1,547–1,562, November 1964.

[54] X Li, D. N. Baker, M. Teremin, T. E. Cayton, G. D. Reeves, R. S. Selesnick, J. B. Blake, G. Lu, S. G. Kanekal, and H. J. Singer. Rapid enchancements of relativistic electrons deep in the magnetosphere during the May 15, 1997, magnetic storm. *J. Geophys. Res.*, 104:4467–4476, March 1999.

[55] J. A. Linker, Z. Mikić, D. A. Biesecker, R. J. Forsyth, S. E. Gibson, A. J. Lazarus, A. Lecinski, P. Riley, A. Szabo, and B. J. Thompson. Magnetohydrodynamic Modeling of the Solar Corona During Whole Sun Month. *J. Geophys. Res.*, 104:9,809–9,830, May 1999.

[56] R. Lionello, J. A. Linker, and Z. Mikić. Including the Transition Region in Models of the Large-Scale Solar Corona. *Astrophys. J.*, 546:542–551, January 2001.

[57] R. Lionello, P. Riley, J. A. Linker, and Z. Mikić. The Effects of Differential Rotation on the Magnetic Structure of the Solar Corona: Magnetohydrodynamic Simulations. *Astrophys. J.*, 625:463–473, May 2005.

[58] H. Liu, K. Schlegel, and S.-Y. Ma. Combined ESR and EISCAT observations of the dayside polar cap and auroral oval during the May 15, 1997 storm. *Ann. Geophys.*, 18:1067–1072, September 2000.

[59] B. J. Lynch, S. K. Antiochos, P. J. MacNeice, T. H. Zurbuchen, and L. A. Fisk. Observable Properties of the Breakout Model for Coronal Mass Ejections. *Astrophys. J.*, 617:589–599, December 2004.

[60] D. H. Mackay and M. Lockwood. The Evolution of the Sun's Open Magnetic Flux - II. Full Solar Cycle Simulations. *Sol. Phys.*, 209:287–309, October 2002.

[61] D. H. Mackay, E. R. Priest, and M. Lockwood. The Evolution of the Sun's Open Magnetic Flux - I. A Single Bipole. *Sol. Phys.*, 207:291–308, June 2002.

[62] W. B. Manchester IV. Shear Flows Driven by the Lorentz Force: An Energy Source for Coronal Mass Ejections and Flares. In *APS Conference Series Vol. 383: Subsurface and Atmospheric Influences on Solar Activity*, page 91, 2008.

[63] W. B. Manchester IV, T. I. Gombosi, I. Roussev, A. Ridley, D. L. De Zeeuw, I. V. Sokolov, K. G. Powell, and G. Tóth. Modeling a Space Weather Event from the Sun to the Earth: CME Generation and Interplanetary Propagation. *J. Geophys. Res.*, 109(A18):2,107–2,122, February 2004.

[64] S. K. Mathew and A. Ambastha. Magnetic field gradient and flare: study of a small flare in NOAA 8038. *Sol. Phys.*, 197:75–84, November 2000.

[65] D. J. McComas, H. A. Elliott, N. A. Schwadron, J. T. Gosling, R. M. Skoug, and B. E. Goldstein. The three-dimensional solar wind around solar maximum. *Geophys. Res. Lett.*, 30:24–1, May 2003.

[66] J. F. McKenzie, W. I. Axford, and M. Banaszkiewicz. The Fast Solar Wind. *Geophys. Res. Lett.*, 24:2,877, November 1997.

[67] Z. Mikic, J. A. Linker, D. D. Schnack, R. Lionello, and A. Tarditi. Magnetohydrodynamic modeling of the global solar corona. *Physics of Plasmas*, 6:2217–2224, May 1999.

[68] M. Neugebauer, P. C. Liewer, E. J. Smith, R. M. Skoug, and T. H. Zurbuchen. Sources of the Solar Wind at Solar Activity Maximum. *J. Geophys. Res.*, 107:SSH 13–1, December 2002.

[69] D. Odstrcil and V. J. Pizzo. Three-Dimensional Propagation of Coronal Mass Ejections in a Structured Solar Wind Flow 1. CME Launched Within the Streamer Belt. *J. Geophys. Res.*, 104:483–492, January 1999.

[70] D. Odstrčil, P. Riley, and X. P. Zhao. Numerical simulation of the 12 May 1997 interplanetary CME event. *J. Geophys. Res.*, 109, February 2004.

[71] M. J. Owens and N. U. Crooker. Coronal mass ejections and magnetic flux buildup in the heliosphere. *J. Geophys. Res.*, 111:10,104, October 2006.

[72] M. J. Owens, N. A. Schwadron, N. U. Crooker, W. J. Hughes, and H. E. Spence. Role of coronal mass ejections in the heliospheric Hale cycle. *Geophys. Res. Lett.*, 34:6104, March 2007.

[73] E. N. Parker. Dynamics of the Interplanetary Gas and Magnetic Fields. *Astroph. J.*, 128:664–676, November 1958.

[74] E. N. Parker. *Interplanetary Dynamical Processes*. Interscience Publishers (Wiley), 1963.

[75] E. N. Parker. Nanoflares and the solar X-ray corona. *Astroph. J.*, 330:474–479, July 1988.

[76] V. Pilipenko, N. Kleimenova, O. Kozyreva, M. Engebretson, and O. Rasmussen. Long-period magnetic activity during the May 15, 1997 storm. *J. Atm. and Sol.-Ter. Phys.*, 63:489–501, March 2001.

[77] V. A. Pilipenko, O. V. Kozyreva, M. J. Engebretson, D.L. Detrick, and S.N. Samsonov. Dynamics of long-period magnetic activity and energetic particle precipitation during the May 15, 1997 storm. *J. Atm. and Sol.-Ter. Phys.*, 64:831–43, March 2002.

[78] S. P. Plunkett, R. A. Thompson, B. J. andHoward, D. J. Michels, O. C. St. Cyr, S. J. Tappin, R. Schwenn, and P. L. Lamy. LASCO observations of an Earth-directed coronal mass ejection on May 12, 1997. *Geophys. Res. Lett.*, 25:2477–2480, July 1998.

[79] G. W. Pneuman and R. A. Kopp. Gas-Magnetic Field Interactions in the Solar Corona. *Sol. Phys.*, 18:258, 1971.

[80] K. G. Powell, P. L. Roe, T. J. Linde, T. I. Gombosi, and D. L. De Zeeuw. A Solution-Adaptive Upwind Scheme for Ideal Magnetohydrodynamics. *J. Comp. Phys.*, 154:284–309, September 1999.

[81] P. Riley. An Alternative Interpretation on the Relashionship between the Inferred Open Solar Flux and the Interplanetary Magnetic Field. *Accepted to ApJ*, 2007.

[82] I. I. Roussev, T. G. Forbes, T. I. Gombosi, I. V. Sokolov, D. L. DeZeeuw, and J. Birn. A Three-Dimensional Flux Rope Model for Coronal Mass Ejections Based on a Loss of Equilibrium. *Astrophys. J. Lett.*, 588:L45–L48, May 2003.

[83] I. I. Roussev, T. I. Gombosi, I. V. Sokolov, M. Velli, W. Manchester, D. L. DeZeeuw, P. Liewer, G. Tóth, and J. Luhmann. A Three-Dimensional Model of the Solar Wind Incorporating Solar Magnetogram Observations. *Astrophys. J. Lett.*, 595:L57–L61, September 2003.

[84] I. I. Roussev and I. V. Sokolov. Models of Solar Eruptions: Recent Advances from Theory and Simulations. *Solar Eruptions and Energetic Particles, ed. N. Gopalswamy, R. Mewaldt, and J. Torsti, Geophysical Monograph 165, 89-102*, 165:89–102, October 2006.

[85] T. Saito, T. Sakurai, and K. Yumoto. The earth's palaeomagnetosphere as the third type of planetary magnetosphere. *Plan. S. Sci.*, 26:413–422, May 1978.

[86] J. Schou, H. M. Antia, S. Basu, R. S. Bogart, R. I. Bush, S. M. Chitre, J. Christensen-Dalsgaard, M. P. di Mauro, W. A. Dziembowski, A. Eff-Darwich, D. O. Gough, D. A. Haber, J. T. Hoeksema, R. Howe, S. G. Korzennik, A. G. Kosovichev, R. M. Larsen, F. P. Pijpers, P. H. Scherrer, T. Sekii, T. D. Tarbell, A. M. Title, M. J. Thompson, and J. Toomre. Helioseismic Studies of Differential Rotation in the Solar Envelope by the Solar Oscillations Investigation Using the Michelson Doppler Imager. *Astrophys. J.*, 505:390–417, September 1998.

[87] C. J. Schrijver and M. L. DeRosa. Photospheric and Heliospheric Magnetic Fields. *Sol. Phys.*, 212:165–200, January 2003.

[88] C. J. Schrijver, M. L. DeRosa, and A. M. Title. What Is Missing from Our Understanding of Long-Term Solar and Heliospheric Activity? *Astrophys. J.*, 577:1006–1012, October 2002.

[89] C. J. Schrijver, R. A. Shine, H. J. Hagenaar, N. E. Hurlburt, A. M. Title, L. H. Strous, S. M. Jefferies, A. R. Jones, J. W. Harvey, and T. L. Duvall, Jr. Dynamics of the Chromospheric Network: Mobility, Dispersal, and Diffusion Coefficients. *Astrophys. J.*, 468:921–+, September 1996.

[90] M. Schulz. Eigenmode approach to coronal magnetic structure with differential solar rotation. *J. Geophys. Res.*, 106:15859–15868, August 2001.

[91] H. B. Snodgrass and S. B. Dailey. Meridional Motions of Magnetic Features in the Solar Photosphere. *Sol. Phys.*, 163:21–42, January 1996.

[92] I. V. Sokolov, K. G. Powell, O. Cohen, and T. I. Gombosi. Computational MagnetoHydrodynamics, Based on Non-Linear Solution of the Well-Posed Riemann Problem. *APS Conference Series, in press*, 2007.

[93] I. V. Sokolov, K. G. Powell, T. I. Gombosi, and I. I. Roussev. A TVD principle and conservative TVD schemes for adaptive Cartesian grids. *Journal of Computational Physics*, 220:1–5, December 2006.

[94] I. V. Sokolov, E. V. Timofeev, J. Sakai, and K. Takayama. Artificial Wind – A New Framework to Construct Simple and Efficient Upwind Shock-Capturing Schemes. *J. Comp. Phys.*, 181:354–393, September 2002.

[95] S. T. Suess, A.-H. Wang, S. T. Wu, G. Poletto, and D. J. McComas. A Two-Fluid, MHD Coronal Model. *J. Geophys. Res.*, 104:4,697–4,708, March 1999.

[96] B. J. Thompson, S. P. Plunkett, J. B. Gurman, J. S. Newmark, O. C. St. Cyr, and D. J. Michels. SOHO/EIT observations of an Earth-directed coronal mass ejection on May 12, 1997. *Geophys. Res. Lett.*, 25:2465–2468, July 1998.

[97] V. S. Titov and P. Démoulin. Basic Topology of Twisted Magnetic Configurations in Solar Flares. *Astron. & Astrophys.*, 351:707–720, November 1999.

[98] G. Tóth. The $\nabla \cdot \mathbf{B} = 0$ Constraint in Shock-Capturing Magnetohydrodynamics Codes. *Journal of Computational Physics*, 161:605–652, July 2000.

[99] G. Tóth, I. V. Sokolov, T. I. Gombosi, D. R. Chesney, C. R. Clauer, D. L. De Zeeuw, K. C. Hansen, K. J. Kane, W. B. Manchester, R. C. Oehmke, K. G. Powell, A. J. Ridley, I. I. Roussev, Q. F. Stout, O. Volberg, R. A. Wolf, S. Sazykin, A. Chan, B. Yu, and J. Kóta. Space Weather Modeling Framework: A New Tool for the Space Science Community. *J. Geophys. Res.*, 110:12,226–12,237, December 2005.

[100] A. V. Usmanov. A Global Numerical 3-D MHD Model of the Solar Wind. *Sol. Phys.*, 146:377–396, August 1993.

[101] A. V. Usmanov and M. L. Goldstein. A Tilted-Dipole MHD Model of the Solar Corona and Solar Wind. *J. Geophys. Res.*, 108:1–1, September 2003.

[102] A. V. Usmanov, M. L. Goldstein, B. P. Besser, and J. M. Fritzer. A Global MHD Solar Wind Model with WKB Alfvén Waves: Comparison with Ulysses Data. *J. Geophys. Res.*, 105:12,675–12,696, June 2000.

[103] D. A. Uzdensky. The Fast Collisionless Reconnection Condition and the Self-Organization of Solar Coronal Heating. *Astrophys. J.*, 671:2139–2153, December 2007.

[104] H. A. Van der vorst. Bi-CGSTAB: A Fast and Smoothly Converging Variant of Bi-CG for the Solution of Nonsymmetric Linear Systems. *SIAM J. Sci. Stat. Comp.*, 13:631–644, 1992.

[105] M. Vandas, D. Odstrčil, and S. Watari. Three-Dimensional MHD Simulation of a Loop-Like Magnetic Cloud in the Solar Wind. *J. Geophys. Res.*, 107:2–1, September 2002.

[106] Y.-M. Wang, J. Lean, and N. R. Sheeley, Jr. The long-term variation of the Sun's open magnetic flux. *Geophys. Res. Lett.*, 27:505–+, 2000.

[107] Y.-M. Wang, J. L. Lean, and N. R. Sheeley, Jr. Modeling the Sun's Magnetic Field and Irradiance since 1713. *Astrophys. J.*, 625:522–538, May 2005.

[108] Y.-M. Wang, A. G. Nash, and N. R. Sheeley, Jr. Magnetic flux transport on the sun. *Science*, 245:712–718, August 1989.

[109] Y.-M. Wang and N. R. Sheeley. Solar Wind Speed and Coronal Flux-Tube Expansion. *Astrophys. J.*, 355:726–732, June 1990.

[110] Y.-M. Wang and N. R. Sheeley. Sunspot Activity and the Long-term Variations of the Sun's Open Magnetic Flux. *J. Geophys. Res.*, 107:SSH 10–1, October 2002.

[111] Y.-M. Wang, N. R. Sheeley, Jr., and J. Lean. Understanding the evolution of the Sun's open magnetic flux. *Geophys. Res. Lett.*, 27:621–+, 2000.

[112] D. F. Webb, R. P. Lepping, L. F. Burlaga, C. E. DeForest, D. E. Larson, S. F. Martin, S. P. Plunkett, and D. M. Rust. The origin and development of the May 1997 magnetic cloud. *J. Geophys. Res.*, 105:27251–27260, December 2000.

[113] C. C. Wu, M Dryer, and S. T. Wu. Three-dimensional MHD simulation of interplanetary magnetic field changes at 1 AU as a consequence of simulated solar flares. *Ann. Geophys.*, 14:383–399, April 1996.

[114] S. T. Wu, W. P. Guo, D. J. Michels, and L. F. Burlaga. MHD Description of the Dynamical Relationships Between a Flux Rope, Streamer, Coronal Mass Ejection, and Magnetic Cloud: An Analysis of the January 1997 Sun-Earth Connection Event. *J. Geophys. Res.*, 104:14,789–14,802, July 1999.

[115] S. Yashiro, N. Gopalswamy, G. Michalek, O. C. St. Cyr, S. P. Plunkett, N. B. Rich, and R. A. Howard. A catalog of white light coronal mass ejections observed by the SOHO spacecraft. *J. Geophys. Res.*, 109, July 2004.

[116] J. Zhao and A. G. Kosovichev. Torsional Oscillation, Meridional Flows, and Vorticity Inferred in the Upper Convection Zone of the Sun by Time-Distance Helioseismology. *Astrophys. J.*, 603:776–784, March 2004.